SAND2017-3473PE

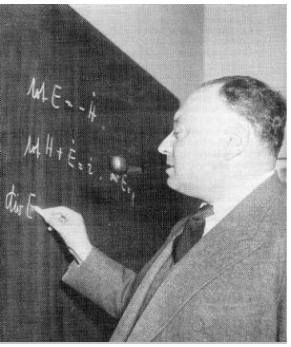

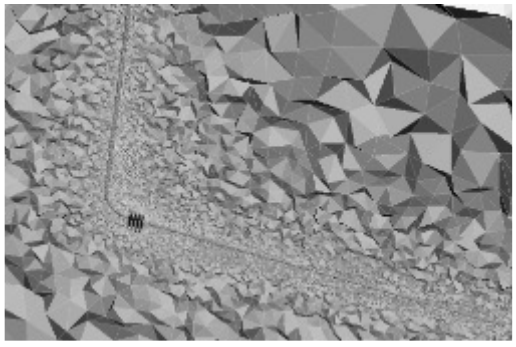
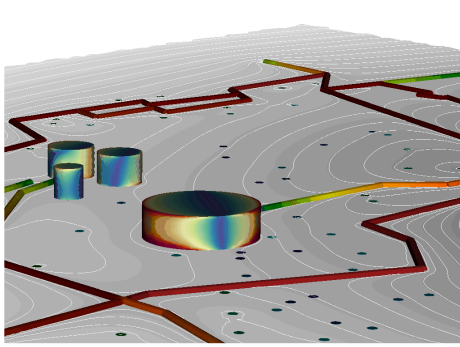

Sweating the small stuff: Why sub-wavelength details in EM modeling matter.

Chester J Weiss

Sandia National Laboratories is a multi-mission laboratory managed and operated by Sandia Corporation, a wholly owned subsidiary of Lockheed Martin Corporation, for the U.S. Department of Energy's National Nuclear Security Administration under contract DE-AC04-94AL85000. SAND NO. 2011-XXXXP

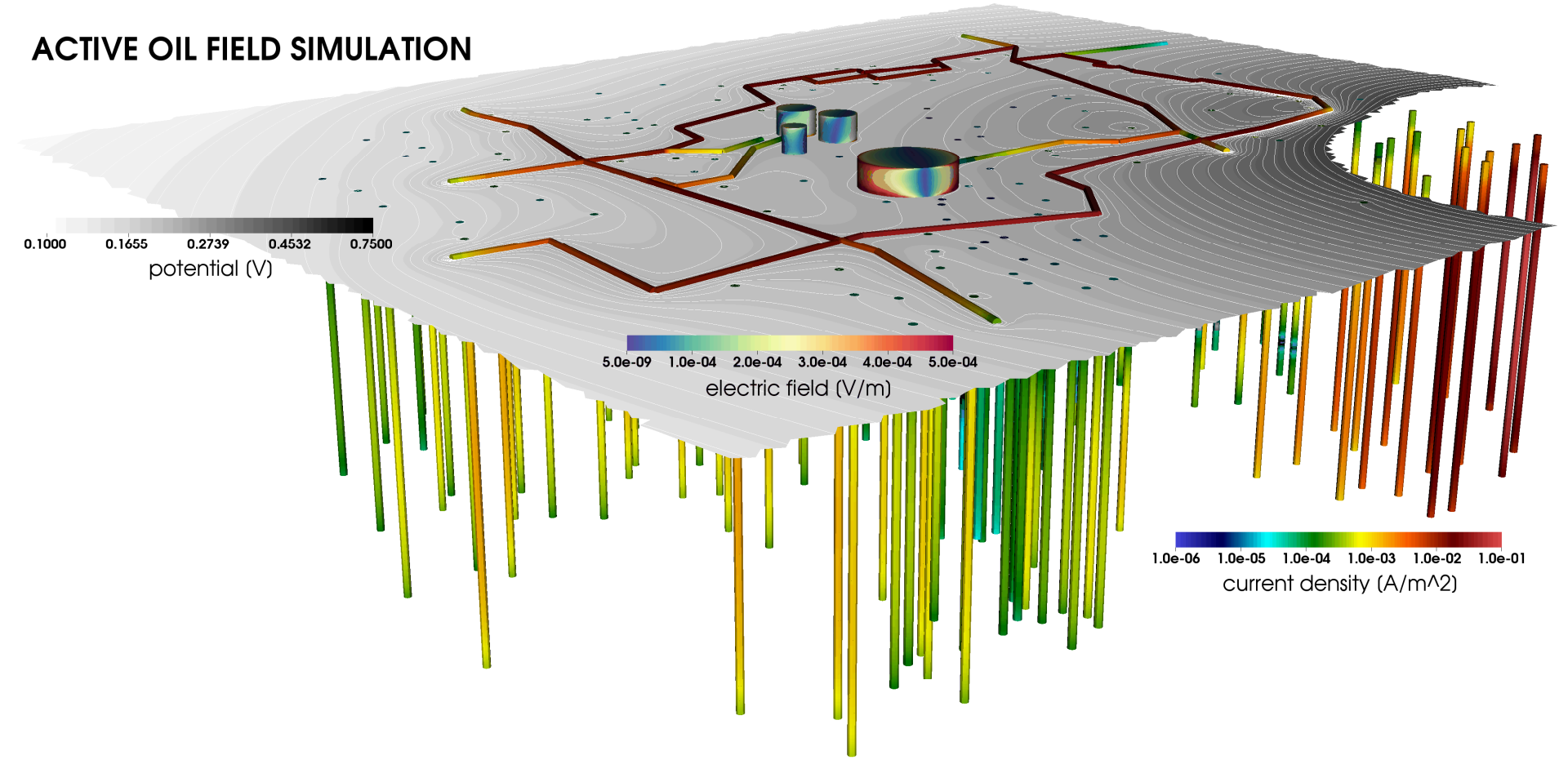
ACTIVE OIL FIELD SIMULATION
0.1000 0.1655 0.2739 0.4532 0.7500
potential (V)
5.0e-09 1.0e-04 2.0e-04 3.0e-04 4.0e-04 5.0e-04
electric field (V/m)
1.0e-06 1.0e-05 1.0e-04 1.0e-03 1.0e-02 1.0e-01
current density (A/m^2)

Computational Electromagnetics in Geoscience

Chester J. Weiss
Staff R&D Scientist
Sandia Nat. Labs cjweiss@sandia.gc
Adjunct Assoc. Prof. of Geophys.
Univ. New Mexico cjweiss@unm.edu

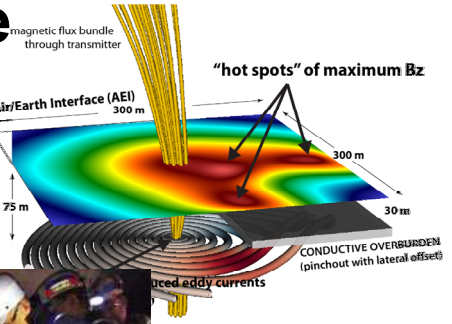

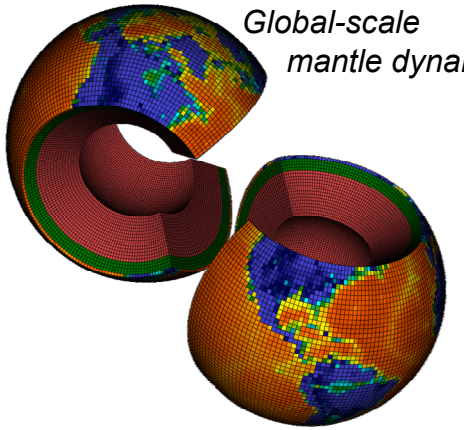

Global-scale mantle dynamics

Research

theory

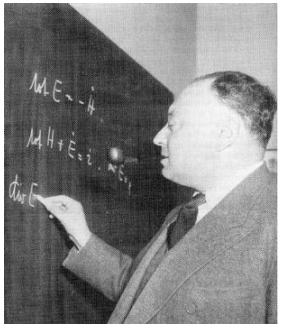

multi-scale transport

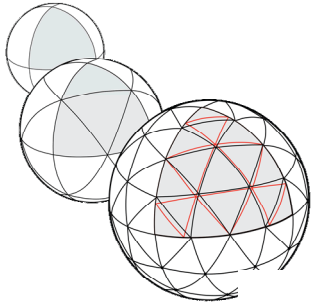

urban geophysics

"Through-the Earth" communications systems

Mapping sea ice thickness in Barrow AK

Teaching

Intro to Geophysics (U)
Potential Field Methods (U)
Electromagnetics I & II (G)
ıl Gravity and Geodesy (G)
Solid Earth Geophysics (G)

Funding sources

NSF — Collaborative Studies o
Earth's Deep Interior
Hydrologic Sciences

Built on LDRD Laboratory Directed Research and Development

earthscope www.earthscope.org

bp Centre for High Performance Computing

. tion for the improvement of mine safety

...ditional and online publishing

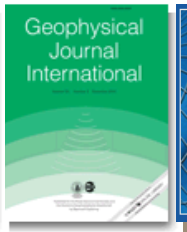

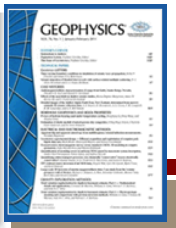

APS physics

OpenEM.org

Project Purpose

Built on LDRD Laboratory Directed Research and Development

Sandia National Laboratories

We propose to develop subsurface imaging and predictive modeling for realistic, complex geology – conditions where the usual assumptions of petrophysics and modeling no longer appl

Electromagnetic field propagation is a function of rock conductivity, which itself is a proxy for rock properties of greater interest such as fracture density, permeability and lithologic texture.

Field data is typically interpreted – and the Earth is typically modelled – as a piecewise constant (homogenized) medium. It's straightforward to demonstrate, however, that this assumption can be violated under routine exploration and monitoring conditions.

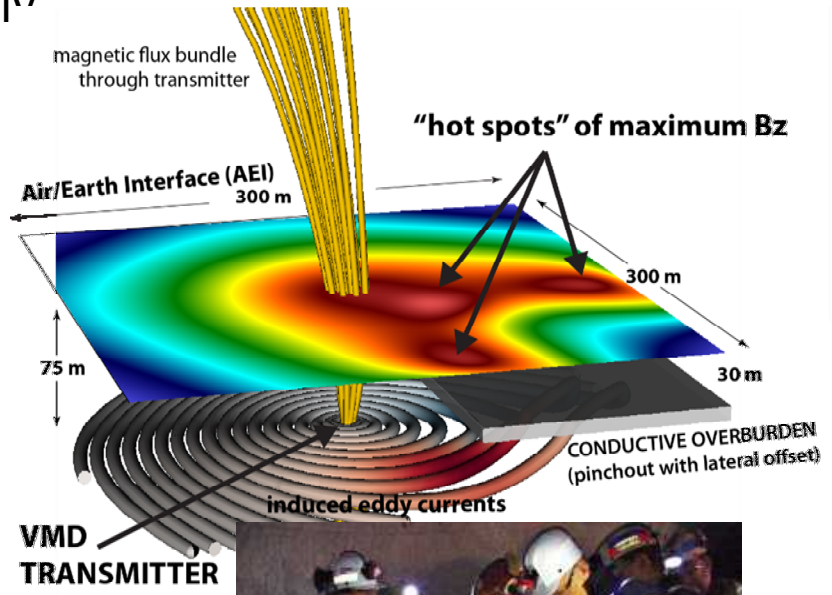

Example impact area:
"Through-the Earth"communications systems

Project Purpose

Built on LDRD Laboratory Directed Research and Development

Sandia National Laboratories

We propose to develop subsurface imaging and predictive modeling for realistic, complex geology – conditions where the usual assumptions of petrophysics and modeling no longer apply.

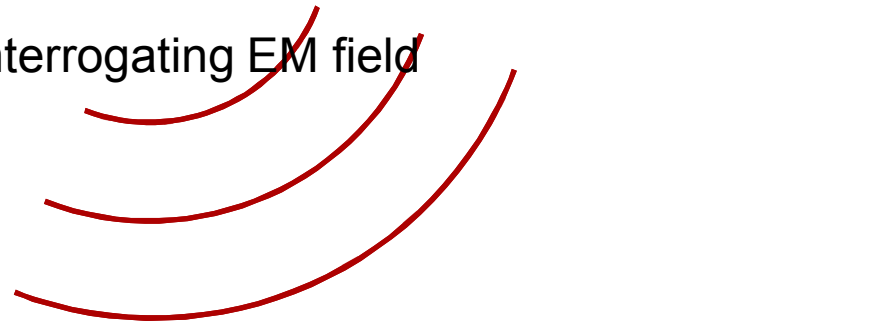

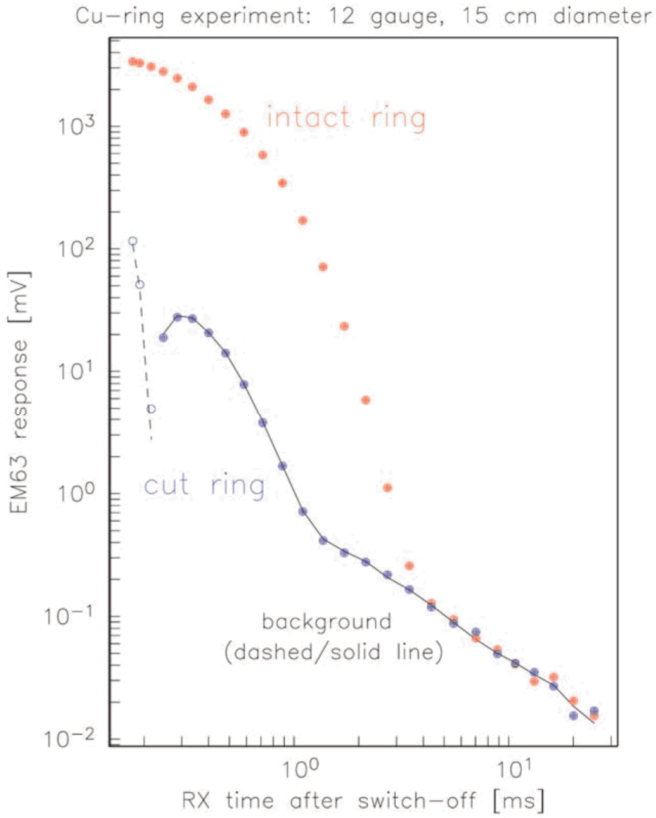

Fine scale details matter!

Everett, The Leading Edge (2005)

Project Purpose

Built on LDRD Laboratory Directed Research and Development

Sandia National Laboratories

We propose to develop subsurface imaging and predictive modeling for realistic, complex geology – conditions where the usual assumptions of petrophysics and modeling no longer apply.

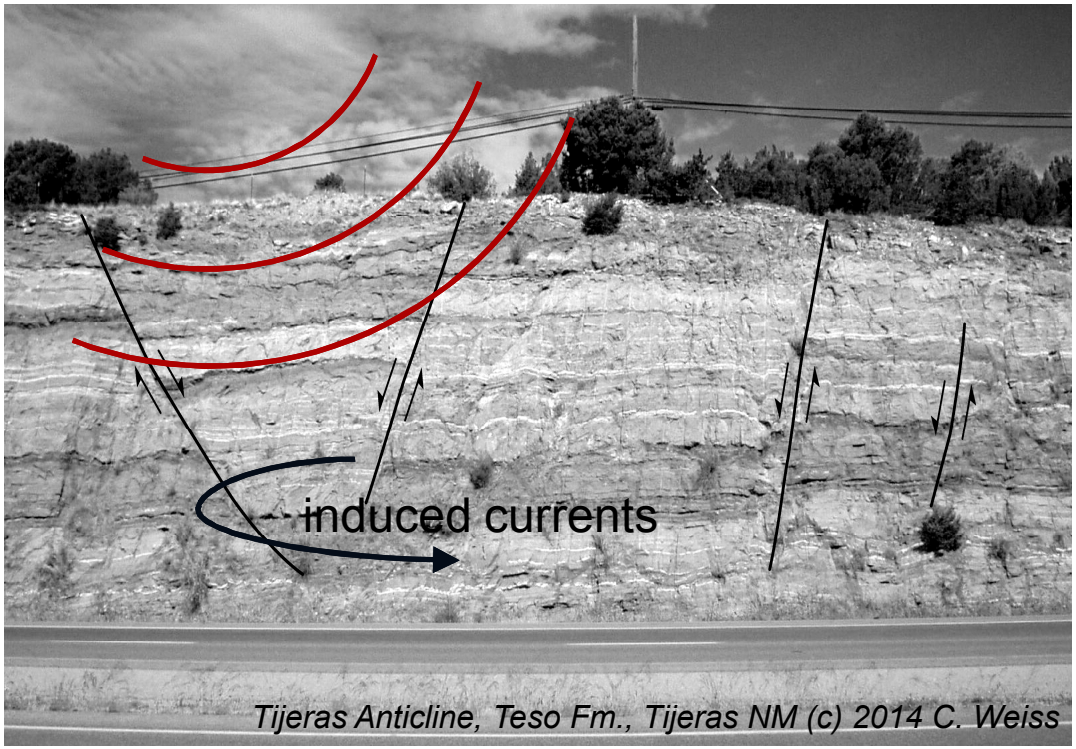

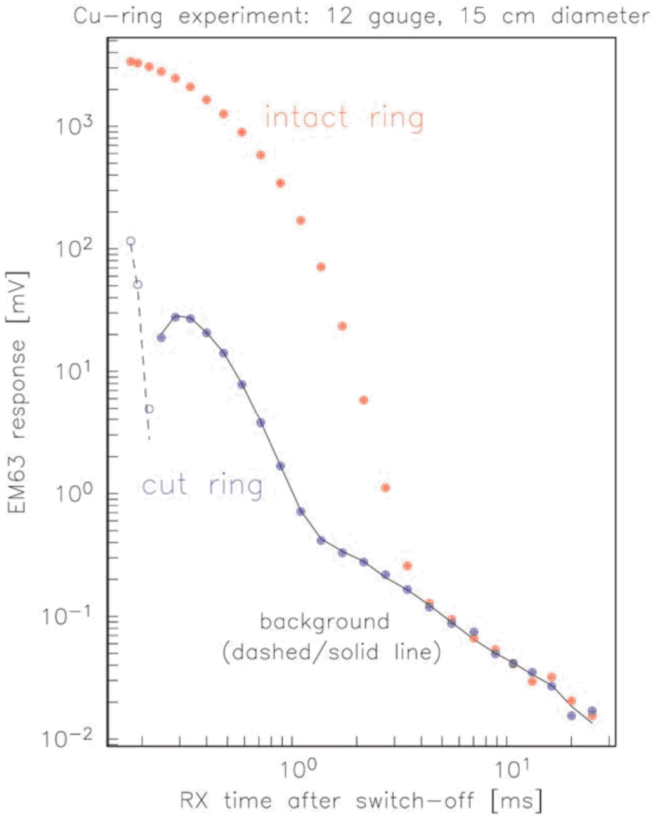

Fine scale details matter!

Why is this an LDRD?

Built on LDRD Laboratory Directed Research and Development

Sandia National Laboratories

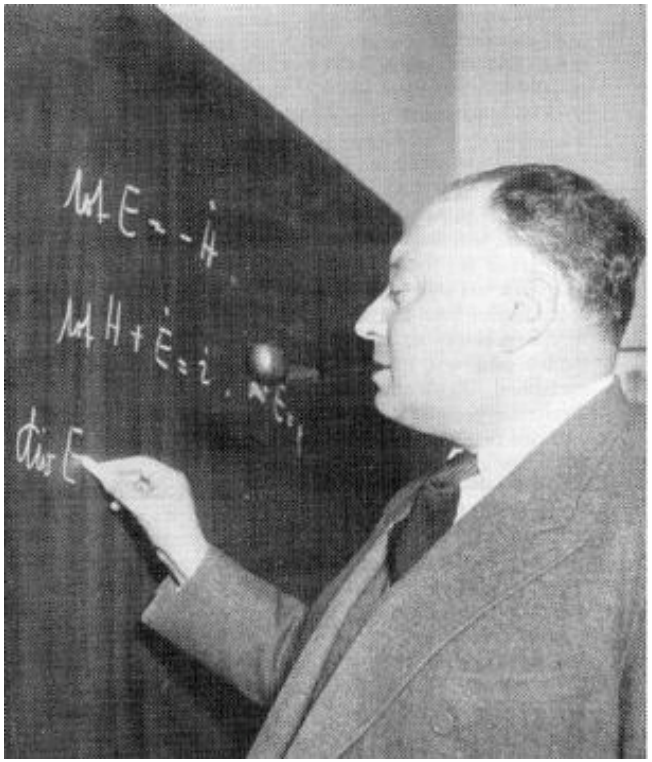

Diffusion on systems with embedded, multi-scale heterogeneity has been shown, in principle, to be described by novel class of partial differential equations – equations whose order of differentiation is non-integer.

This realization is far reaching, with limits presently uncharted, but with applications to:

earth science
economics
biophysics
signal analysis

For problems in Earth science, the transition between classical and "anomalous" fractional electromagnetic field propagation is unknown. This research is novel and high-risk, which if successful, will enable a modeling capability unparalleled elsewhere in the world.

Observational Evidence for a Fractional Diffusion Model of Electromagnetic Induction

TRANSMITTER ANTENNA
source current
step-off at time $t=t_0$

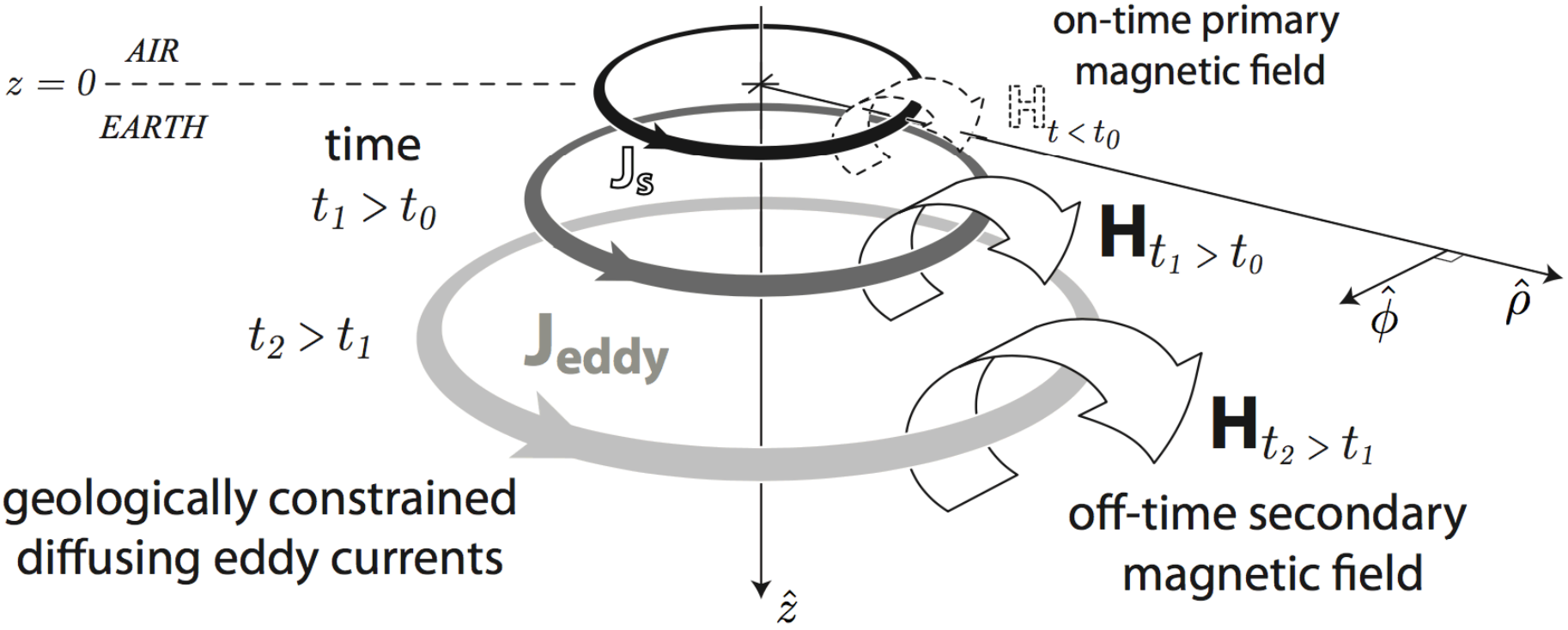

LAYERED EARTH

magnetic fields have vector components

only in the radial $\hat{\rho}$ and vertical $\hat{z}$ directions.

Experimental Evidence pt 1: Anomalous travel time arrival

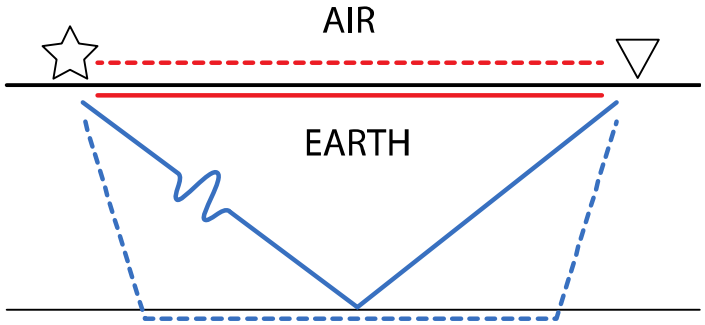

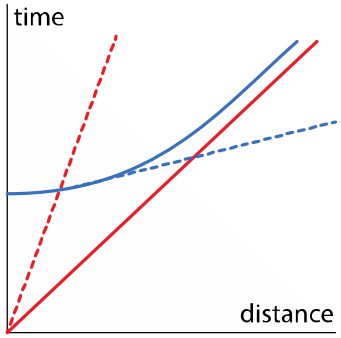

Similar to seismic travel time analysis, the arrival time of the EM pulse is analyzed for consistency with classical diffusion.

EARLY TIME
$t_0 < t < \tau$
$B_z > 0$

ZERO-CROSSING TIME
$t = \tau$
$B_z = 0$

LATE TIME
$t > \tau$
$B_z < 0$

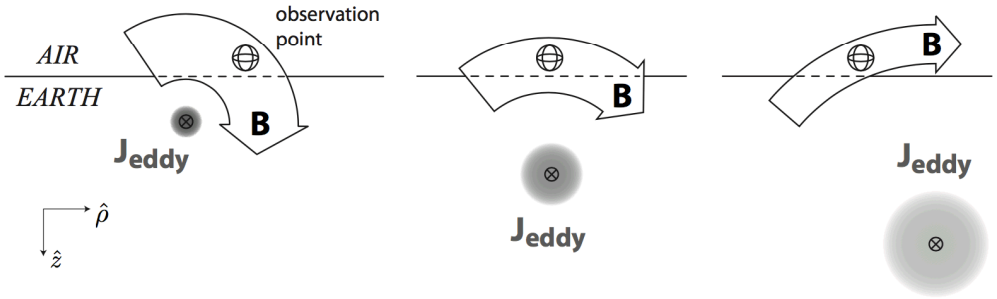

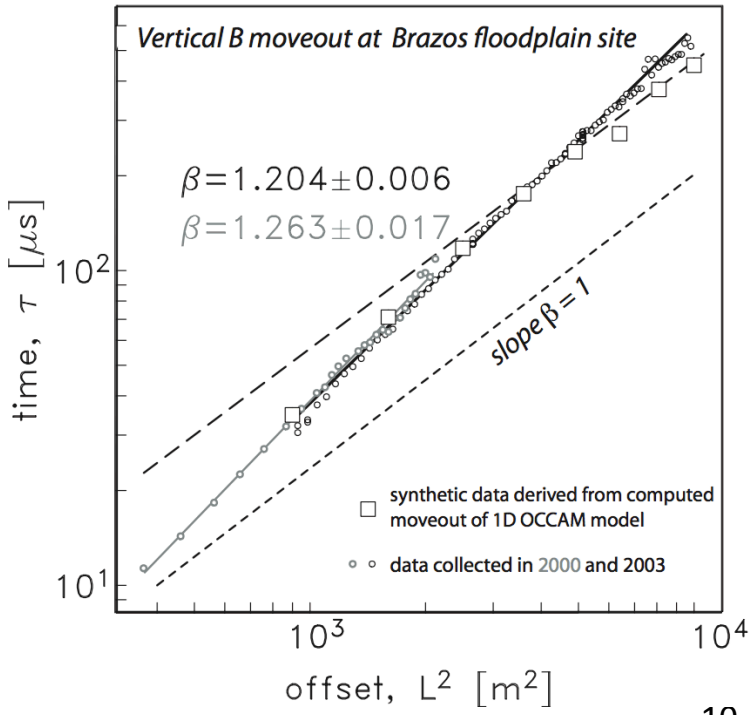

Weiss and Everett, JGR (2007)

Experimental Evidence pt 2: azimuthal variations on the circle

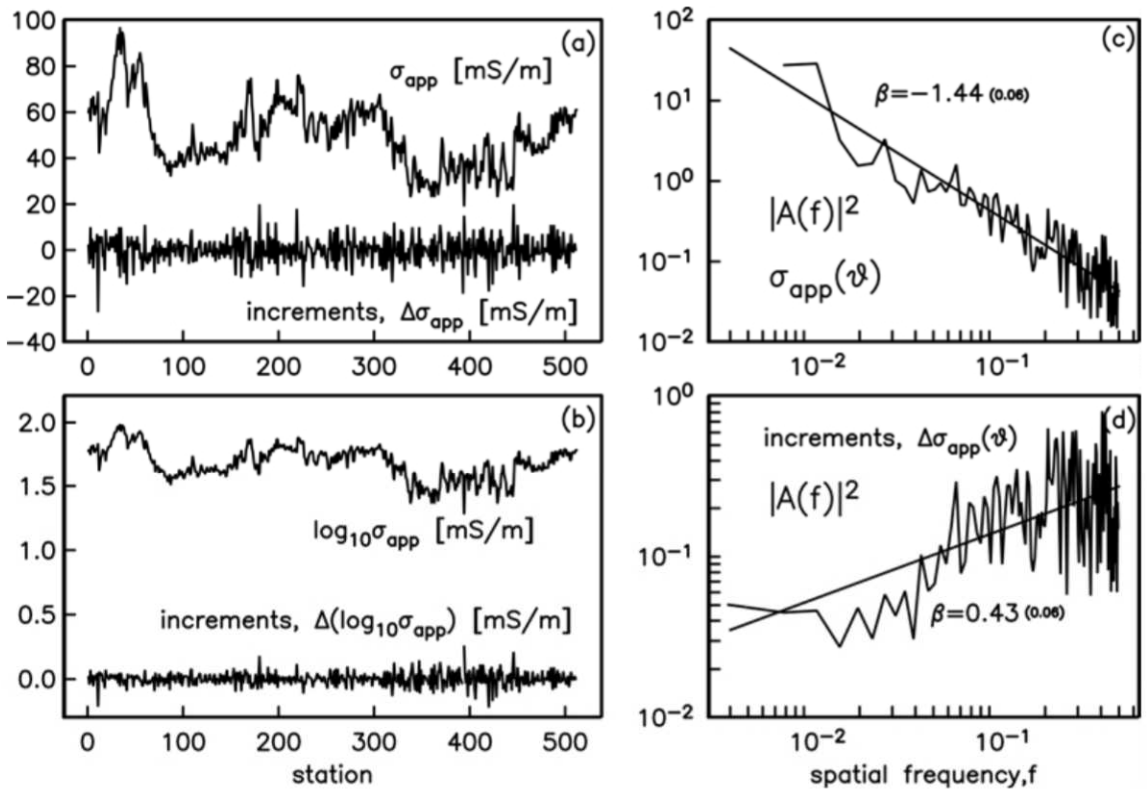

Figure 1. (a): Geonics EM34-3 near-surface electromagnetic response σ_a and increments $\Delta\sigma_a$ over Brazos River floodplain alluvium at College Station, Texas. (b): Logarithm and increments of logarithm of apparent conductivity shown in (a). (c): Power spectral density (PSD) of the apparent conductivity profile σ_a in (a) along with best-fit straight line. A slope $|\beta| > 1.0$ is characteristic of fractional Brownian motion. (d): PSD of the increments in apparent conductivity shown in (a). The slope $|\beta| < 1$ indicates a non-fractal signal similar to Gaussian noise.

|slope| > 1 consistent with long-range correlations,
i.e. fractional Brownian motion (fBm)

Everett and Weiss, GRL (2002)

Putting it all together at the macroscopic level

Pulse propagation

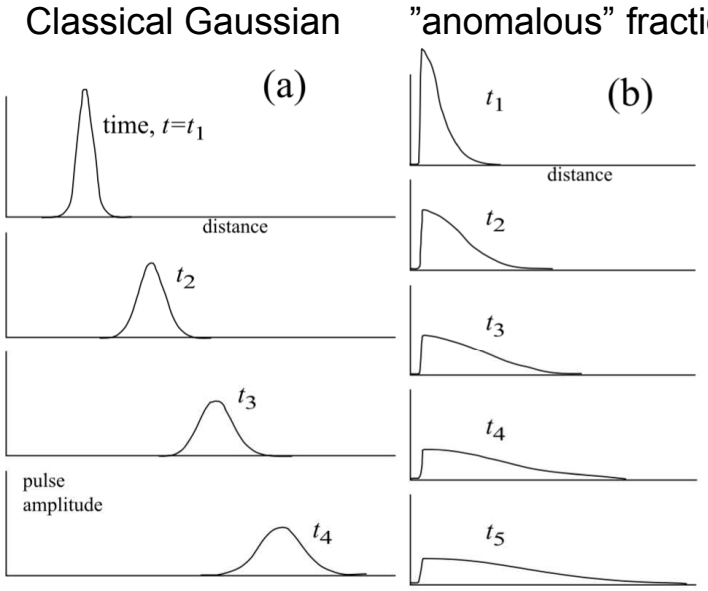

Figure 1. (a) Propagation of a Gaussian pulse $G(x,t)$ undergoing classical diffusion. (b) Propagation of a CTRW pulse $A(x,t)$ undergoing anomalous diffusion (after the work of *Scher and Montroll* [1975]).

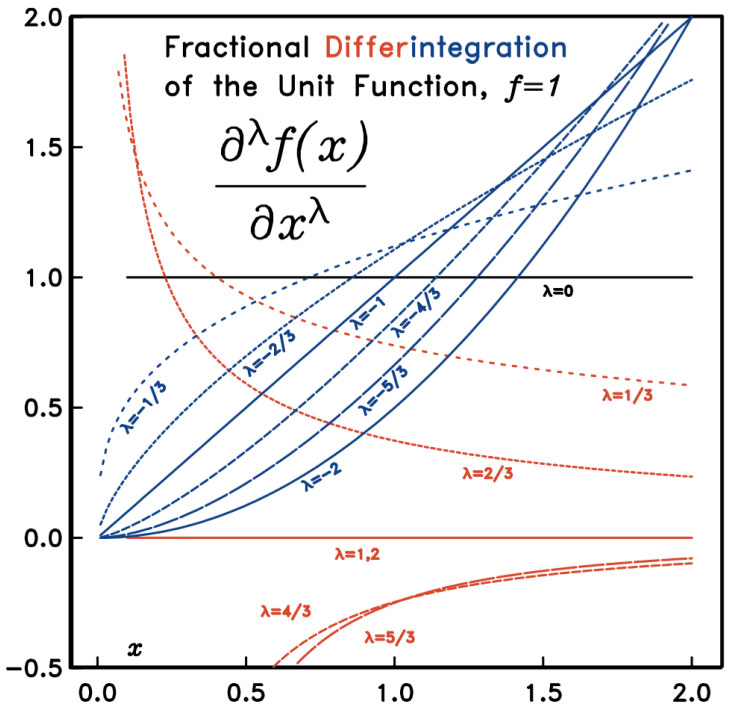

Fractional diffusion equation

$$\frac{\partial}{\partial t}A(x,t) = {}_0D_t^{1-\alpha}\left[v_\alpha \frac{\partial^2}{\partial x^2}A(x,t)\right]$$

Riemann-Liouville convolution

$${}_0D_t^{1-\alpha}A(x,t) = \frac{1}{\Gamma(\alpha)}\frac{\partial}{\partial t}\left[\int_0^t \frac{A(x,t')}{(t-t')^{1-\alpha}}\,\mathrm{d}t'\right]$$

Weiss and Everett, JGR (2007)

Our EM Modeling and Optimization Toolkit

3D numerical modeling toolkit

Sandia National Laboratories

Computers & Geosciences 58 (2013) 40–52

Contents lists available at SciVerse ScienceDirect

Computers & Geosciences

journal homepage: www.elsevier.com/locate/cageo

Project APhiD: A Lorenz-gauged **A**-Φ decomposition for parallelized computation of ultra-broadband electromagnetic induction in a fully heterogeneous Earth

Chester J. Weiss*

Department of Geosciences, Virginia Tech, Blacksburg, VA 24061, United States

Benchmarked against independent reference solutions for 1D, 2D and 3D geometries over length scales from 0.001 – 1e5 m and frequencies 0.01 – 1e9 Hz.

simultaneous, parallel computation of multiple-frequencies over a single grid

Complex Geology is mapped onto a Cartesian Grid

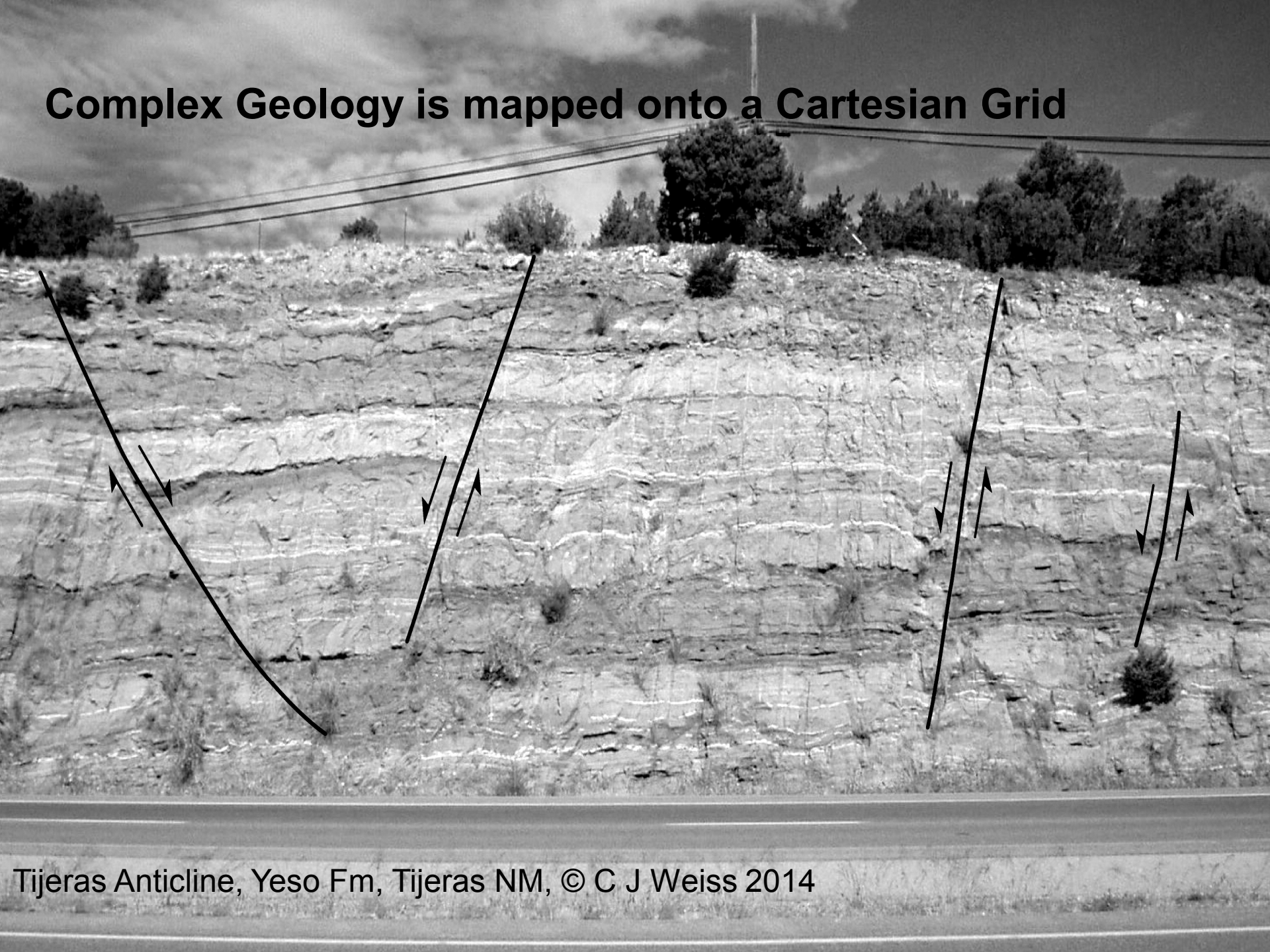

Tijeras Anticline, Yeso Fm, Tijeras NM, © C J Weiss 2014

Complex Geology is mapped onto a Cartesian Grid

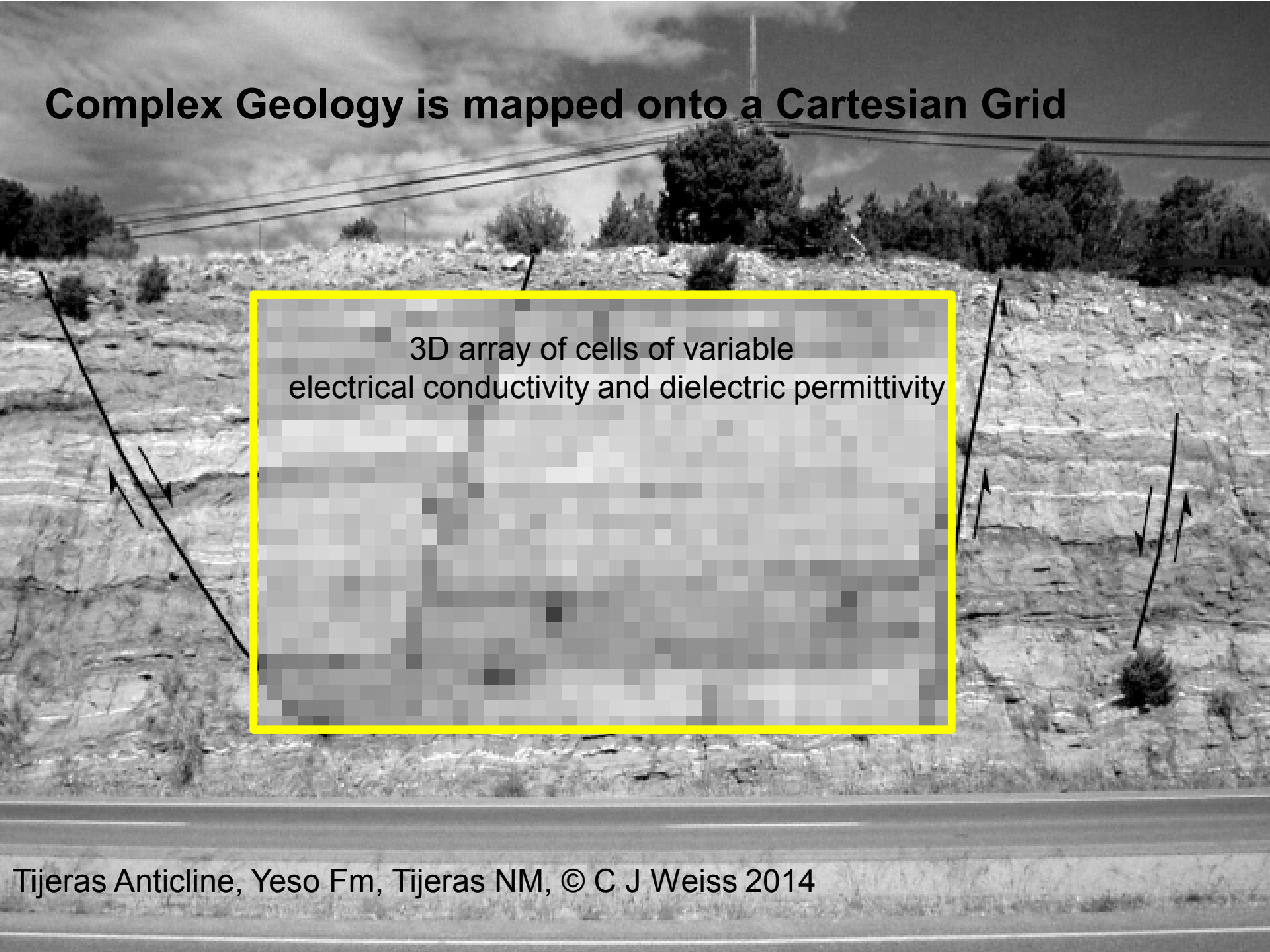

Tijeras Anticline, Yeso Fm, Tijeras NM, © C J Weiss 2014

Complex Geology is mapped onto a Cartesian Grid

Generalized Maxwell's equations are solved on cell edges and face centers by finite differences

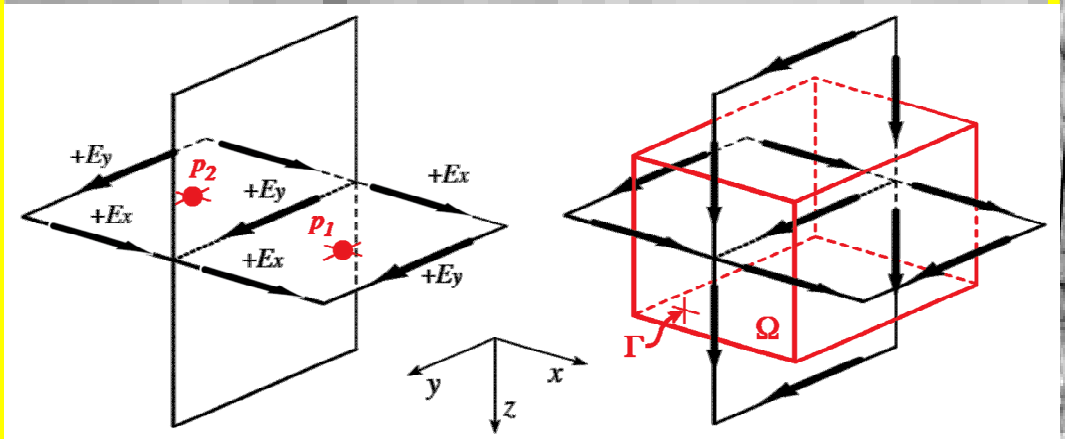

Tijeras Anticline, Yeso Fm, Tijeras NM, © C J Weiss 2014

2-level hybrid Parallel Optimization

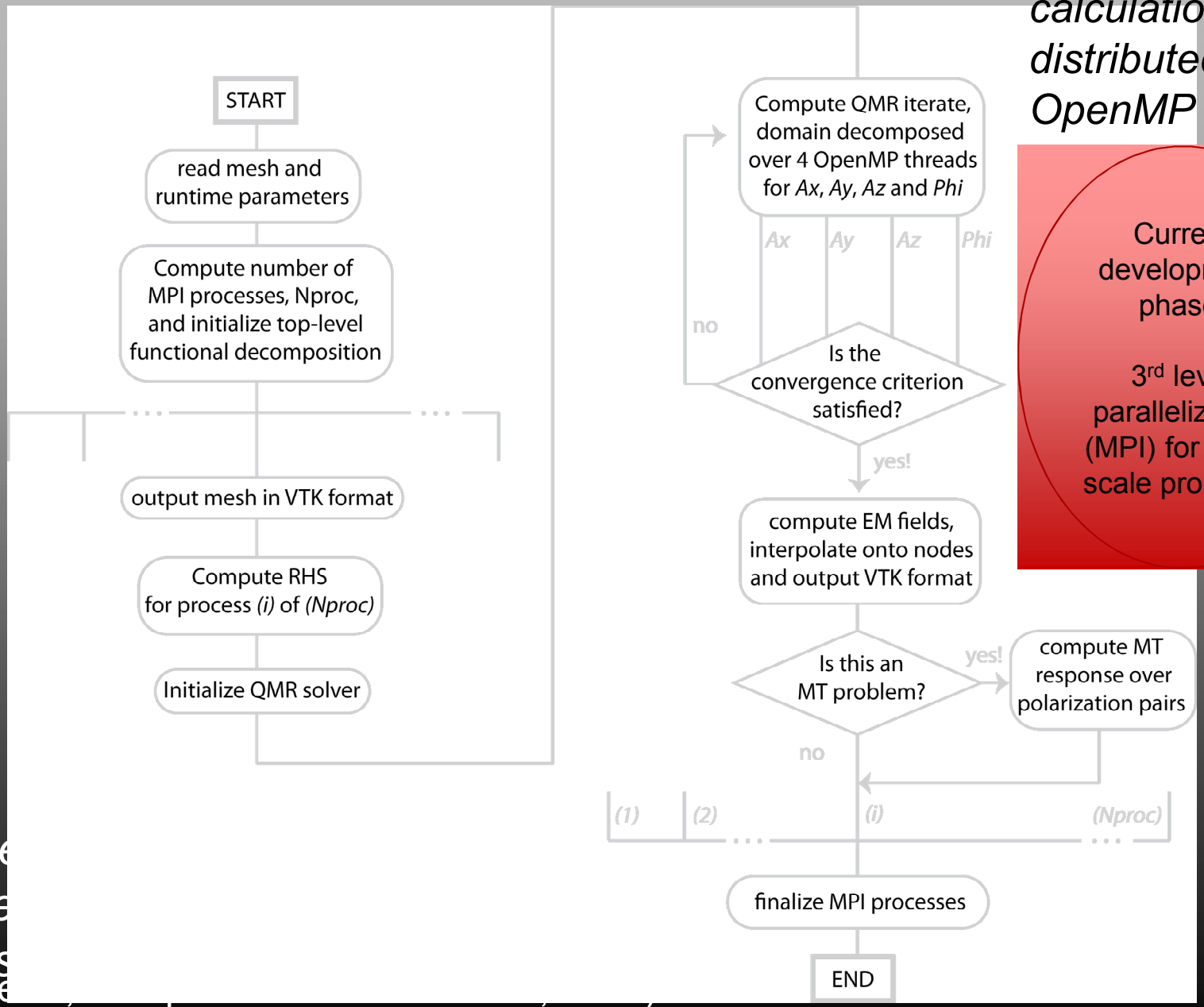

Forward calculations distributed over 4 OpenMP threads

Current development phase:

3rd level parallelization (MPI) for HPC-scale problems

Freque
source
proces
(C J We

Capturing Full EM physics across 12 decades of frequency

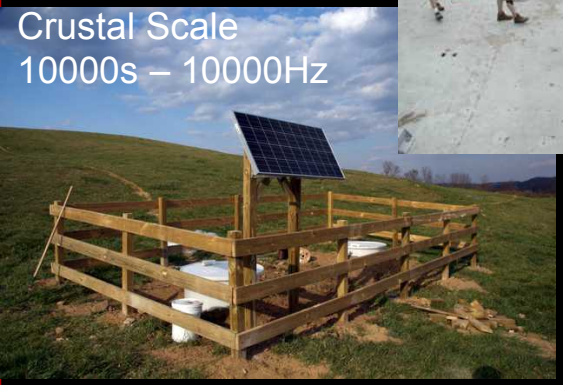

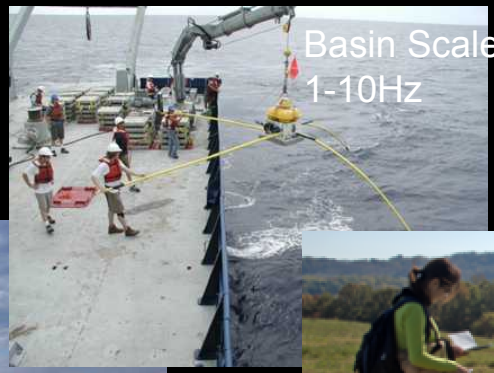

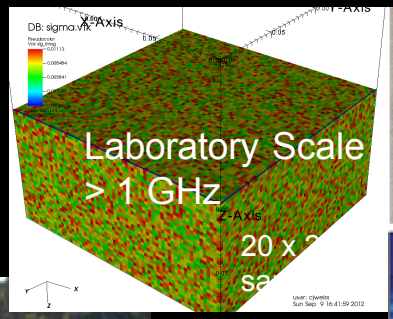

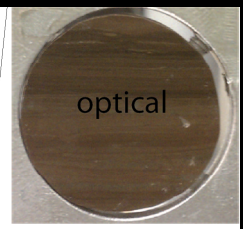

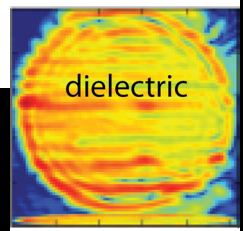

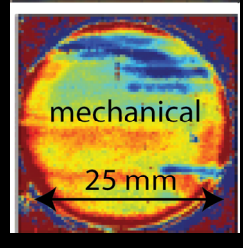

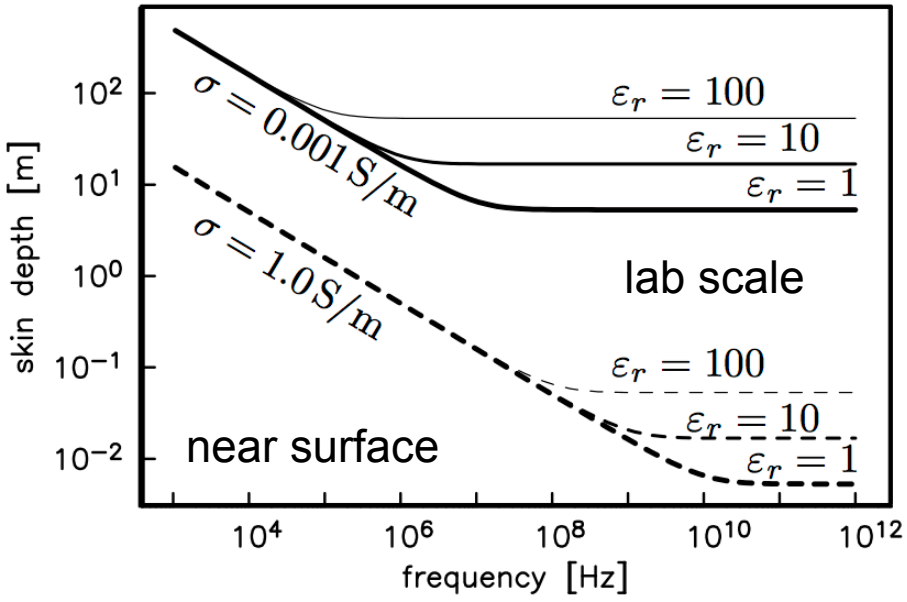

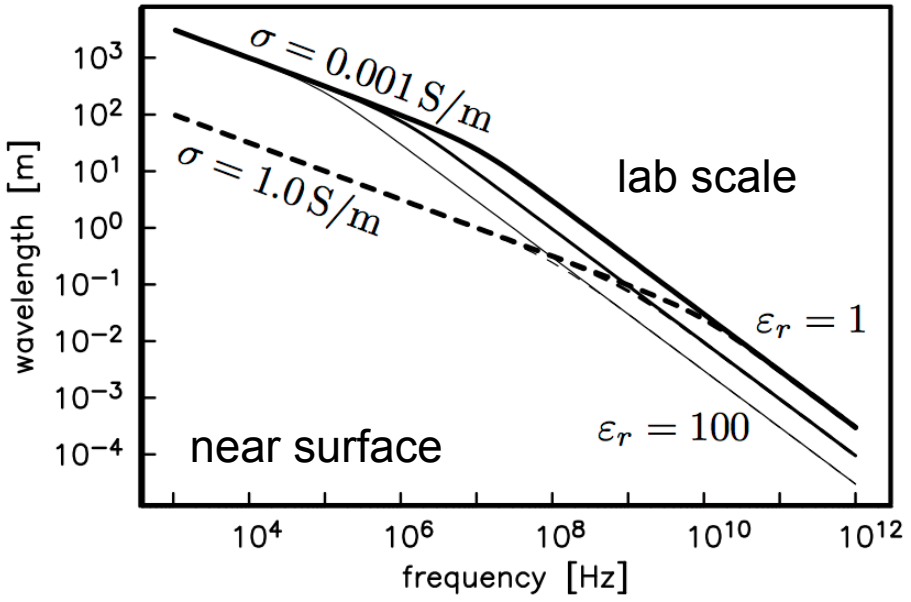

Benchmark problem #2: marine CSEM (f ~ 1 Hz)

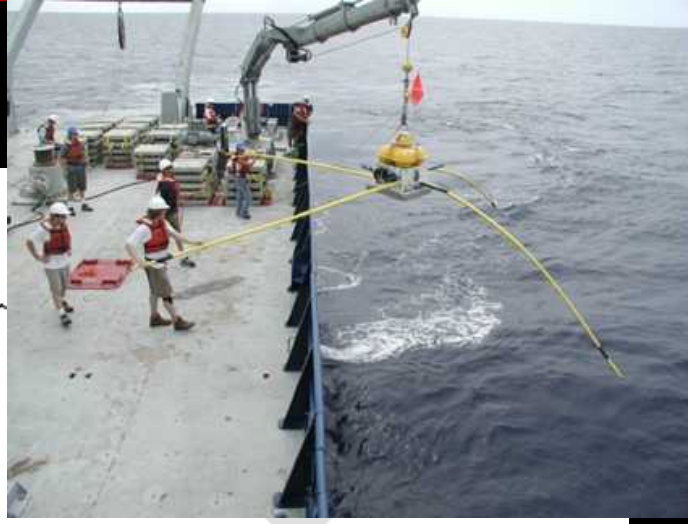

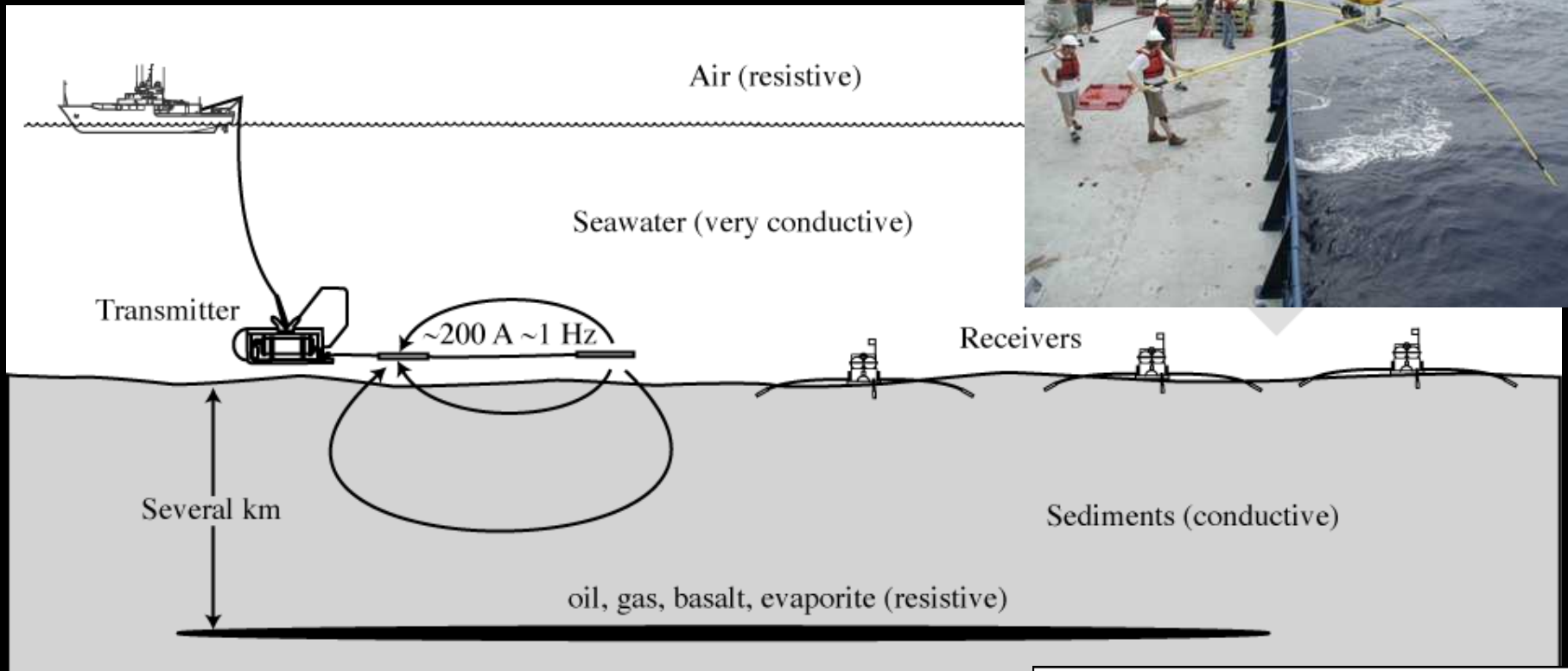

Choosing a layered conductivity model $\sigma(z)$ and a horizontal electric dipole source retains full A-Phi coupling

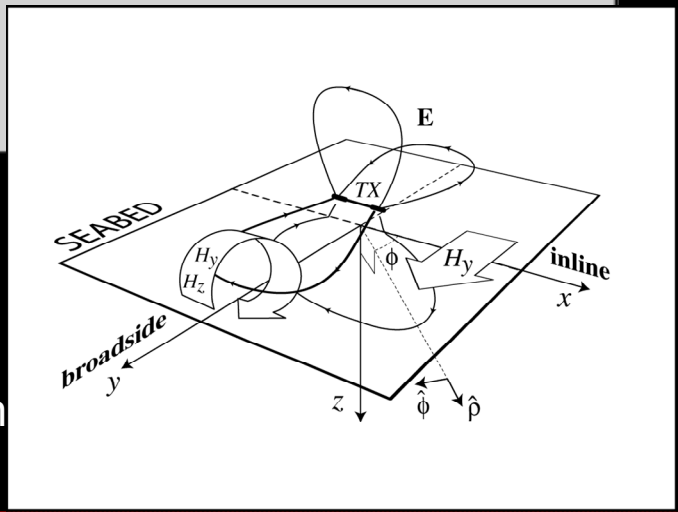

Closed form analytic solution only available in the mixed Fourier-Hankel domain.

Options for HT computation: digital filters (e.g. Anderson, 1979; Guptasarma and Singh 1997; Kong, 2007), Gaussian quadrature (Chave, 1983) or some optimized variants

Benchmark problem #2: CSEM shallow water (f ~ 1 Hz)

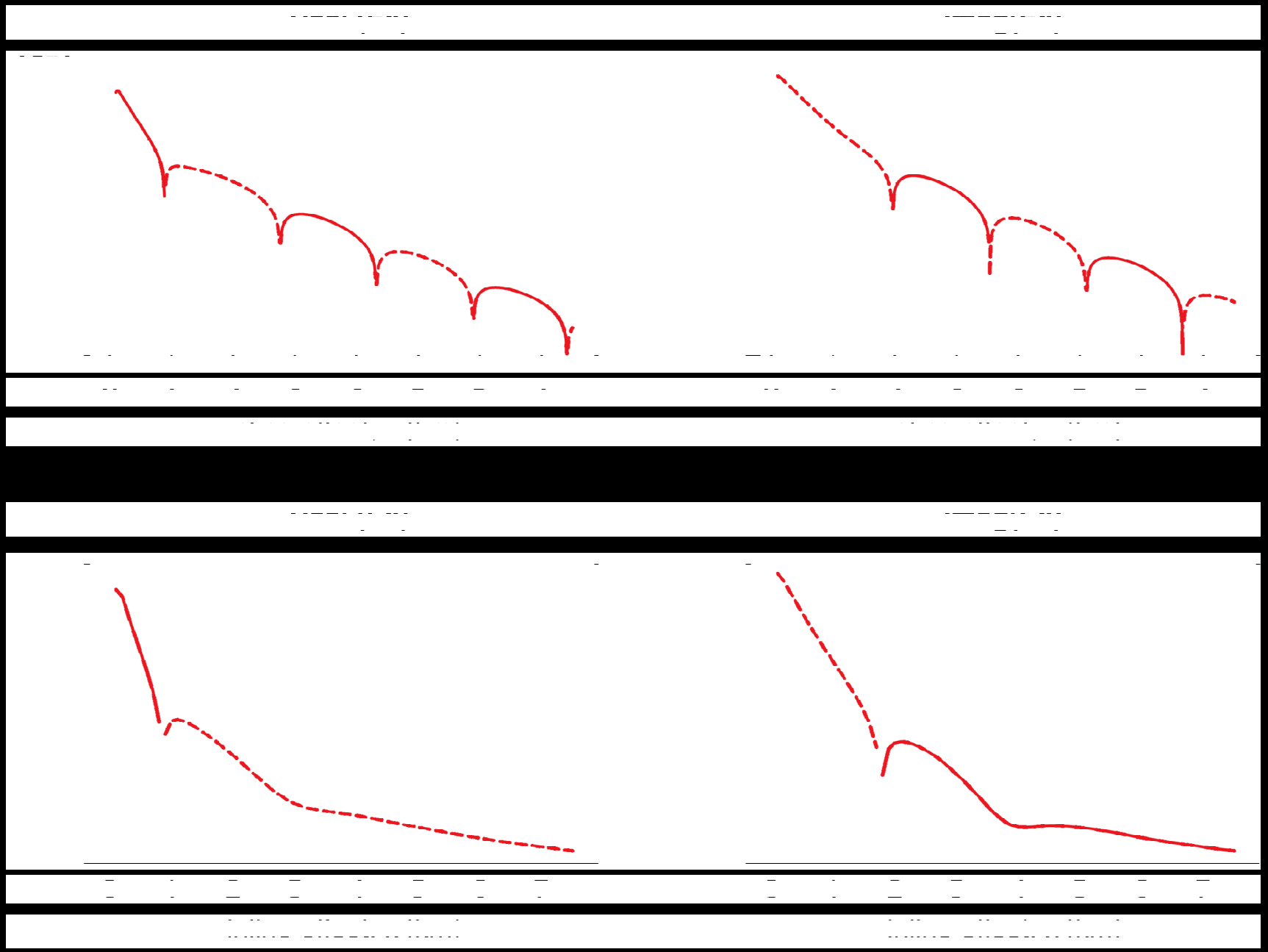

Benchmark #3: ground conductivity meter (f ~ 1kHz)

Inductive loop antenna pair
f = 0.4, 1.6 and 6.4 kHz
spacing = 10, 20 and 40 m

fast, rapid reconnaissance mapping, easy to intrepret in 1D

VT PhD Student Sharmin Shamsalsadati collecting EM34-data at Kentland Farms field Station, McCoy VA

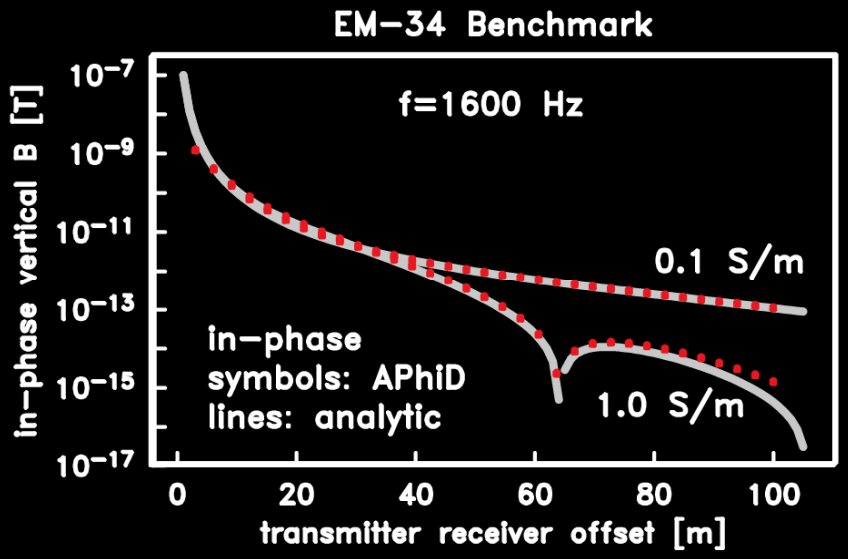

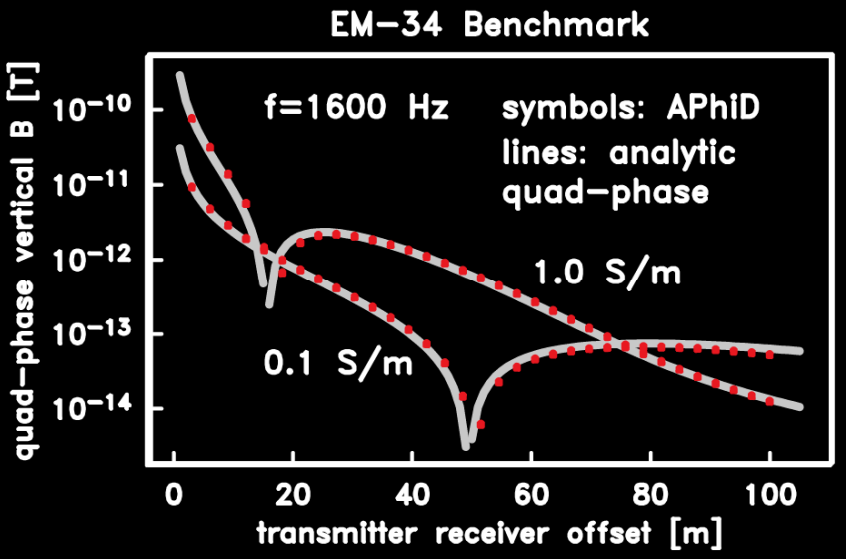

Parallel multi-grid discretization (Weiss, GJI 2014)

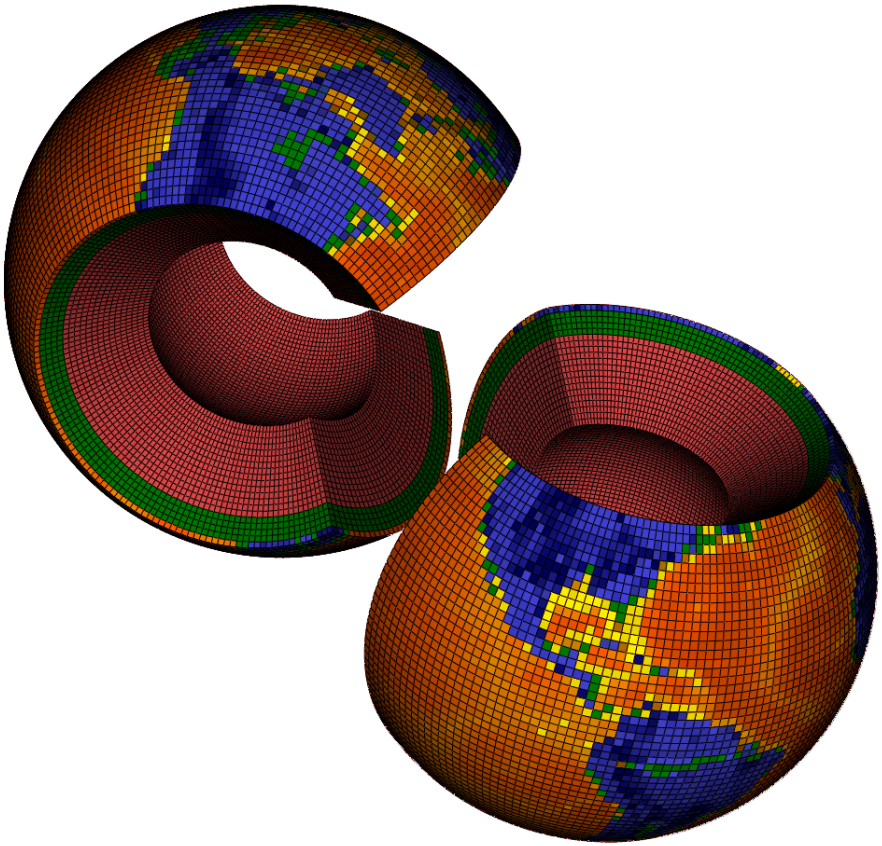

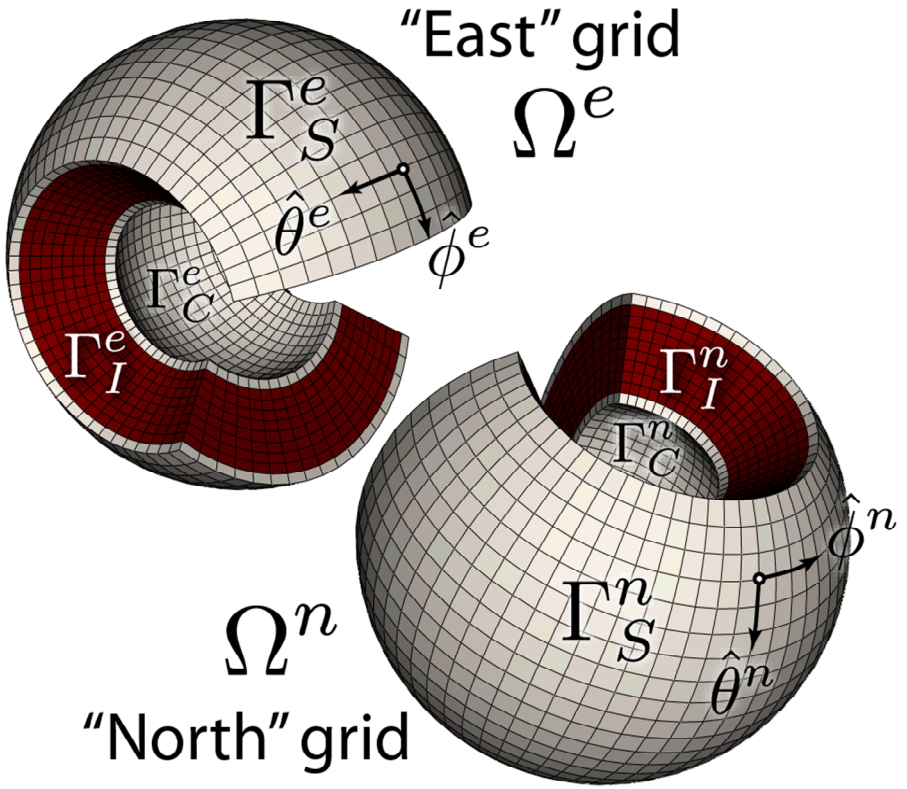

Borrow a page from the book of EM calculations on a sphere (Weiss, Geophys J Int, 2014).

1. decompose the mesh into partially overlapping grids
2. solve for the fields in parallel over each mesh
3. interpolate on the overlap regions for mesh-to-mesh consistency

Overlap control, mesh refinement and interpolation

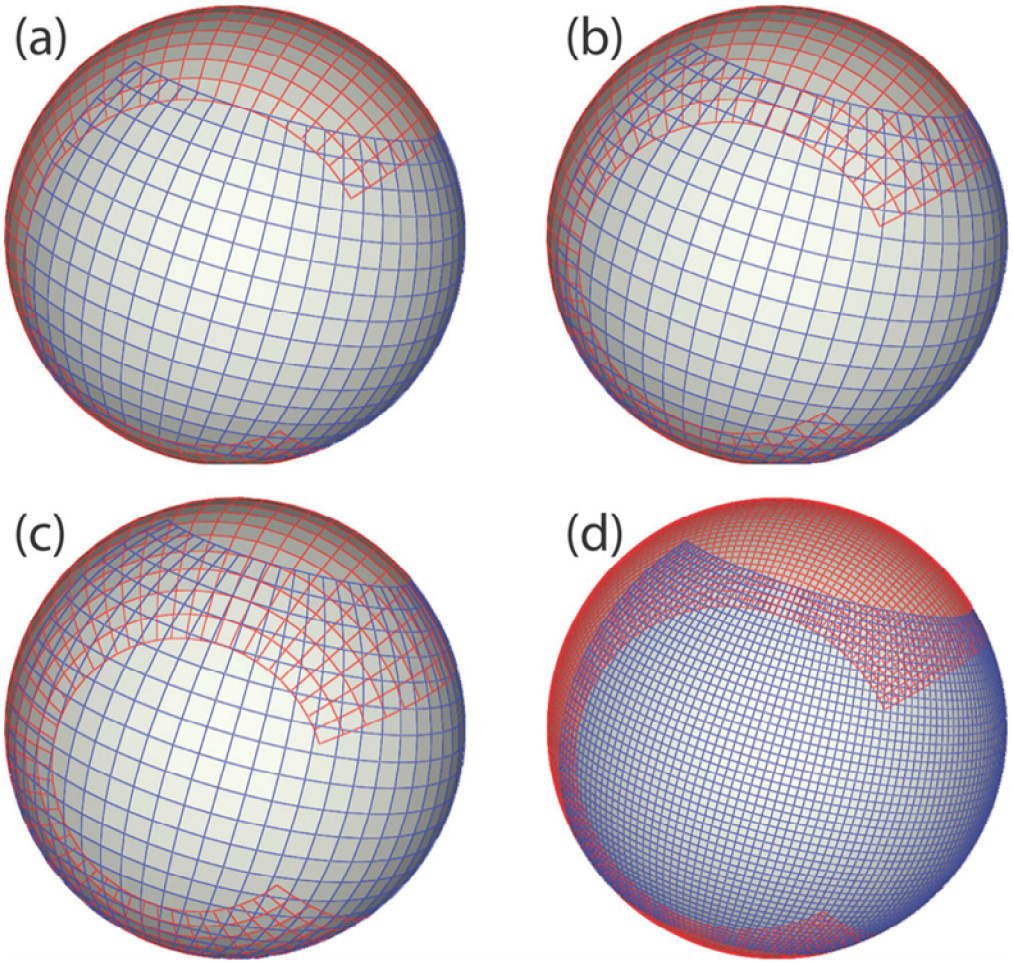

global scale grids with variable mesh refinement and overlap

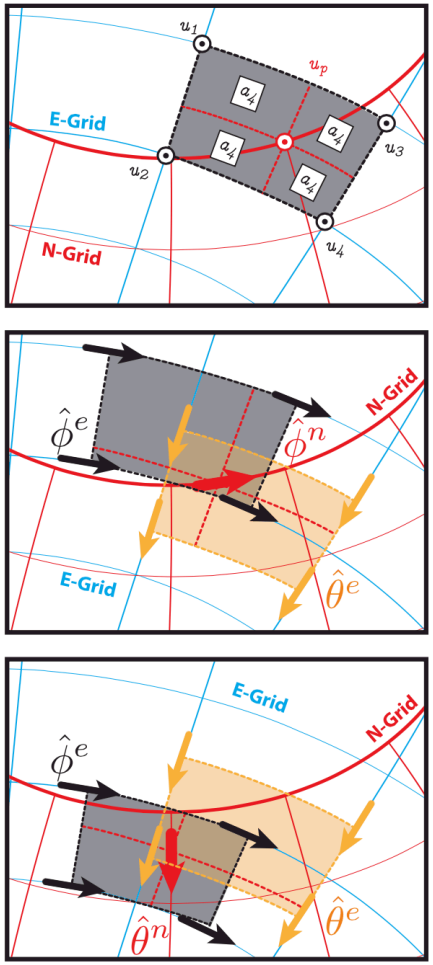

interpolation templates

Weiss, GJI, (2014)

3D numerical modeling toolkit:
Project SOAP, aka “son of A-Phi”

Sandia National Laboratories

GEOPHYSICS, VOL. 75, NO. 1 (JANUARY-FEBRUARY 2010); P. F33–F50, 14 FIGS., 2 TABLES.
10.1190/1.3278525

Geophysics

journal homepage: library.seg.org

High-order finite-difference simulations of marine CSEM surveys using a correspondence principle for wave and diffusion fields

Rune Mittet
EMGS AS, Trondheim Norway. rm@emgs.com

the BIG idea: recast the low-frequency diffusion problem into a well-posed, *lossless*, and comparatively easy wave propagation problem (BIG grids, low resource footprint)

SNL’s SOAP code benchmarked against 1D analytic Green’s function solutions (induction only) and CSEM geometries (full 3D physics: induction + galvanic).

3D numerical modeling toolkit:
Project SOAP, aka “son of A-Phi”

Weiss and Constable (Geophysics, 2006)

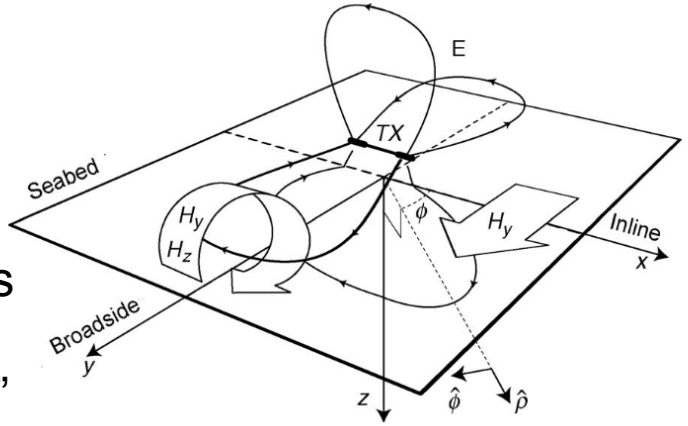

electric dipole source over the seabed drives currents both parallel and normal to conductivity interfaces, therefore providing a rigorous test of the “full physics”

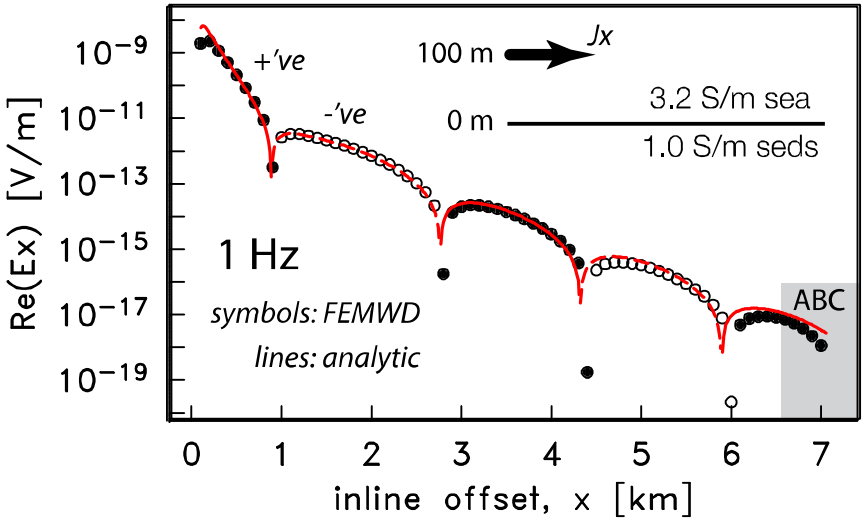

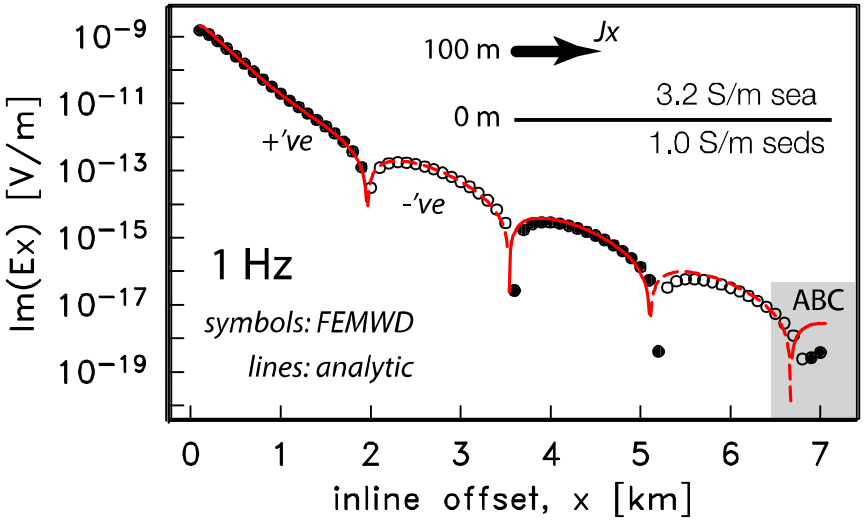

CSEM benchmark example
numeric (symbols) –vs– analytic (lines)

Rapid Optimization Library (ROL)

RAPID OPTIMIZATION LIBRARY

Sandia National Laboratories

- ROL is a new Trilinos package for large-scale continuous optimization, a.k.a. nonlinear programming (NLP).
- Available in Trilinos since 10/21/2014.
- Developers: Drew Kouri, Denis Ridzal, Greg Von Winckel, Bart van Bloemen Waanders
- ROL includes:
  - A rewrite and consolidation of existing optimization tools in Trilinos: *Aristos*, *MOOCHO*, *Optipack, Globipack.*
  - Hardened, production-ready algorithms for unconstrained and equality-constrained continuous optimization.
  - Methods for efficient handling of inequality constraints.
  - A unified interface for simulation-based optimization.
  - New methods for efficient handling of inexact computations.
  - New methods for optimization under uncertainty.

Estimating basal friction of ice sheets.

- Interface to LifeV Project (www.lifev.org).

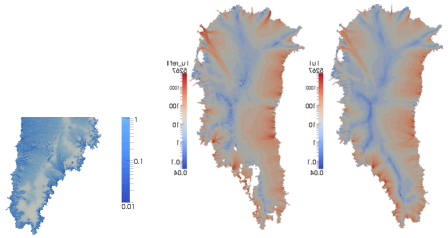

- **65K distributed optimization variables**
- 700,000 state variables

Inverse problems in acoustics / elasticity.

- Interface to the Sierra-SD structural dynamics code

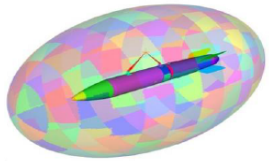

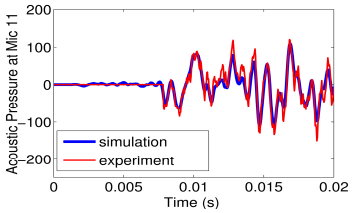

1M optimization variables, 1M state variables

EM Modeling of Multi-scale Geologic Heterogeneity

von Kármán representation? No.

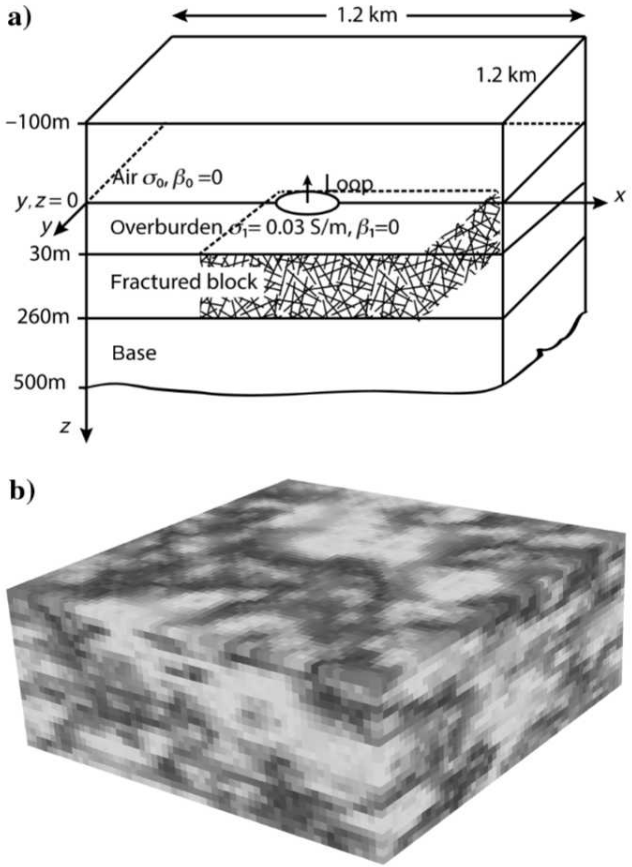

Figure 7. (a) The 3D fractured model and (b) the stochastic conductivity model of the fractured block, in which the darker gray denotes conductive anomalies, and the lighter gray denotes less conductive regions.

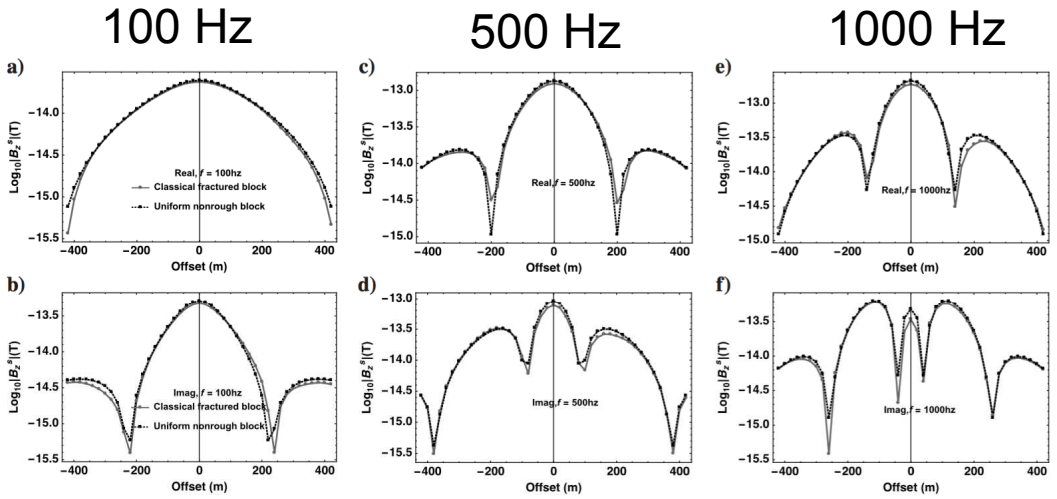

Figure 12. Comparisons between the classical von-Kármán-type ($\nu = -0.1$) fractured model responses (solid line) and responses to the unique nonrough block model (dashed line) at $f = 100$, 500, and 1000 Hz. The conductivity of the nonrough block is 0.045 S/m.

Comparison between von Kármán-type ”fracture model” and equivalent homogeneous block for several interrogation frequencies.

Demonstrates the vK models have a classical, homogeneous equivalent model.

Ge et al., Geophysics (2015)

Line Integral Convolution (LIC)

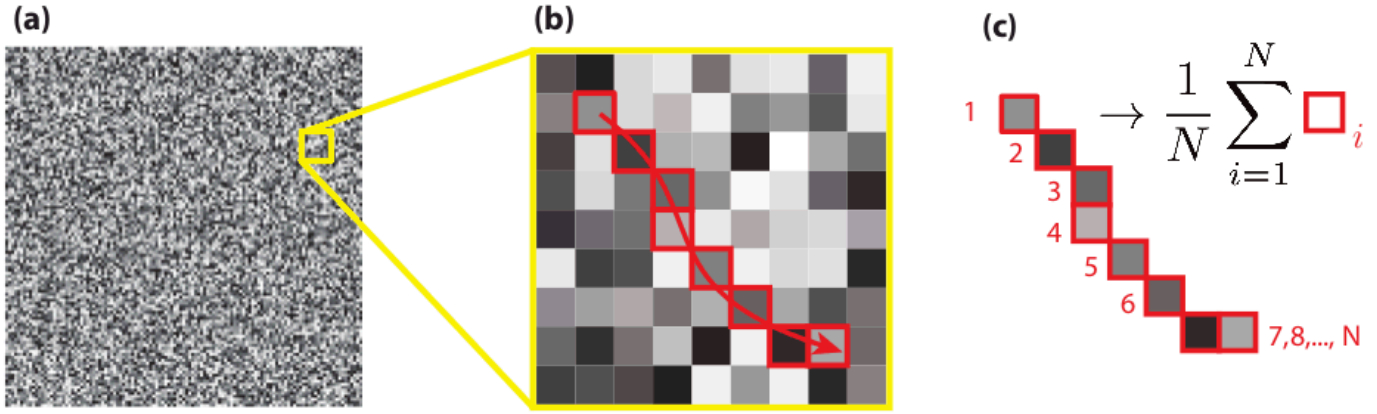

(d)

$$\mathbf{f}(x,y,z) = u(x,y,z)\hat{x} + v(x,y,z)\hat{y} + w(x,y,z)\hat{z}$$

$u(x,y) = 1$ $v(x,y) = \sin(x)$
$u(x,y) = 1$ $v(x,y) = 0.3$

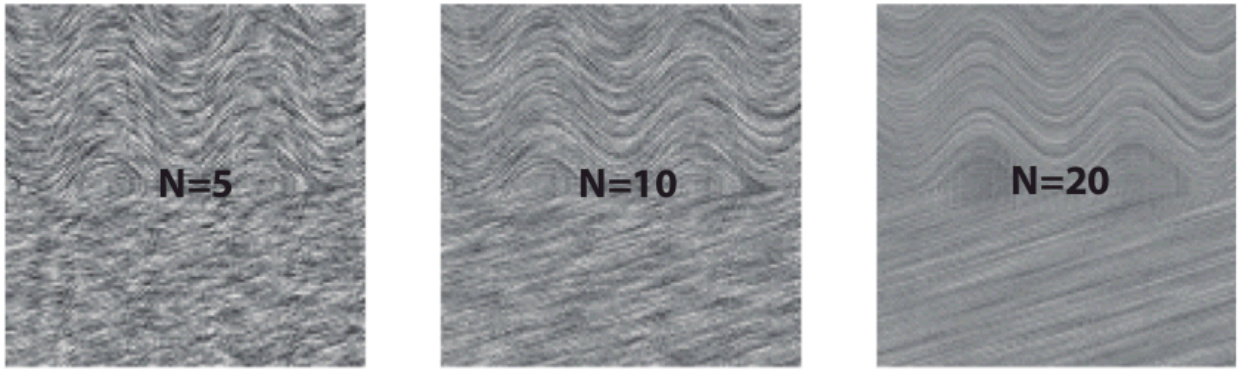

Correlation through convolution length.
Texture defined through the convolving vector field.

Beskardes et al., GJI (2017)

LIC Models of simple geotextures

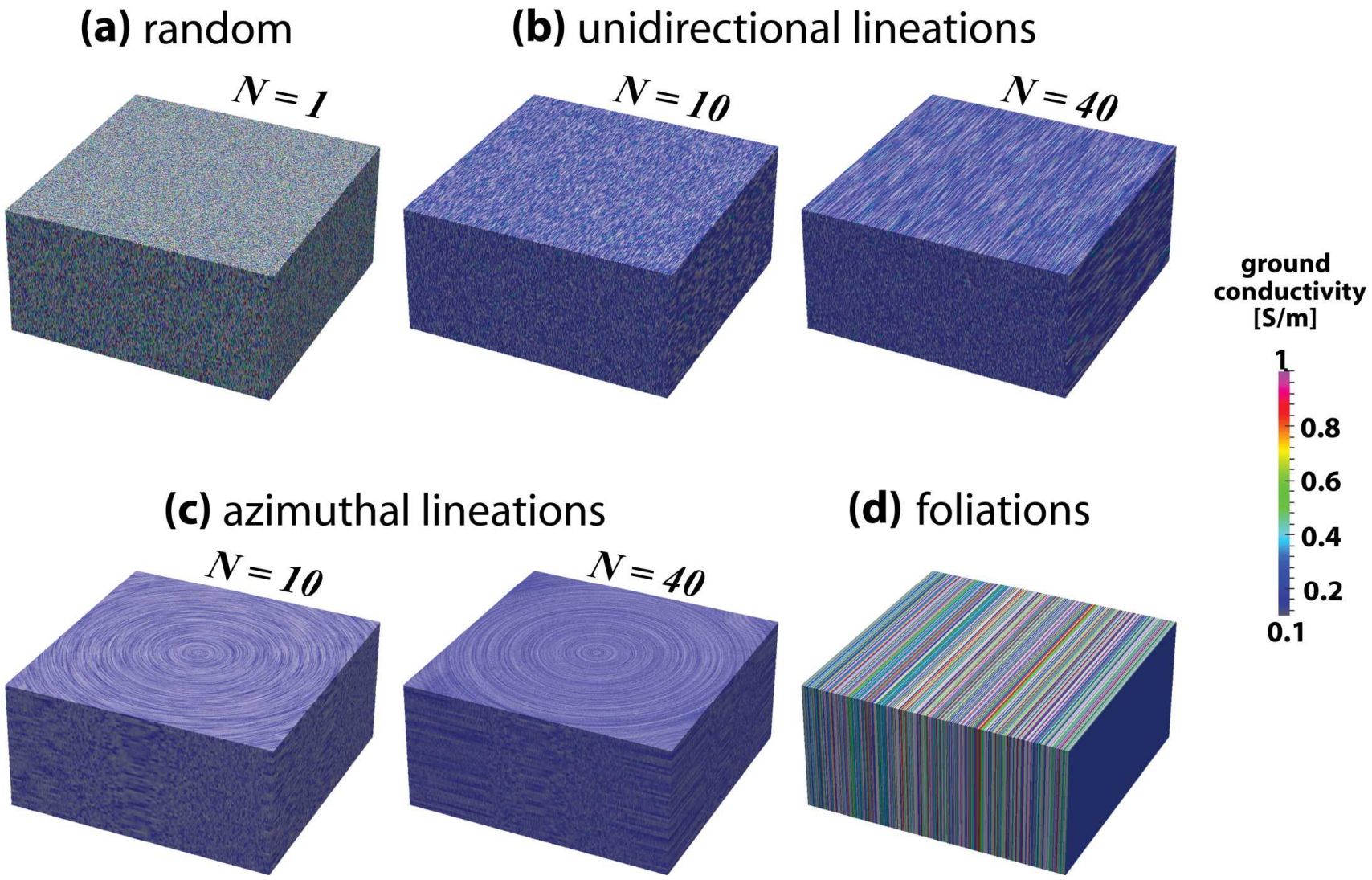

Beskardes et al., GJI (2017)

Simulated azimuthal LIC response

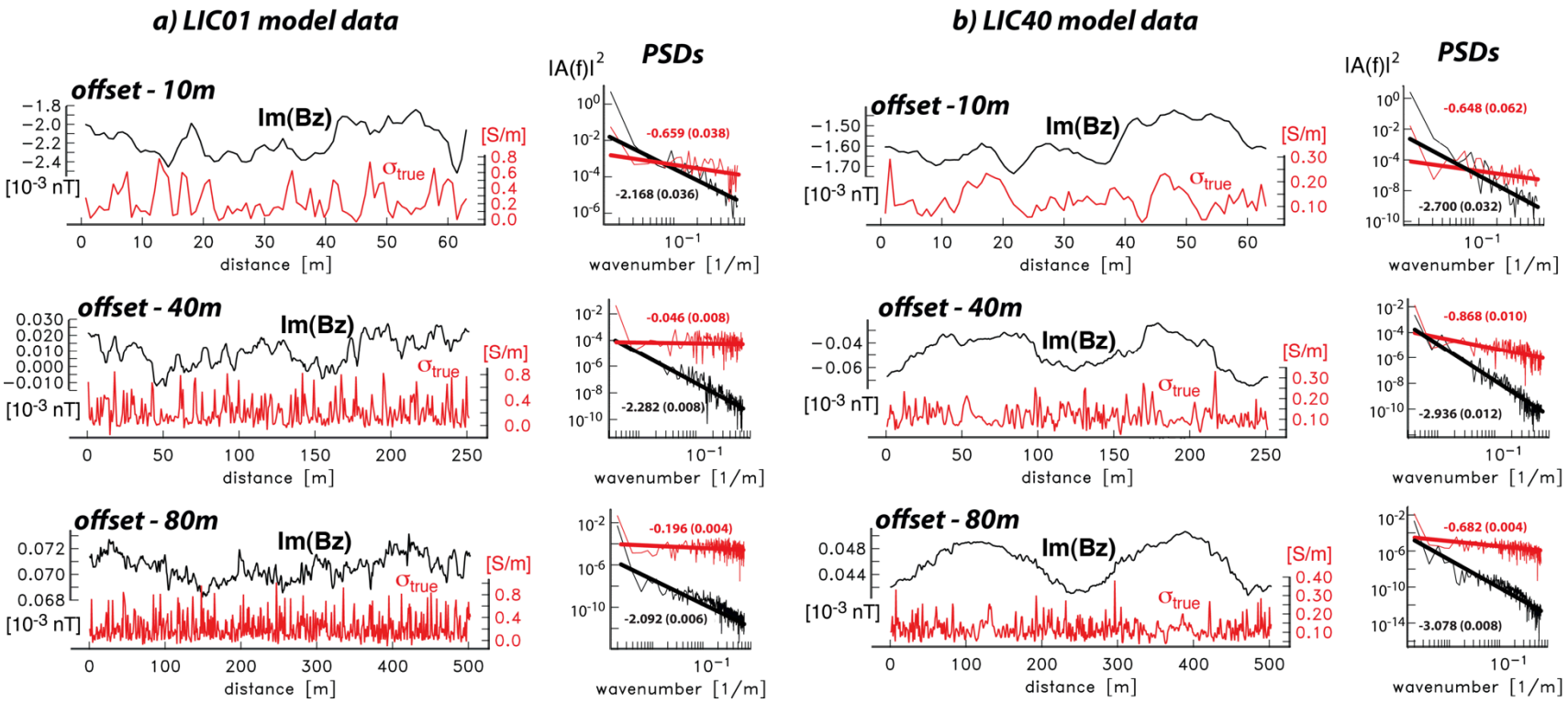

Statistically a fractional Brownian motion (fBm) signal
Consistent with observed data.

Beskardes et al., GJI (2017)

Simulated azimuthal LIC response

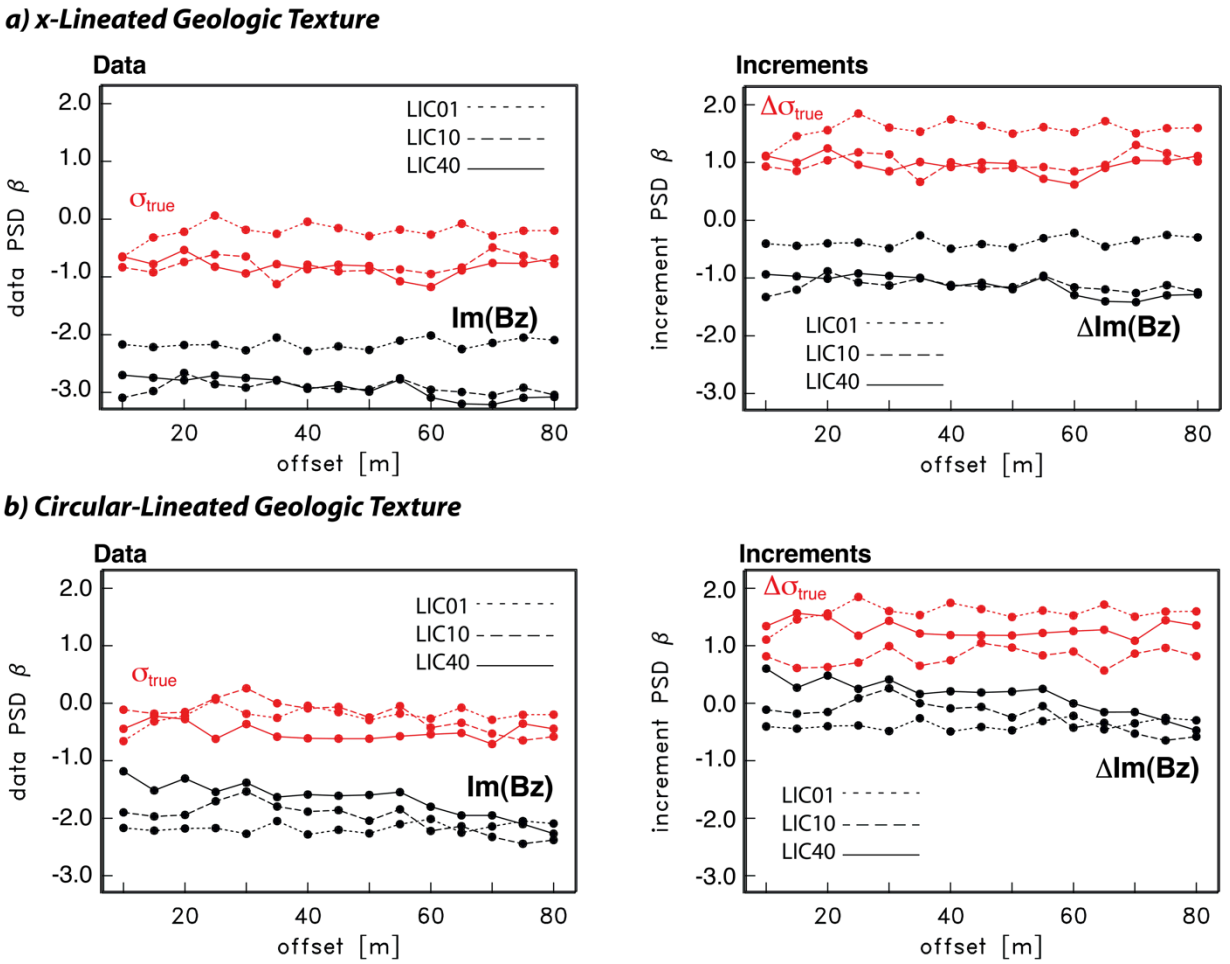

Statistics are robust over variable transmitter/receiver spacing

Beskardes et al., GJI (2017)

Isn't it just anisotropy? No.

GEOPHYSICS, VOL. 67, NO. 4 (JULY-AUGUST 2002); P. 1104–1114, 11 FIGS., 1 TABLE.
10.1190/1.1500371

journal homepage: library.seg.org

Electromagnetic induction in a fully 3-D anisotropic earth

Chester J Weiss and Gregory A Newman
Sandia National Laboratories, cjweiss@sandia.gov

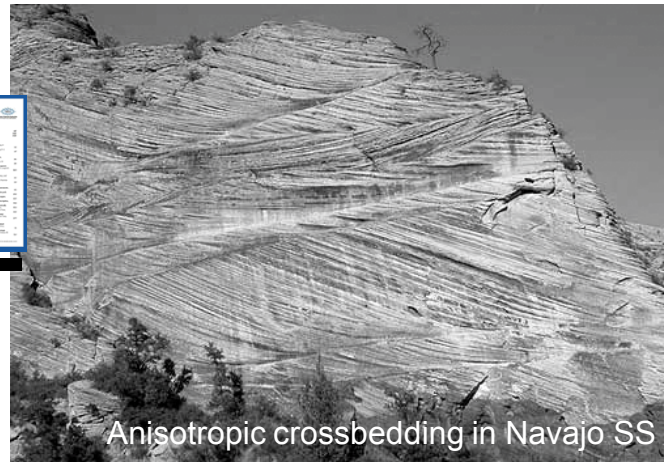

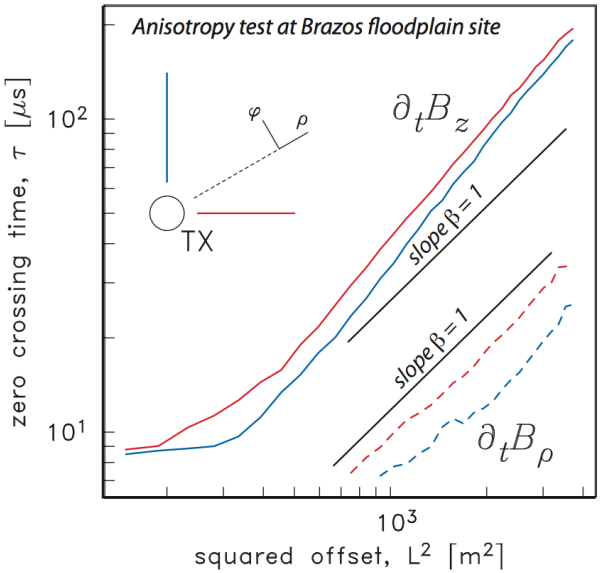

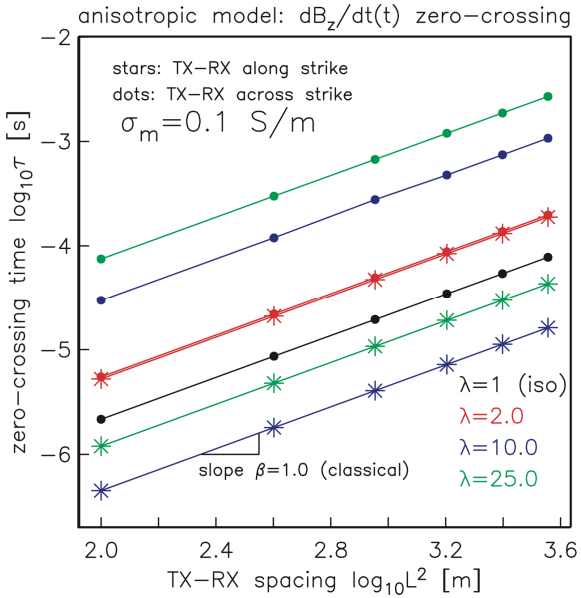

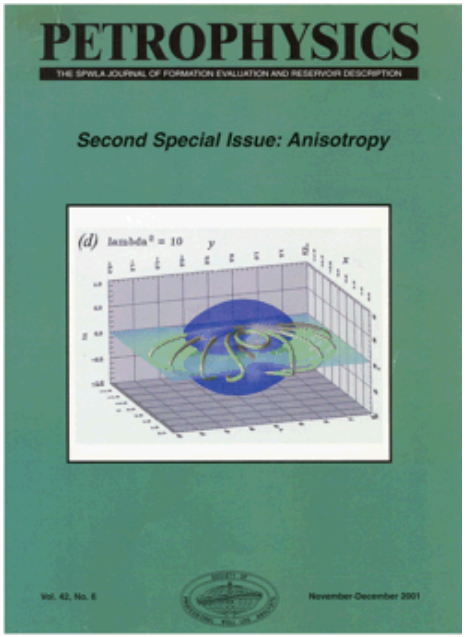

Weiss et al., (2001), Weiss and Everett (2007)

Fracture Detection with DC Methods

Weiss et al., (2015, 2016)

Finite element forward solver: Benchmark test

Solve for electric scalar potential Φ over an arbitrary conductivity model σ excited by a source current $\mathbf{J}_s$:

$$-\nabla \cdot (\sigma \nabla \Phi) = \nabla \cdot \mathbf{J}_s$$

Homogeneous Dirichlet BC on mesh bottom and sides, Neumann BC on mesh top to simulate air/Earth interface.

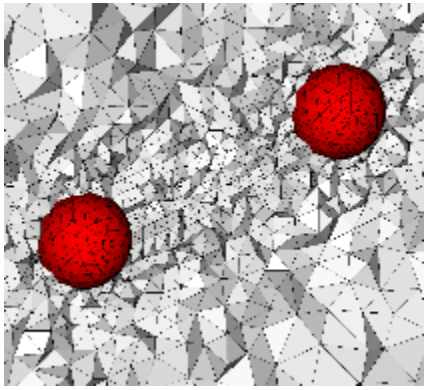

(right) *finite element mesh for benchmark comparison against analytic solution of 2 spheres in a wholespace (Aldridge and Oldenburg, Geophysical Prospecting, 1989)*

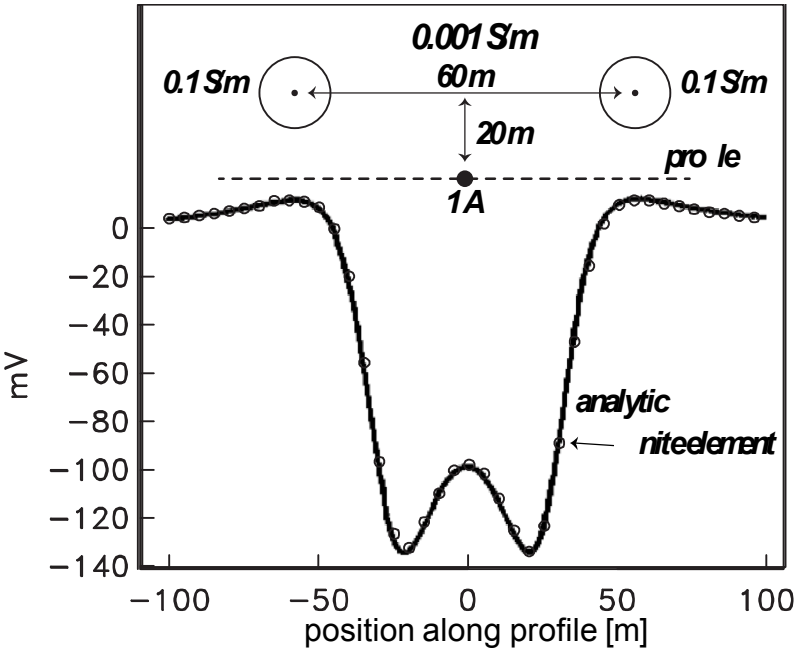

(above) *comparison of finite element and analytic solutions of scattered electric potential for an offset point source*

Problem Statement and Approach

- Given an induced fracture system in a horizontal well with elevated electrical conductivity, what can be said about the fractures from surface measurements of DC potential differences?
- Forward model the Earth/borehole/fracture system with unstructured finite elements conformal to conductivity boundaries
  - compute the prefrack, postfrack and pre-post DC potential differences
  - parametric analysis of fracture conductivity effect
  - quantify topographic effects
  - linear inversion synthetic responses for simple fracture mapping

Earth model of exploration scenario

*Idealized **(below)** and discretized **(right)** Earth model for finite element analysis (FEA). Electrode location indicated by symbols, with 3 possible contact points (A-C) of the +'ve electrode with steel well casing.*

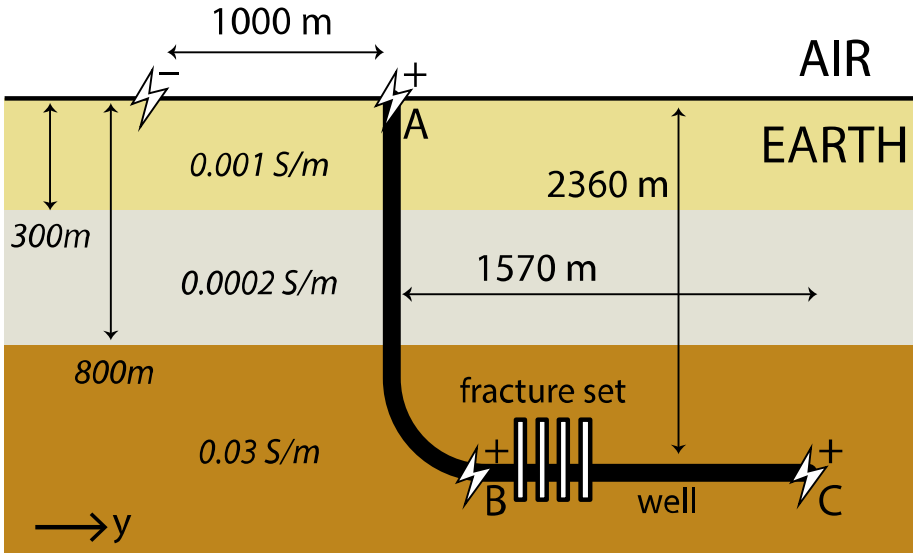

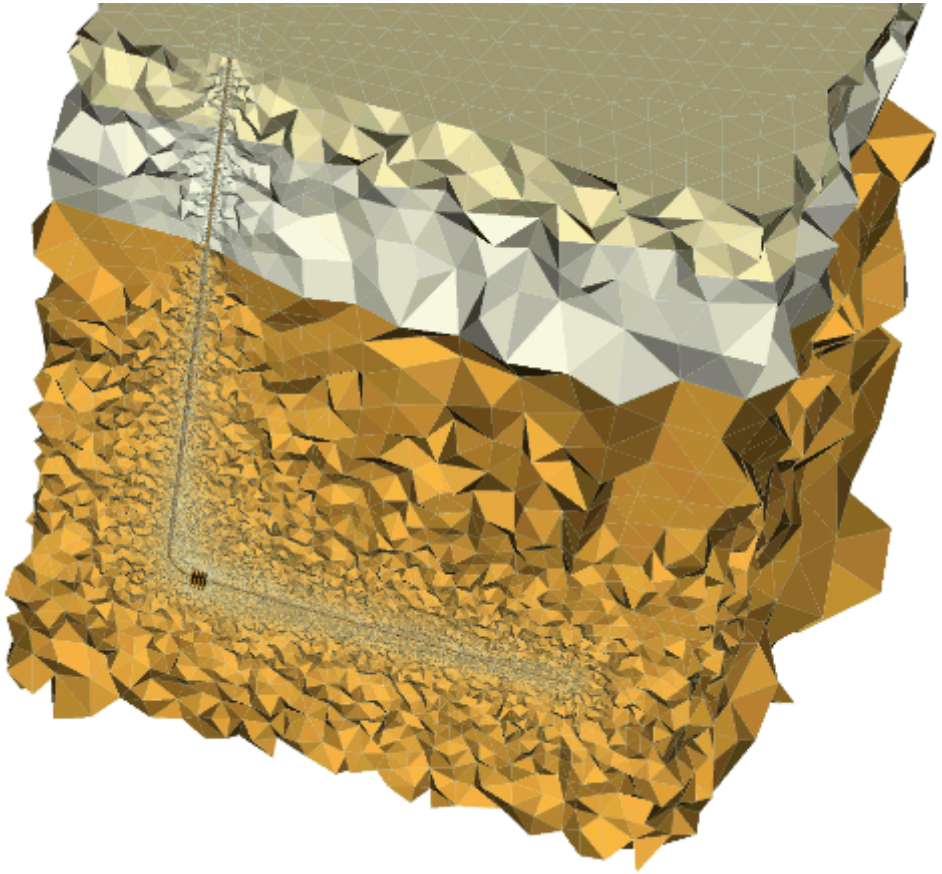

DC potential on the ground over the well head

(left) Plan view of electric potential (in Volts) at Earth's surface (z = 0 m) over the well head (x = y = 0 m) where the Earth model is energized by +1 A current source at the well head (case A) and a –1 A sink at y = 1000 m.

(right) Potential difference (in microvolts) at z = 0 m computed by subtracting the response of the Earth model with a set of 10 S/m fractures from one where the fractures are absent, thus simulating a time-lapse scenario for detection of electrically enhanced fractures.

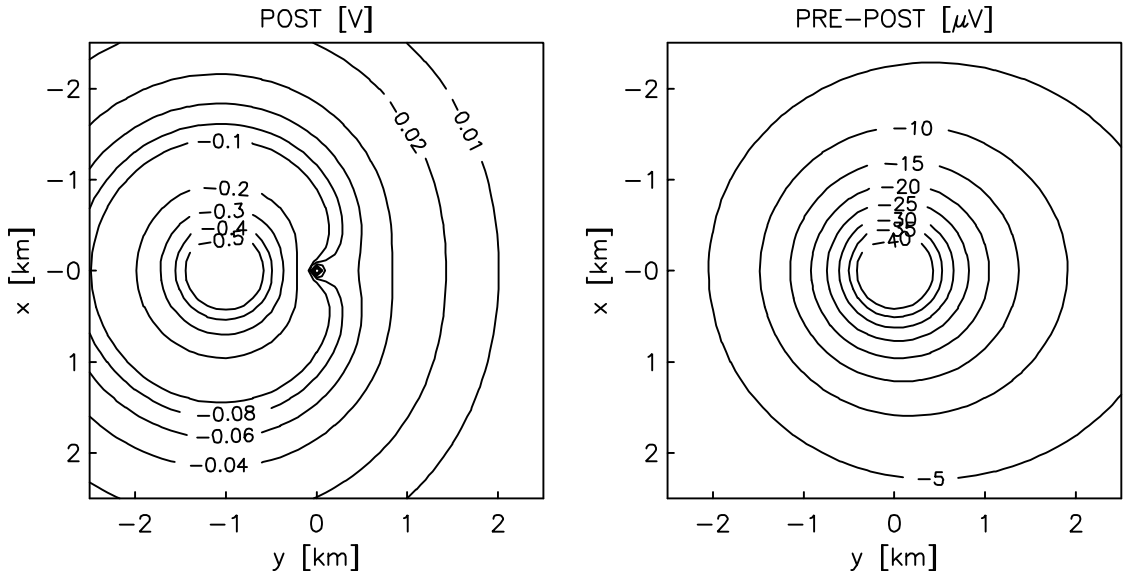

How do the ground-based measurements arise?

Oblique view of the magnitude of electric potential for case A (+'ve electrode at the well head) along two intersecting surfaces: a vertical slice at x = 0 m through the well track and fracture set; and, a horizontal slice at z = 0 m along the air/Earth interface.

Intersecting the slices are the well track and fractures. Note the local perturbation near the well heel due to the fractures, as well as the dominance of the –1 A current source on the potentials at z = 0.

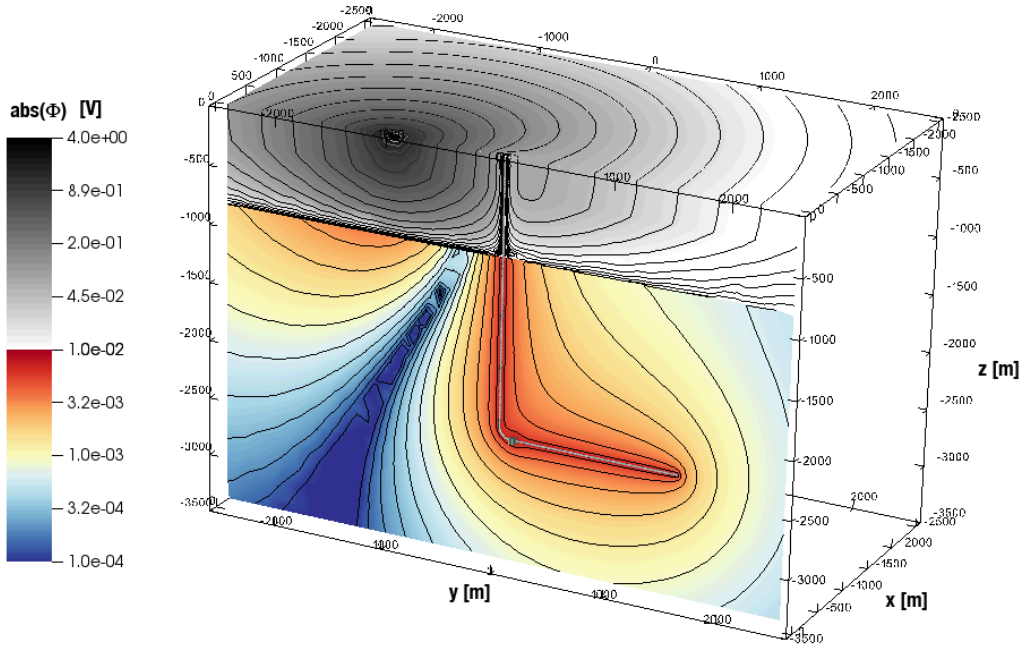

Generally small amplitudes of the potential in the region below z = −800 m are consistent with its relatively high 0.03 S/m conductivity – in contrast to the low (< 0.001 S/m) conductivity in the region above z = −800 m.

Topography effect: 3D-1D residual

Topography: 860m to 970m elevation

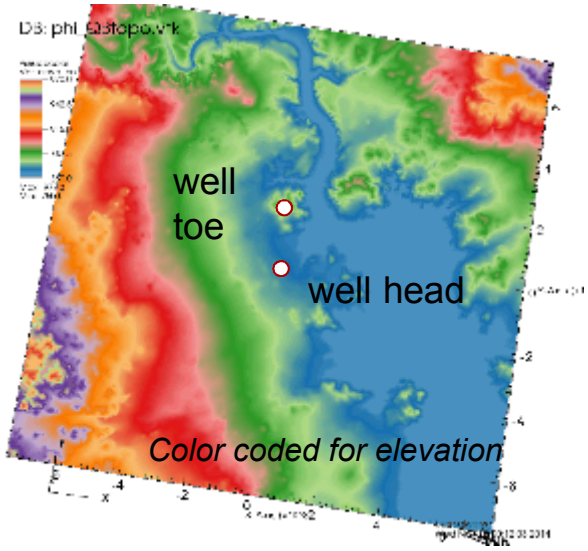

3D DC FEA calculation w/ topo

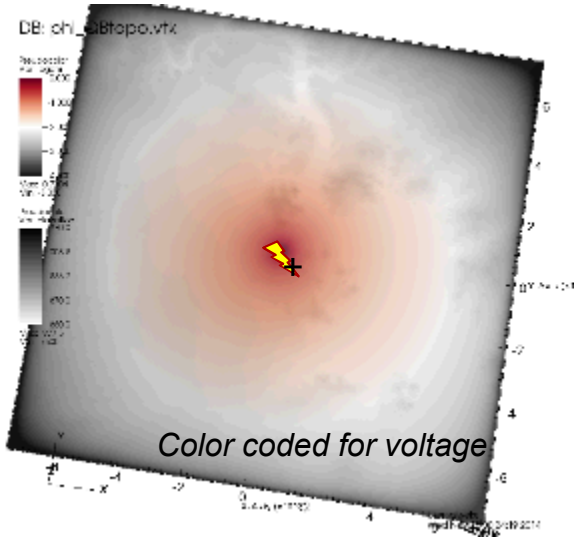

topo – flat FEA residual

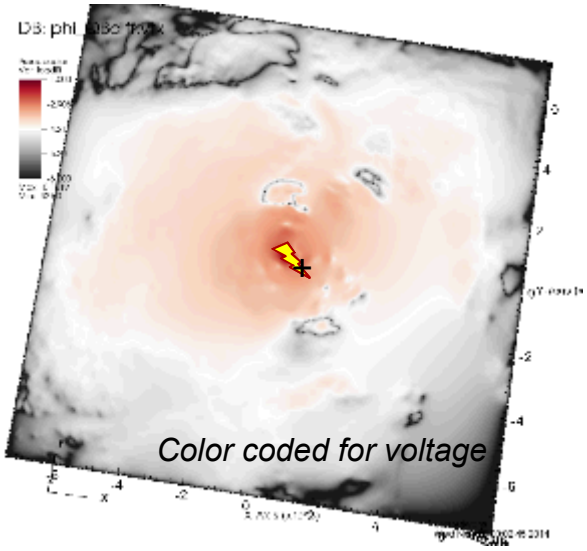

~1% change in voltage due to topography

This relative magnitude is comparable to the change expected from electrically conductive fracture set.

Predicted data for inline measurement array

(top curve) Potential difference along line x = 0 directly through the well head and over the horizontal section of the well, in the absence of conducting fractures for 1 A source located at the well head (case A) and –1 A source at y = −1000 m. Dashed lines indicate negative values; solid lines, positive.

(bottom curve) Scattered potential differences arising from a 10 S/m fracture set near the heel of the well bore.

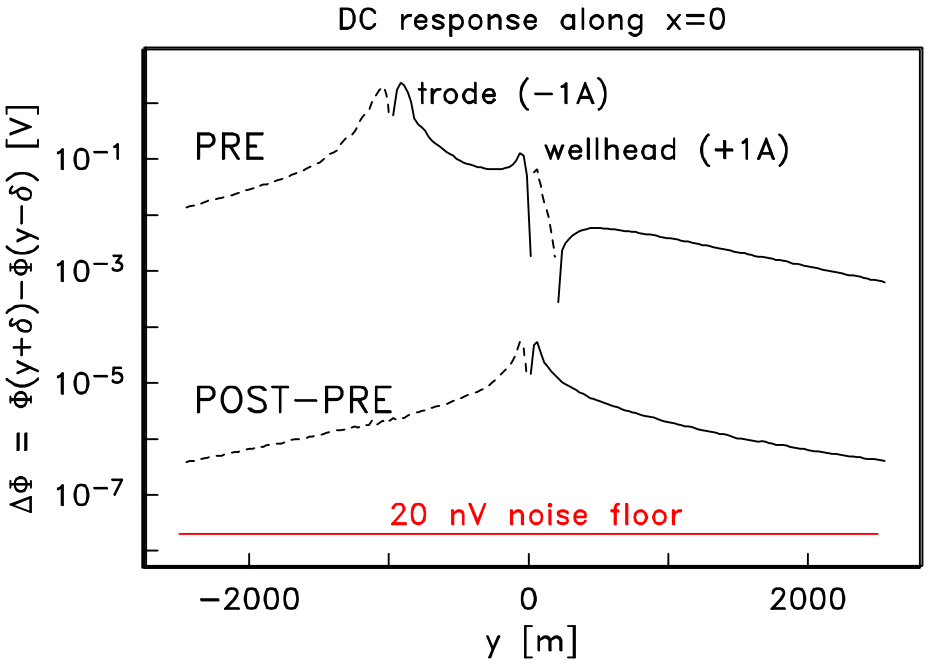

Potential differences computed using 100 m electrode separation, δ = 50 m. For reference, also shown is the 20 nV noise floor for the 32-bit ZEN receiver from Zonge Engineering (http://zonge.com/instruments-home/systems/distributed-em-systems/).

Effect of source location and fracture conductivity

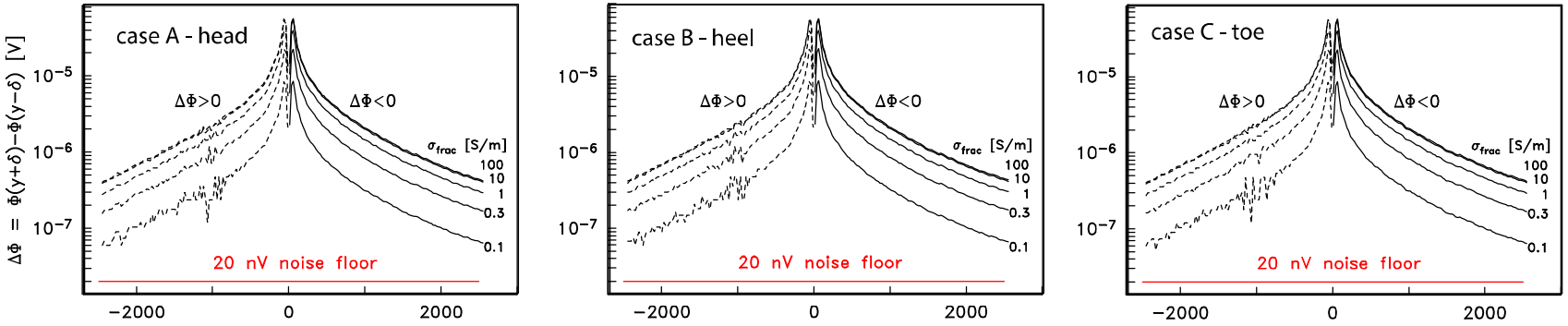

Inline scattered potential differences (δ = 50 m) as a function of fracture conductivity over the range 0.1–100 S/m for a –1 A source at y = −1000 m and +1 A source located at either the well head, heel, or toe (cases A-C). Dashed lines indicate negative values; solid lines, positive.

Note that location of the +1 A source has minimal effect on scattered potential differences, and that fracture response is saturated for conductivities greater than ~10 S/m.

Effect of fracture location

heel fracture

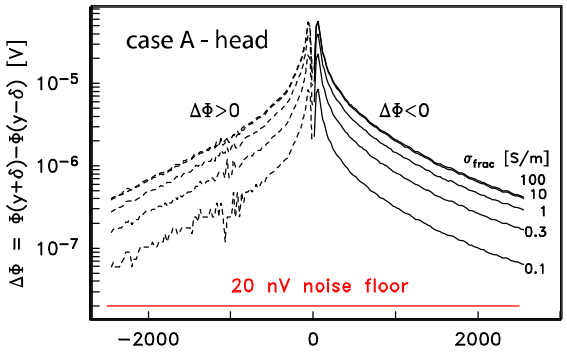

toe fracture

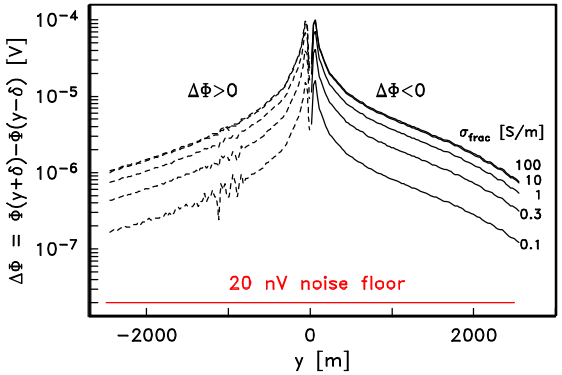

Inline scattered potential differences (δ = 50 m) as a function of fracture conductivity over the range 0.1–100 S/m for a –1 A source at y = −1000 m and +1 A source, fractures located at either the well heel **(left)**, or toe **(right)**. Dashed lines indicate negative values; solid lines, positive.

Note the pronounced left/right asymmetry of the toe-fracture result, and that fracture response remains saturated for conductivities greater than ~10 S/m.

Motivation for empirical LQS inversion

Oblique view of the magnitude of POST–PRE scattered electric potential for case A along two intersecting surfaces: a vertical slice through the well track and fracture set at x = 0 m; and, a horizontal slice along the air/Earth interface
z = 0 m.

Region where Φ > 0 is denoted by (+) whereas the region Φ < 0 is denoted by (−). Superimposed on the slices are the well bore and fractures.

Observe that this POST–PRE difference data arises primarily from a combination of sources – one due to the conductivity perturbation at the fractures, and the other, a change in the relative potential of the borehole casing due to current leakage at the fracture.

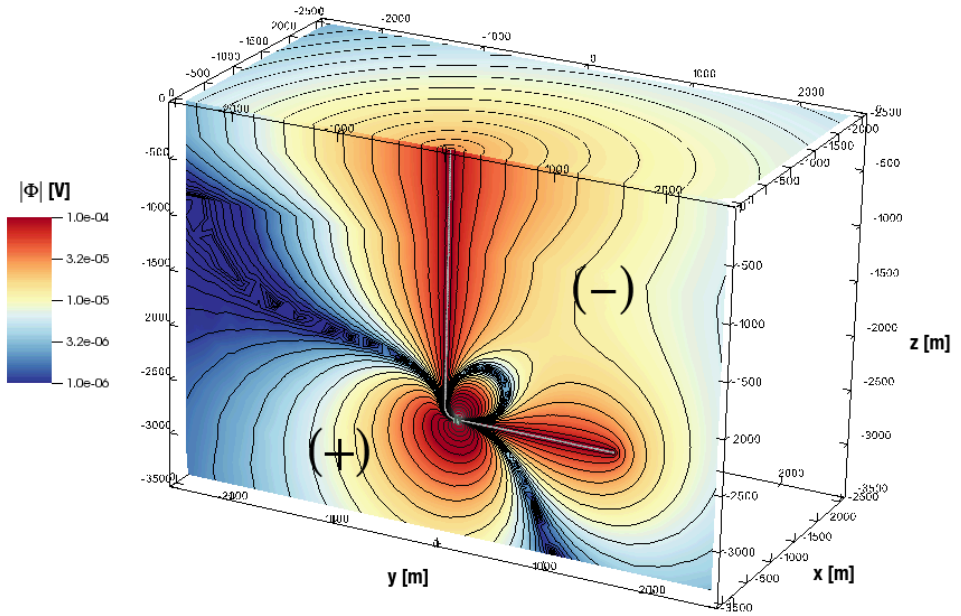

Empirical LQS inversion: invert time-lapse surface data for linear charge density (**l**ambda) on the well casing; point charge **q** at the fracture, and position **s** of the fracture.

LQS inversion: eyeball minimization of the misfit norm

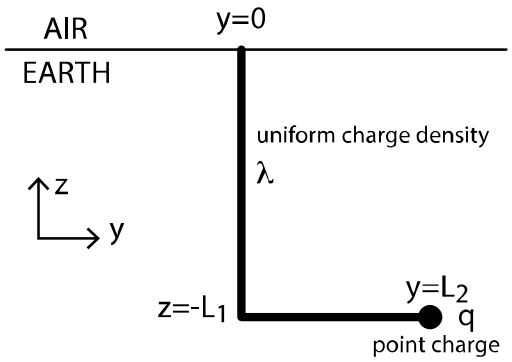

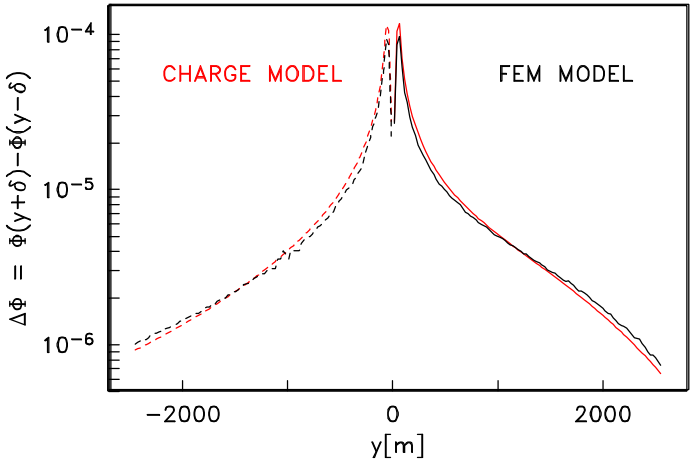

(left) problem setup for LQS inversion of toe-fracture data with known fracture location, s. Inversion is linear in charge magnitudes λ and q.

(right) eyeball-minimized data misfit of time lapse inline potential differences. λ = 5.6E-15 C/m, q = 1.7E-11 C.

LQS Inversion: minimize the L2 norm

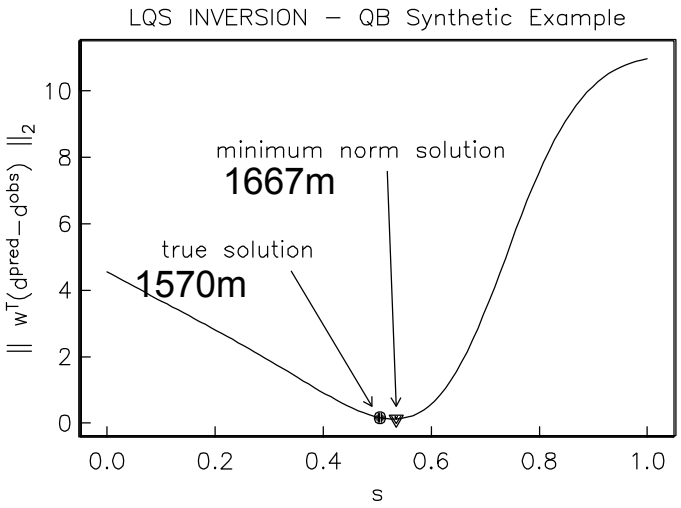

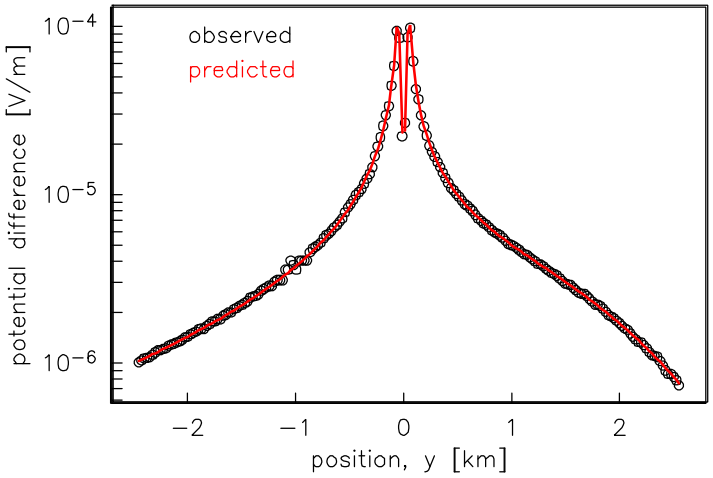

(left) Line search on s for minimum L2 misfit. At each candidate location, s, the linear inverse problem for (λ,q) is solved.

(right) L2-minimized data misfit of time lapse inline potential differences. λ = 5.1E-15 C/m, q = 1.8E-11 C.

LQS inversion: 2D array of 2-component data

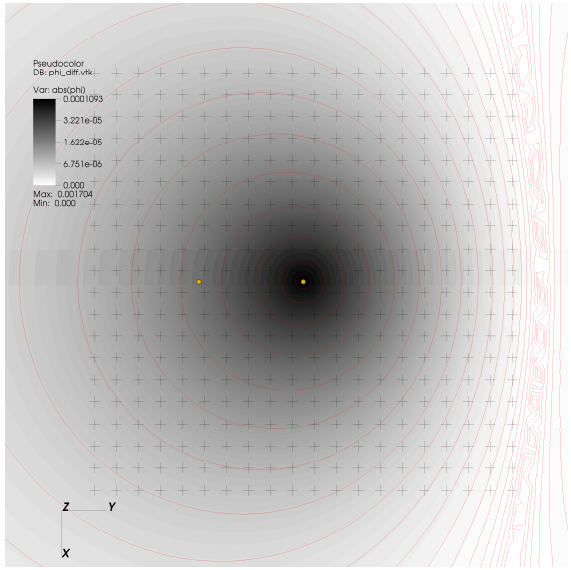

(above) Broaden the array to a *massive* 20x20 grid of 2-component measurements on a 4x4 km area. Time-lapse potentials in grey scale with red contours. Stations indicated by + signs. Well head and ground point indicated by yellow dots.

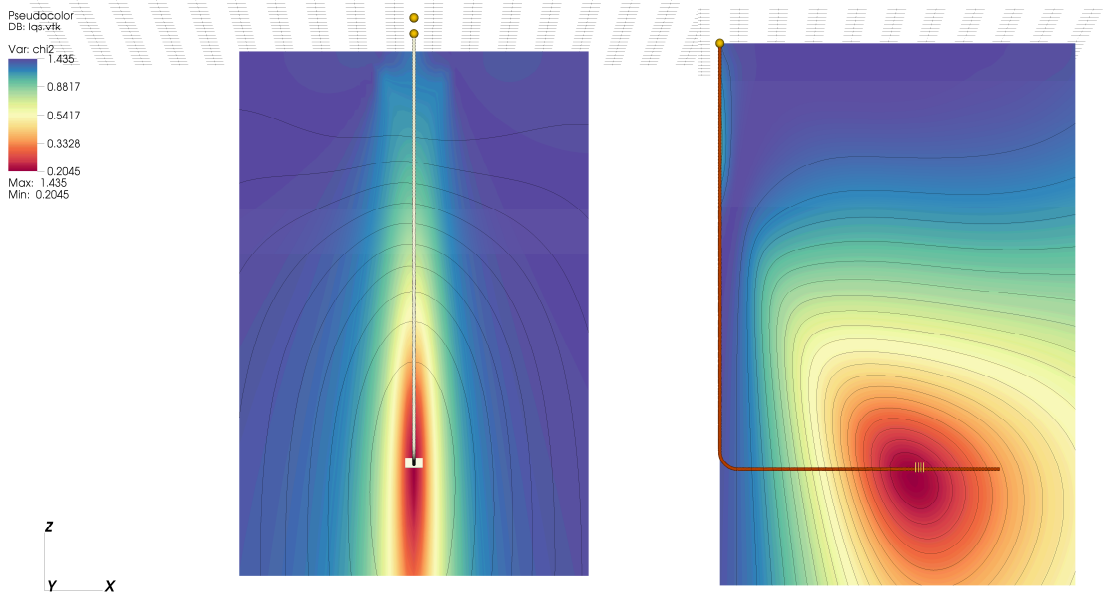

Color scaled L2 norm values of optimal (λ,q) pairs for candidate 's' points in a plane orthogonal to the horizontal section of the well bore and through the fracture set **(left)**, and in a plane containing the entire well bore **(right)**.

LQS Inversion: 3D fracture location

Inversion of synthetic data taken from a *massive* 20x20 grid of 2-component measurements on a 4x4 km area. Time-lapse potentials in grey scale with red contours.

Stations indicated by + signs. Well head and ground point indicated by yellow dots.

Red isosurface surrounding the fractures is taken at χ^2=2, a value where its width is similar to that of the fractures.

$$\chi^2 = \sum_{i=1}^{N} \left(\frac{d_i^{obs} - d_i^{pred}}{d_i^{obs}} \right)^2$$

Note the strong differences in vertical and lateral resolution!

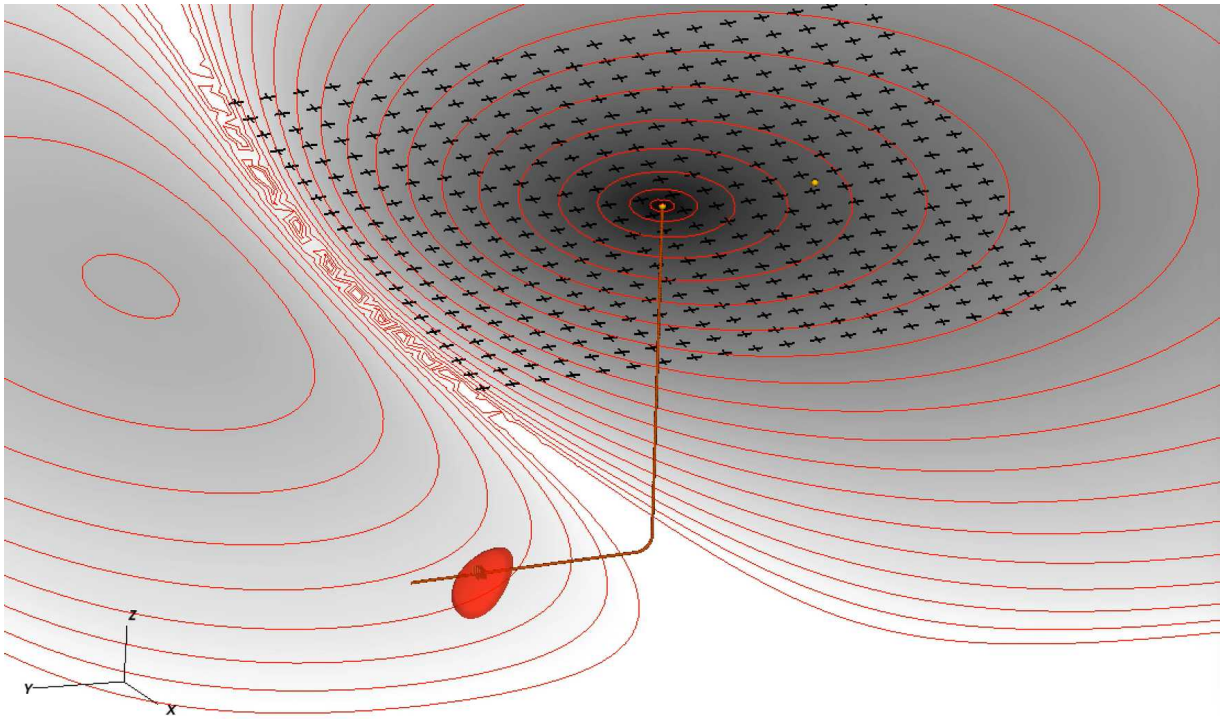

Conclusions

- Assuming electrical continuity of the well casing, DC fracture response is generally independent of source contact point.
- DC response of the fracture set saturates for conductivities greater than 10 S/m in the scenarios tested here. Further investigation is required to quantify such thresholds in other geologic settings.
- Topographic effects introduce signals comparable in magnitude to those of the fractures.
- Time-lapse DC response of the fractures is reasonably approximated by a simple 3-parameter charge model and easily invertible.

Sensitivity Analysis for Oilfield Timelapse Monitoring

Weiss et al. (2016)

Derivation of the Adjoint Sensitivity

Sandia National Laboratories

- Adapted from McGillivray et al. (1994) and modified here for DC.

$$-\nabla \cdot \sigma \nabla \phi = f$$

Primal problem with engineered source, *f*, and conductivity model σ.

$$\sigma(\mathbf{x}) = \sum_{j=1}^{M} \sigma_j \psi_j(\mathbf{x})$$

Representation of the conductivity model in terms of basis functions ψ_j. For example, ψ_j can be functions of compact support, such as a 3D voxel, or have global support in the case of orthogonal polynomials or harmonic functions.

$$\frac{\partial}{\partial \sigma_j}\left(\phi(\mathbf{x}_A) - \phi(\mathbf{x}_B)\right)$$

If we choose ψ_j as a 3D voxel encapsulating the fracture volume, then derivatives of potential differences at two points A and B with respect to the coefficient σ_j quantify the 1st order sensitivity of observations to fracture conductivity.

Derivation of the Adjoint Sensitivity

Sandia National Laboratories

$$-\nabla \cdot \sigma \nabla \tilde{\phi} = \tilde{f}$$ Adjoint problem with adjoint source, $\tilde{f}$, and conductivity model σ.

$$-\nabla \cdot \sigma \nabla \phi = f$$ Primal problem with engineered source, *f*, and conductivity model σ.

Differentiate the primal problem with respect to σ_j, multiply by $\tilde{\phi}$ and rearrange.

$$-\tilde{\phi}\,\nabla \cdot (\psi_j \nabla \phi) - \nabla \cdot \left(\tilde{\phi}\,\sigma\,\nabla \frac{\partial \phi}{\partial \sigma_j} \right) + \sigma \nabla \tilde{\phi} \cdot \nabla \frac{\partial \phi}{\partial \sigma_j} = 0$$

Multiply the adjoint problem by $\frac{\partial \phi}{\partial \sigma_j}$ and rearrange.

$$-\nabla \cdot \left(\frac{\partial \phi}{\partial \sigma_j}\,\sigma\,\nabla \tilde{\phi} \right) + \sigma \nabla \frac{\partial \phi}{\partial \sigma_j} \cdot \nabla \tilde{\phi} = \frac{\partial \phi}{\partial \sigma_j}\,\tilde{f}$$

Derivation of the Adjoint Sensitivity

Sandia National Laboratories

$$-\nabla \cdot \sigma \nabla \tilde{\phi} = \tilde{f}$$ Adjoint problem with adjoint source, $\tilde{f}$, and conductivity model σ.

$$-\nabla \cdot \sigma \nabla \phi = f$$ Primal problem with engineered source, f, and conductivity model σ.

Differentiate the primal problem with respect to σ_j, multiply by $\tilde{\phi}$ and rearrange.

$$-\tilde{\phi}\,\nabla \cdot (\psi_j \nabla \phi) - \nabla \cdot \left(\tilde{\phi}\,\sigma\,\nabla \frac{\partial \phi}{\partial \sigma_j} \right) + \sigma \nabla \tilde{\phi} \cdot \nabla \frac{\partial \phi}{\partial \sigma_j} = 0$$

Multiply the adjoint problem by $\frac{\partial \phi}{\partial \sigma_j}$ and rearrange.

Identical terms

$$-\nabla \cdot \left(\frac{\partial \phi}{\partial \sigma_j}\,\sigma\,\nabla \tilde{\phi} \right) + \sigma \nabla \frac{\partial \phi}{\partial \sigma_j} \cdot \nabla \tilde{\phi} = \frac{\partial \phi}{\partial \sigma_j}\,\tilde{f}$$

Derivation of the Adjoint Sensitivity

Sandia National Laboratories

Difference the previous two equations… (typo in Eq 7 in abstract)

$$\psi_j \nabla\tilde{\phi}\cdot\nabla\phi \;-\; \nabla\cdot\left(\psi_j\tilde{\phi}\nabla\phi \;+\; \tilde{\phi}\sigma\nabla\frac{\partial\phi}{\partial\sigma_j} \;-\; \frac{\partial\phi}{\partial\sigma_j}\sigma\nabla\tilde{\phi}\right) = -\frac{\partial\phi}{\partial\sigma_j}\tilde{f}$$

… and integrate over the domain spatial Ω, on whose bounding surface the potentials vanish (e.g. let Ω extends to infinity). Apply Gauss's theorem to therefore annihilate the surface integrals resulting from the $\nabla\cdot()$ terms in the preceding equation. This leaves...

$$\int_\Omega \psi_j \nabla\tilde{\phi}\cdot\nabla\phi\,\mathrm{d}\Omega = -\int_\Omega \frac{\partial\phi}{\partial\sigma_j}\tilde{f}\,\mathrm{d}\Omega$$

… where we are now free to choose the adjoint source... $\tilde{f} = \delta(\mathbf{x}-\mathbf{x}_A) - \delta(\mathbf{x}-\mathbf{x}_B)$

$$\frac{\partial}{\partial\sigma_j}\left(\phi(\mathbf{x}_A)-\phi(\mathbf{x}_B)\right) = \int_\Omega \psi_j\nabla\tilde{\phi}\cdot\nabla\phi\,\mathrm{d}\Omega$$

... and arrive at our desired expression for the adjoint sensitivity of potential differences measured at two points A and B.

Derivation of the Adjoint Sensitivity

Sandia National Laboratories

Difference the previous two equations… (typo in Eq 7 in abstract)

$$\psi_j \nabla\tilde{\phi}\cdot\nabla\phi \;-\; \nabla\cdot\left(\psi_j\tilde{\phi}\nabla\phi \;+\; \tilde{\phi}\sigma\nabla\frac{\partial\phi}{\partial\sigma_j} \;-\; \frac{\partial\phi}{\partial\sigma_j}\sigma\nabla\tilde{\phi}\right) = -\frac{\partial\phi}{\partial\sigma_j}\tilde{f}$$

… and integrate over the domain spatial Ω, on whose bounding surface the potentials vanish (e.g. let Ω extends to infinity). Apply Gauss's theorem to therefore anihhilate the surface integrals resulting from the $\nabla\cdot()$ terms in the preceding equation. This leaves...

$$\int_\Omega \psi_j \nabla\tilde{\phi}\cdot\nabla\phi \,\mathrm{d}\Omega = -\int_\Omega \frac{\partial\phi}{\partial\sigma_j}\tilde{f}\,\mathrm{d}\Omega$$

… where we are now free to choose the adjoint source... $\tilde{f} = \delta(\mathbf{x}-\mathbf{x}_A) - \delta(\mathbf{x}-\mathbf{x}_B)$

sensitivity kernel

$$\frac{\partial}{\partial\sigma_j}\left(\phi(\mathbf{x}_A)-\phi(\mathbf{x}_B)\right) = \int_\Omega \psi_j \nabla\tilde{\phi}\cdot\nabla\phi\,\mathrm{d}\Omega$$

... and arrive at our desired expression for the adjoint sensitivity of potential differences measured at two points A and B.

Subsurface DC potential distribution

Sandia National Laboratories

Primal Potentials

Adjoint Potentials

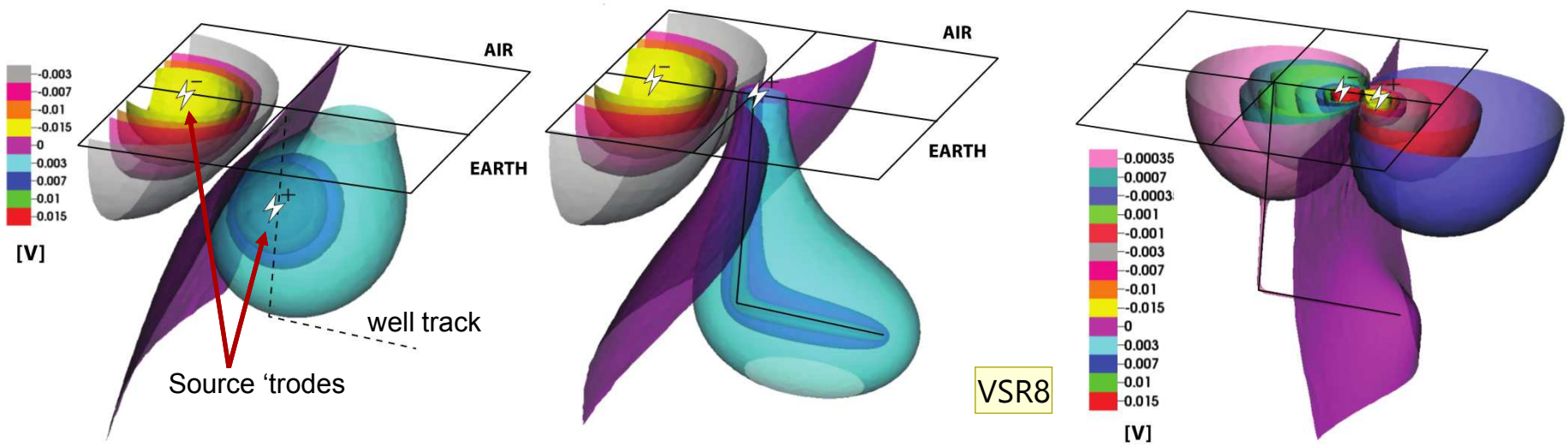

ignoring the borehole casing

considering the borehole casing

”inline” dipole configuration

Note the strong coupling between the source trodes and the borehole casing, even when not in direct electrical contact.

Slide 57

VSR8 I take it this is an industry term
Vigil, Steven R, 10/7/2016

2D slice of sensitivity kernel: near inline offset

Source electrodes: symbols

Measurement electrodes: A and B

Warm colors indicate regions where a conductivity perturbation gives rise to a large perturbation in the A-B measurement. Regions of cool colors result in small, and in some cases zero, effect on measurements.

Note the strong sensitivity to the near-surface, suggesting the need for a stable weather window if taking time-lapse data. Also notice the sign change along the borehole path.

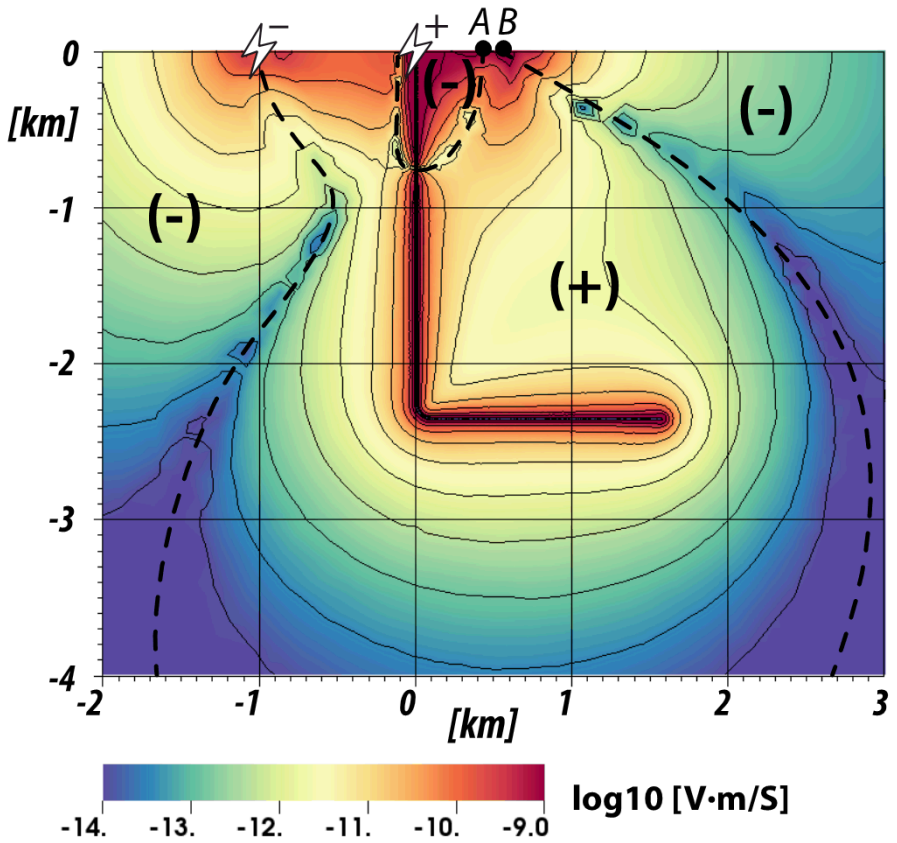

2D slice of sensitivity kernel: intermediate offset

Source electrodes: symbols

Measurement electrodes: A and B

Warm colors indicate regions where a conductivity perturbation gives rise to a large perturbation in the A-B measurement. Regions of cool colors result in small, and in some cases zero, effect on measurements.

Note the strong sensitivity to the near-surface, suggesting the need for a stable weather window if taking time-lapse data. Also notice the sign change along the borehole path.

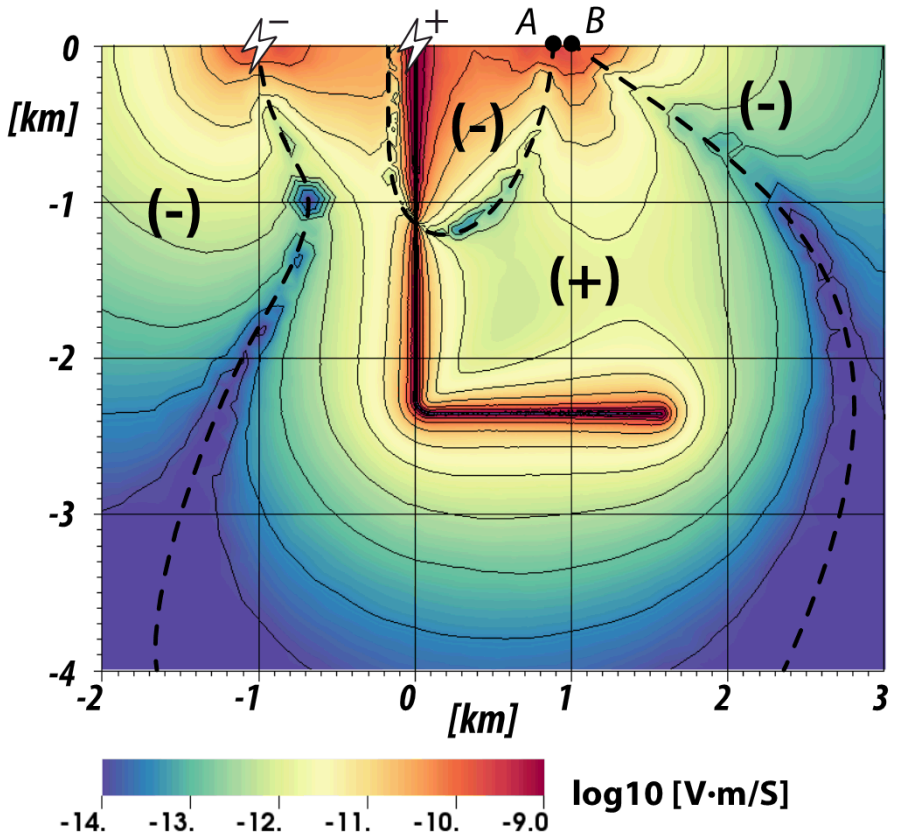

2D slice of sensitivity kernel: long inline offset

Source electrodes: symbols

Measurement electrodes: A and B

Warm colors indicate regions where a conductivity perturbation gives rise to a large perturbation in the A-B measurement. Regions of cool colors result in small, and in some cases zero, effect on measurements.

Note the strong sensitivity to the near-surface, suggesting the need for a stable weather window if taking time-lapse data. Also notice the sign change along the borehole path.

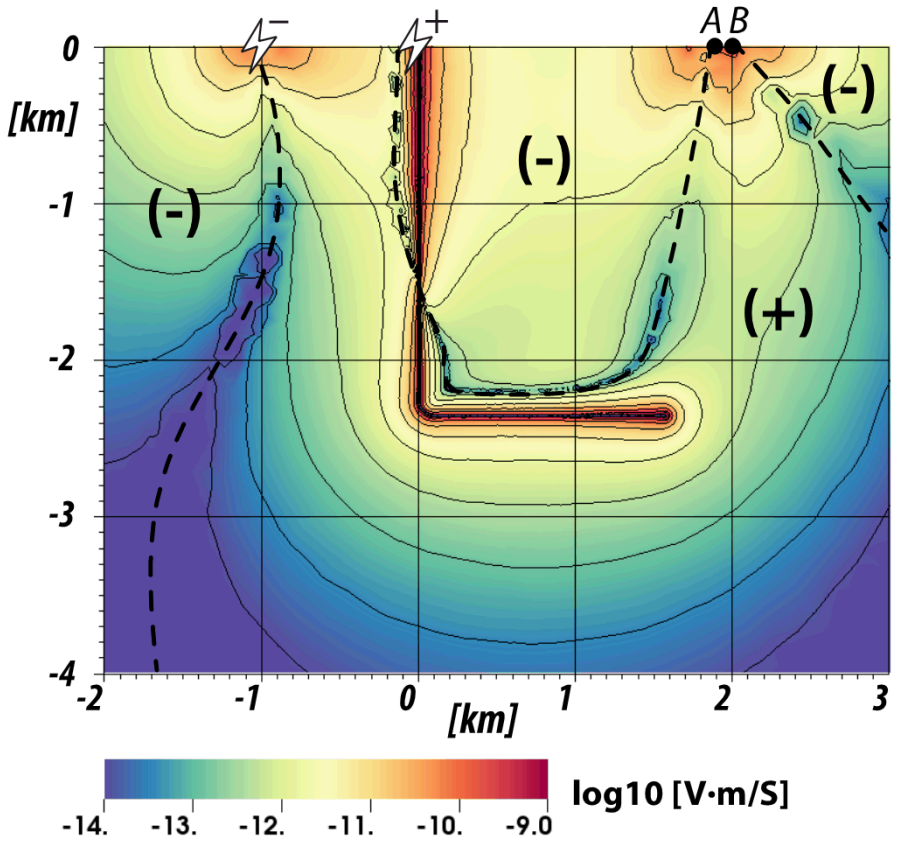

The BIG breakthrough: Hierarchical Finite Elements

Weiss (Geophysics, 2017)

Hanging the material properties on the tets, faces and edges of the unstructured tetrahedral mesh allows for thin conductors to be economically represented by facets and edges, rather than 100s of millions of tiny tets.

$$\boldsymbol{\sigma}(\boldsymbol{x}) = \sum_{e=1}^{N_V} \sigma_e \boldsymbol{\psi}_e^V(\boldsymbol{x}) + \sum_{e=1}^{N_F} s_e \boldsymbol{\psi}_e^F(\boldsymbol{x}) + \sum_{e=1}^{N_E} t_e \boldsymbol{\psi}_e^E(\boldsymbol{x})$$

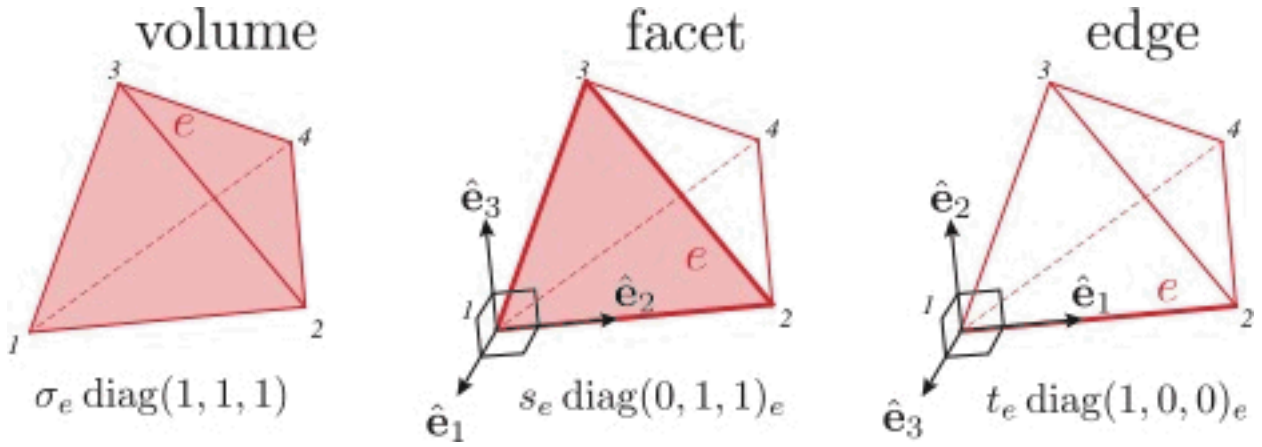

This hierarchy of material distributions is made possible by using rank-2 tensor basis functions – an extension of the early work in 2D anisotropy by Weiss and Newman (Geophysics, 2002, 2003)

$$\boldsymbol{\sigma}(\boldsymbol{x}) = \sum_{e=1}^{N_V} \sigma_e \boldsymbol{\psi}_e^V(\boldsymbol{x}) + \sum_{e=1}^{N_F} s_e \boldsymbol{\psi}_e^F(\boldsymbol{x}) + \sum_{e=1}^{N_E} t_e \boldsymbol{\psi}_e^E(\boldsymbol{x})$$

$$\boldsymbol{\psi}_e^V(\boldsymbol{x}) = \mathrm{diag}(1,1,1) \begin{cases} 1 & \text{if } \boldsymbol{x} \in \text{volume } e \\ 0 & \text{otherwise} \end{cases}$$

$$\boldsymbol{\psi}_e^E(\boldsymbol{x}) = \mathrm{diag}(1,0,0)_e \begin{cases} 1 & \text{if } \boldsymbol{x} \in \text{edge } e \\ 0 & \text{otherwise} \end{cases}$$

$$\boldsymbol{\psi}_e^F(\boldsymbol{x}) = \mathrm{diag}(0,1,1)_e \begin{cases} 1 & \text{if } \boldsymbol{x} \in \text{facet } e \\ 0 & \text{otherwise} \end{cases}$$

The tensor representation keeps the material properties local to the edges and facets in the Finite Element weak formulation / bilinear form.

Benchmarking and internal consistency checks show that for thin conductors, the facet/edge representation achieves acceptable accuracy over a range of geometries and material properties.

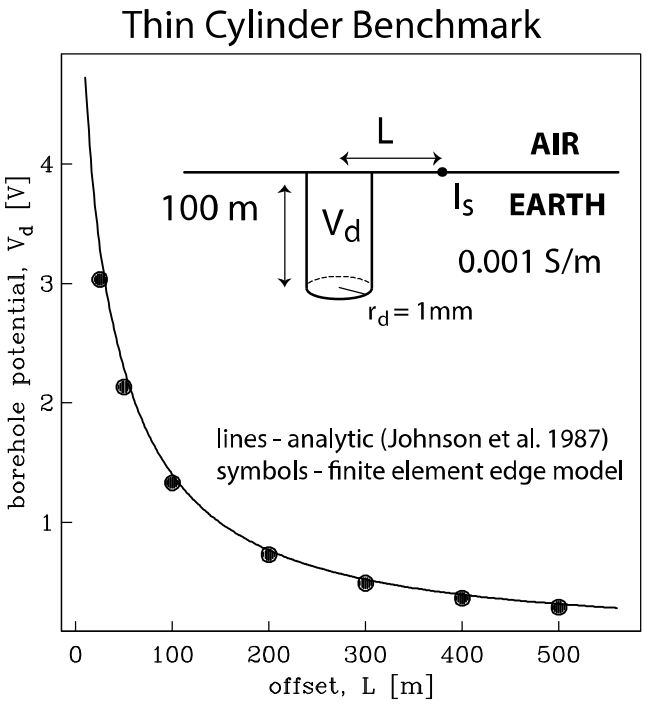

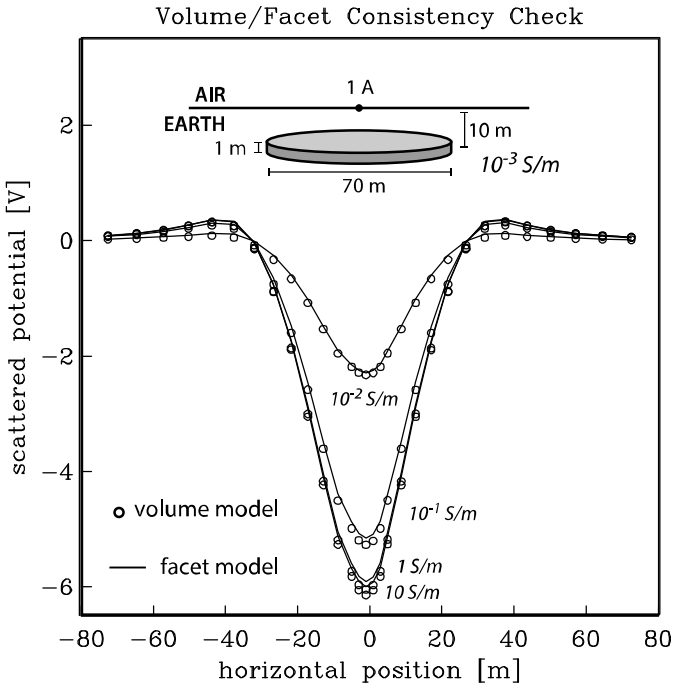

Visual inspection of thin disk results for facet elements (left) and many small tetrahedral elements (right).

Shown is a cross section of electric potential through the disk and surrounding geology for a weak conductor (top) and strong conductor (bottow). Background conductivity is 0.001 S/m.

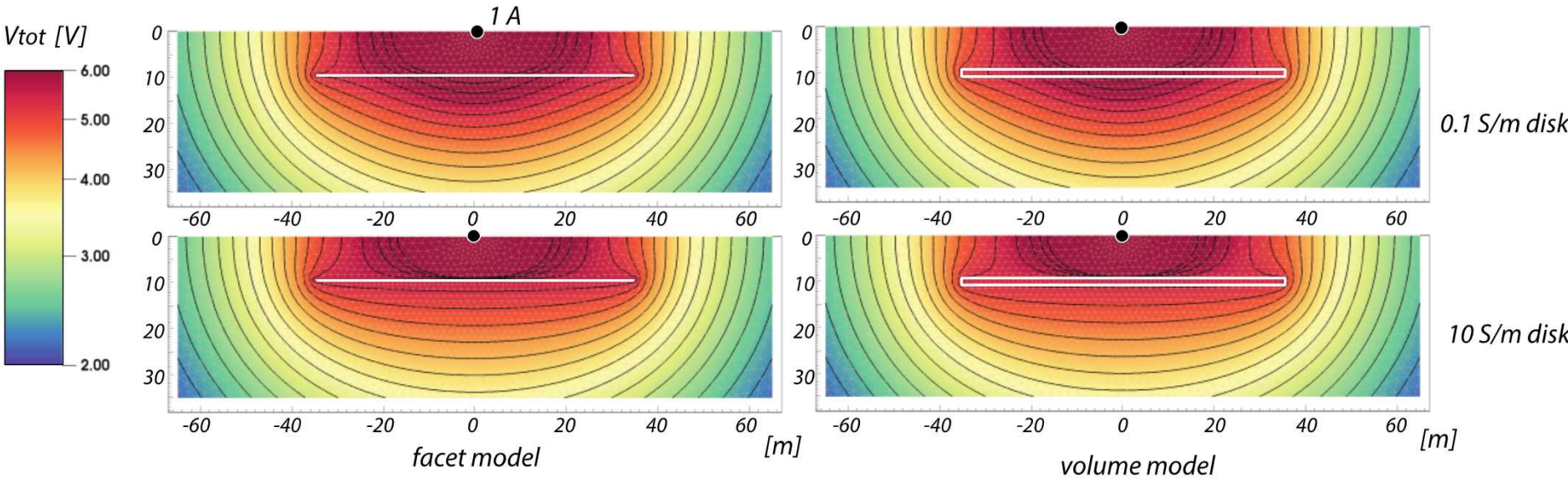

Because of the continuity condition, thin resistors require a little more intervention. Specifically, we require that the infinitely thin resistor be multi-valued on the disk surface, with either side of the surface subject to a Neumann boundary condition. This is called a “tear” in the FE literature.

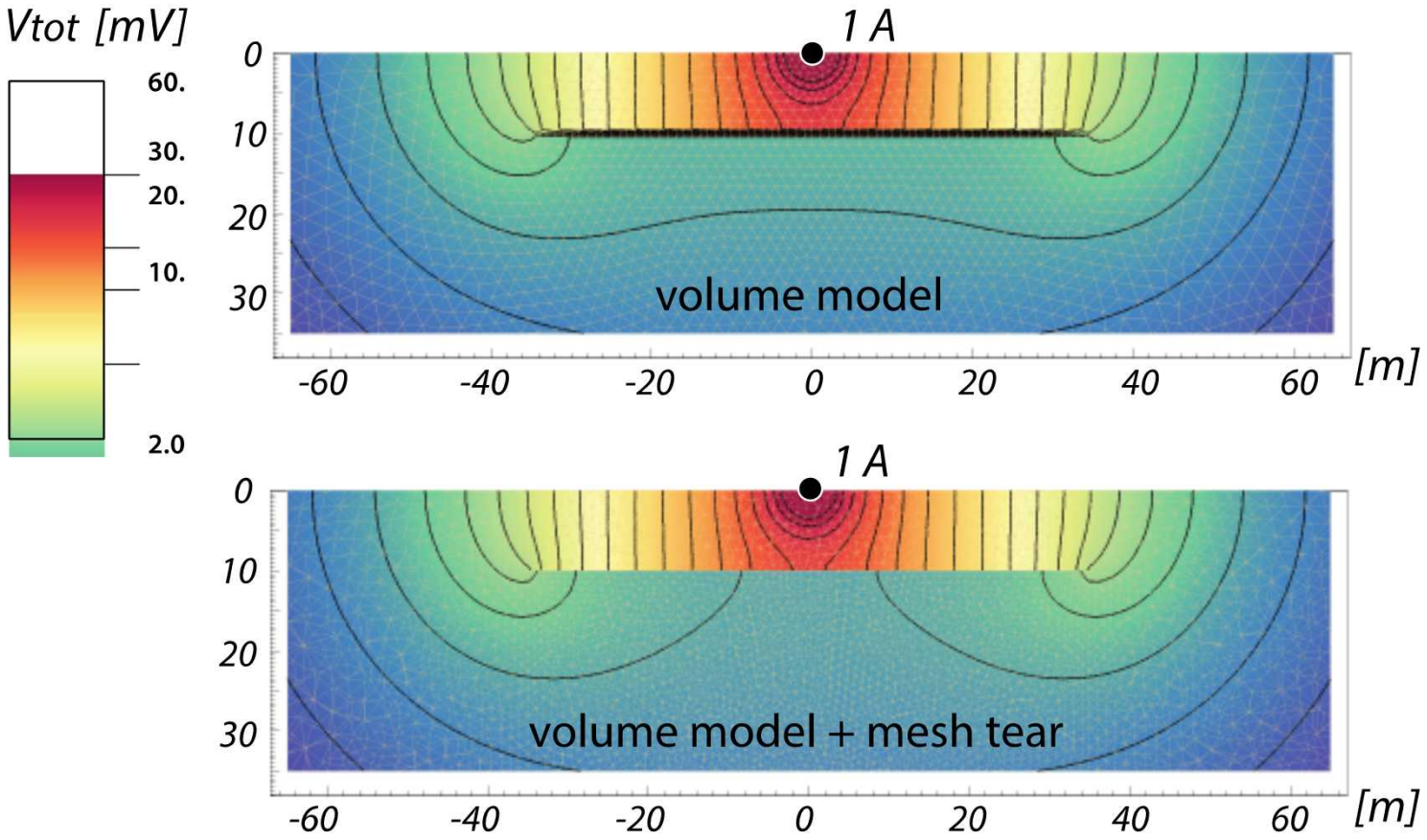

The ”tear” representing the thin resistor is doubly discretized, with one set of nodes corresponding to tets on one side of the tear, and second set for tets on the other side. Still, the surface is infinitely thin and we avoid extreme discretization of a thin, but finite thinckness “slab” filled with millions of tiny tets.

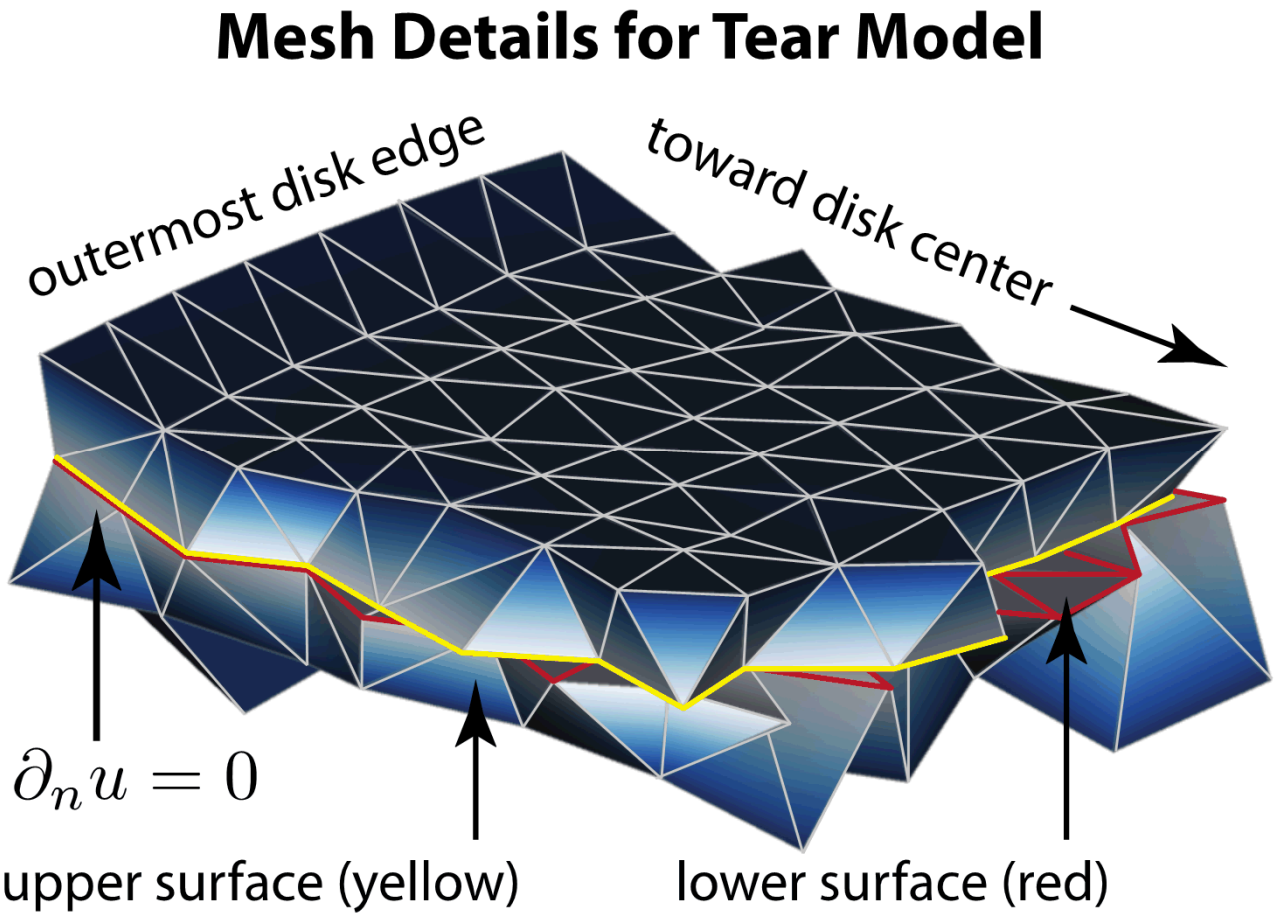

With the mathematical framework in place along with favorable benchmarking results, we're now emboldened to investigate oilfield problems.

EXAMPLE PROBLEM: an idealized multi-lateral (edge elements for casing)

What is the effect of casing conductivity on the casing potential?

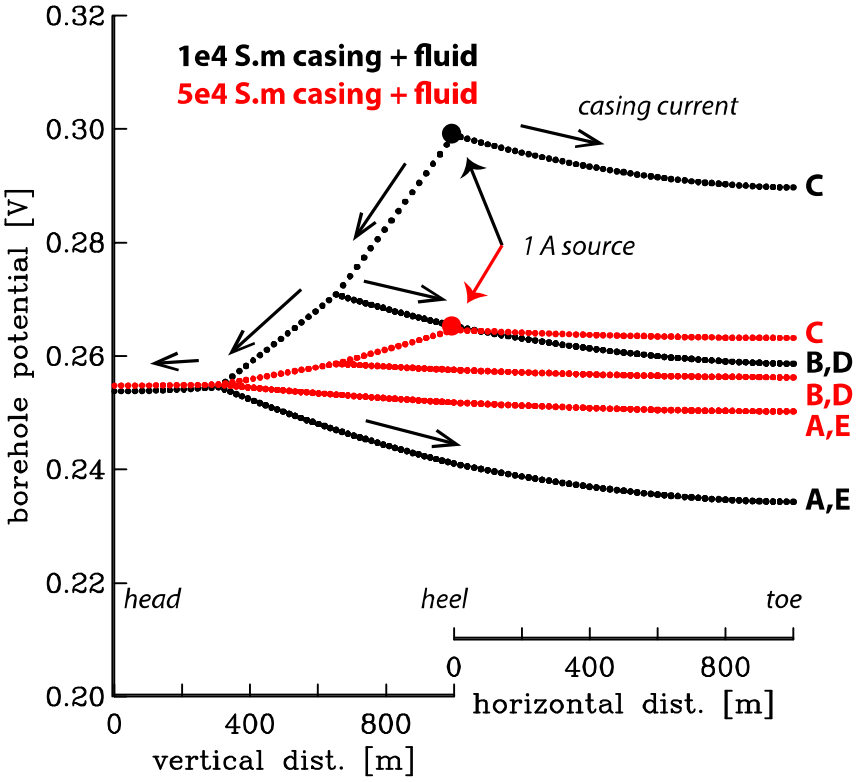

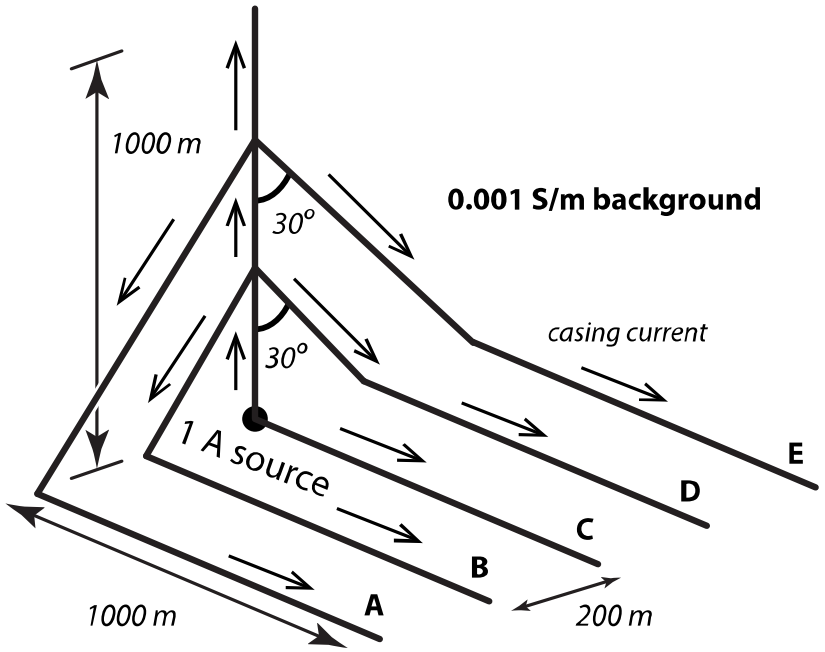

3D rendering of the multi-lateral system

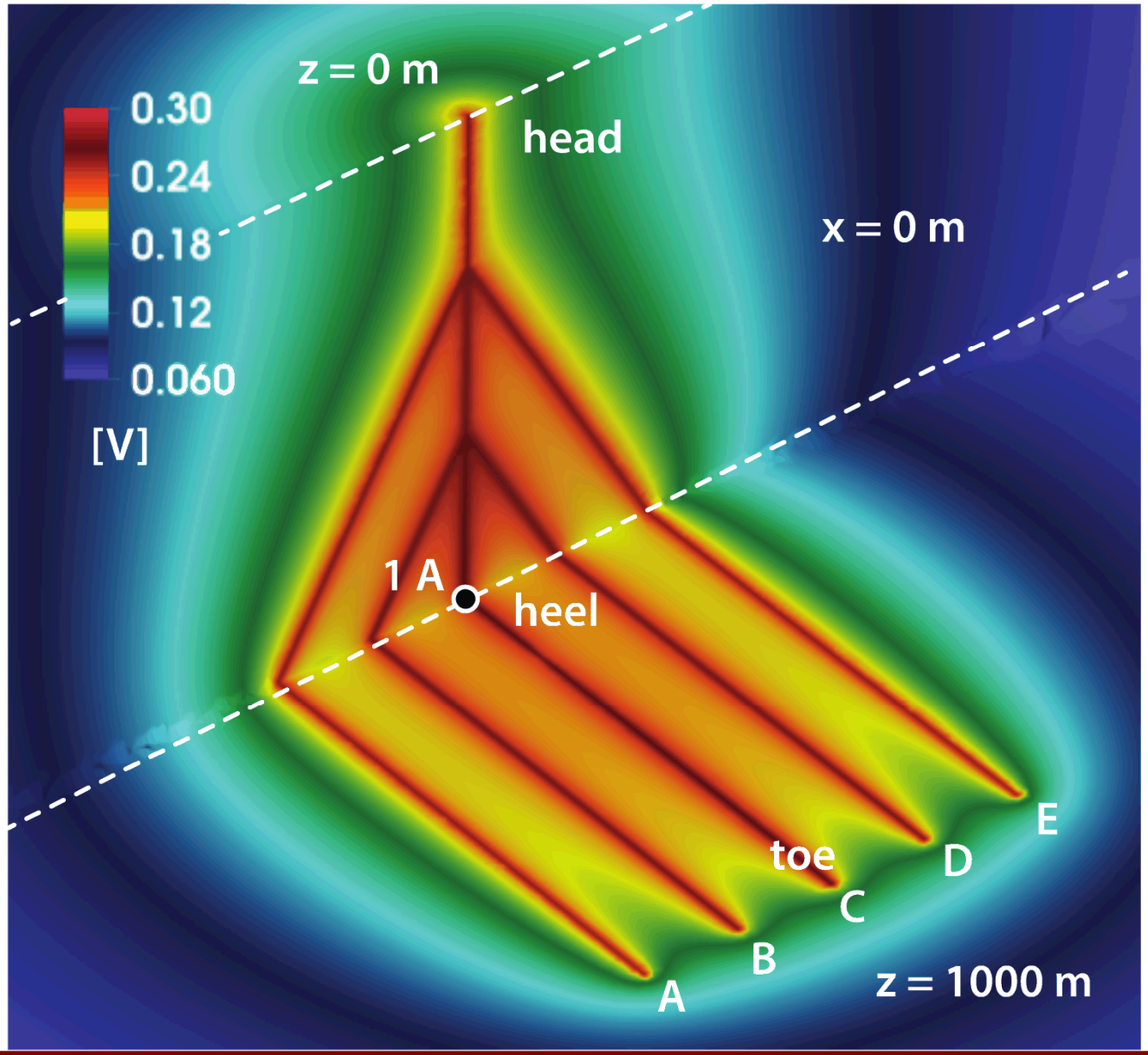

With the mathematical framework in place along with favorable benchmarking results, we're now emboldened to investigate oilfield problems.

EXAMPLE PROBLEM: an idealized multi-lateral, now with a fracture.

What effect does a conductive fracture have on the casing system?

casing: edge elements, fracture: facet elements

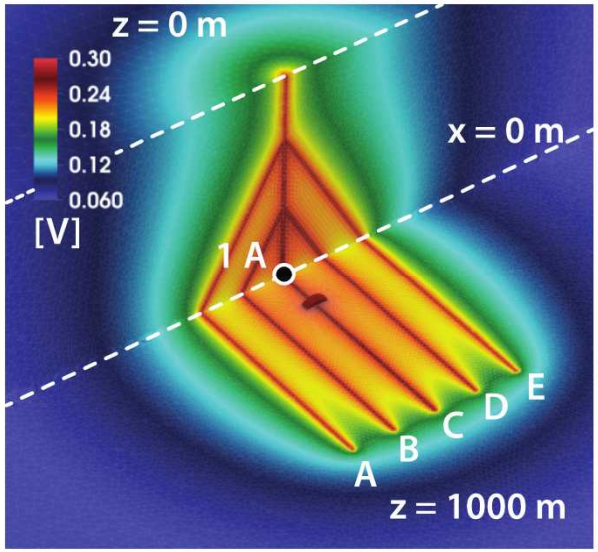

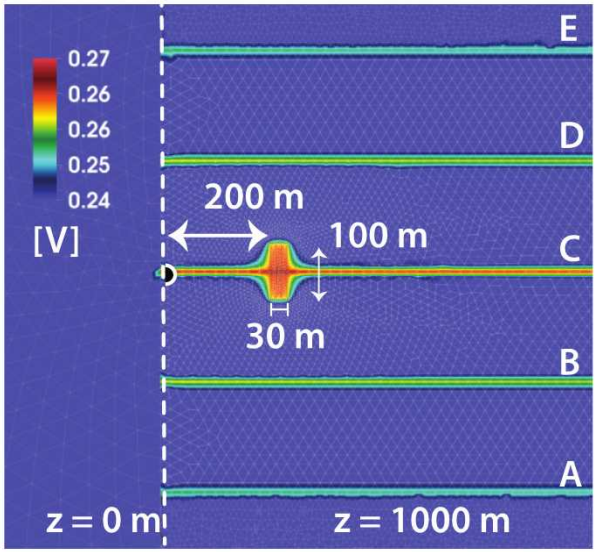

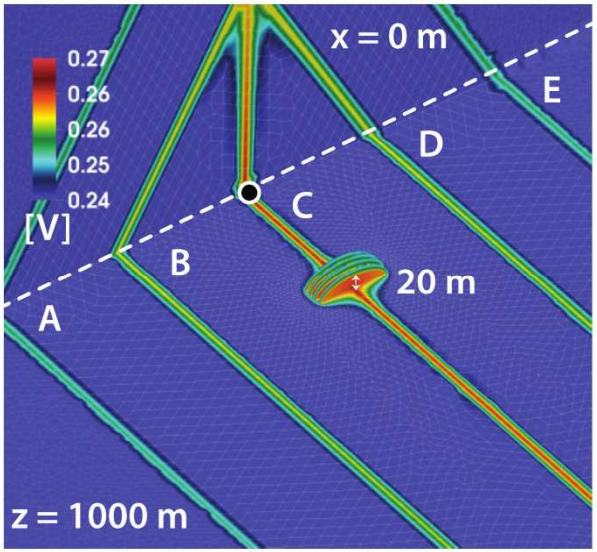

4D time-lapse response of casing response with conductive fractures introduced into the system

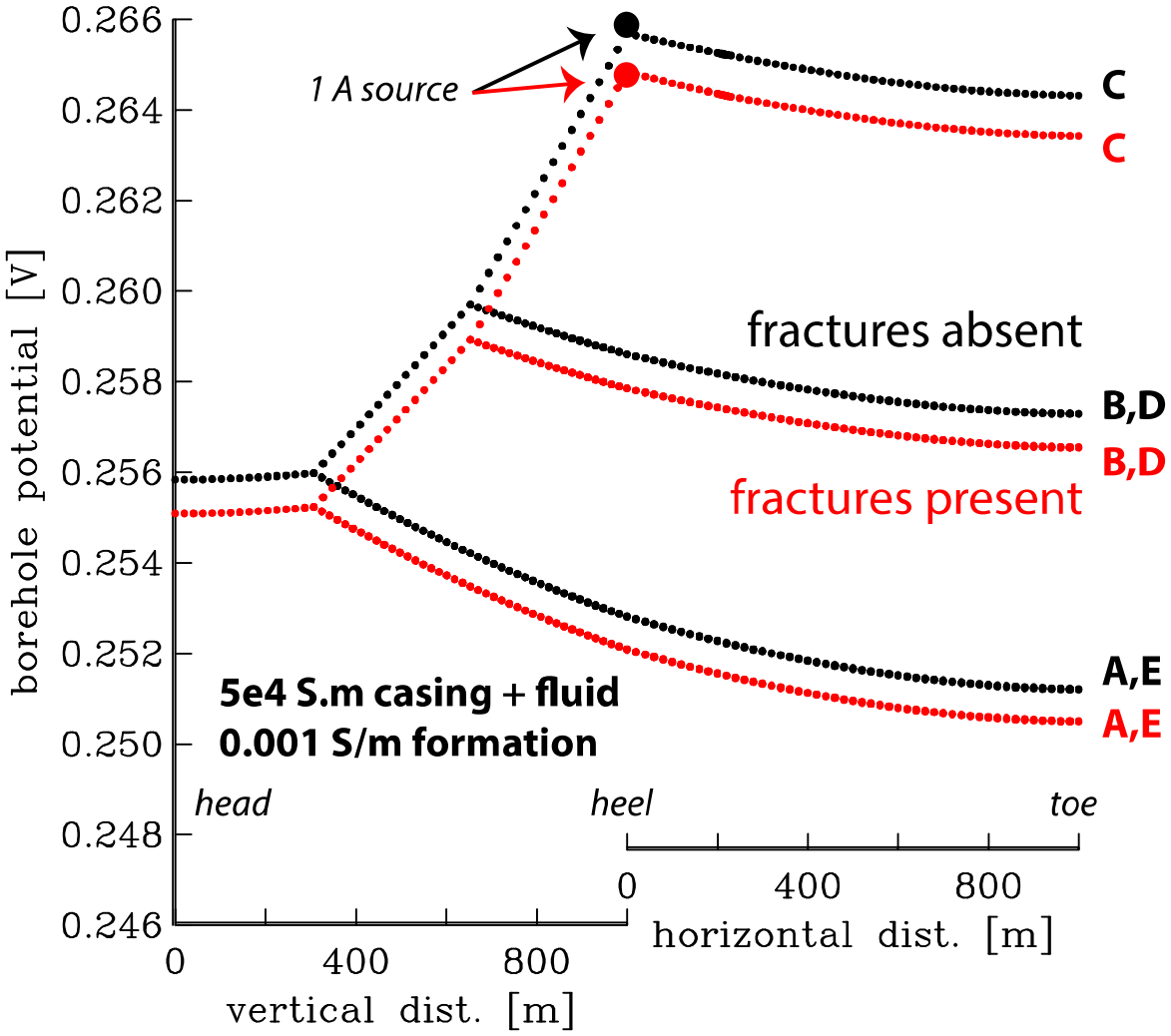

4D time-lapse differences of casing potential due to introduced fractures.

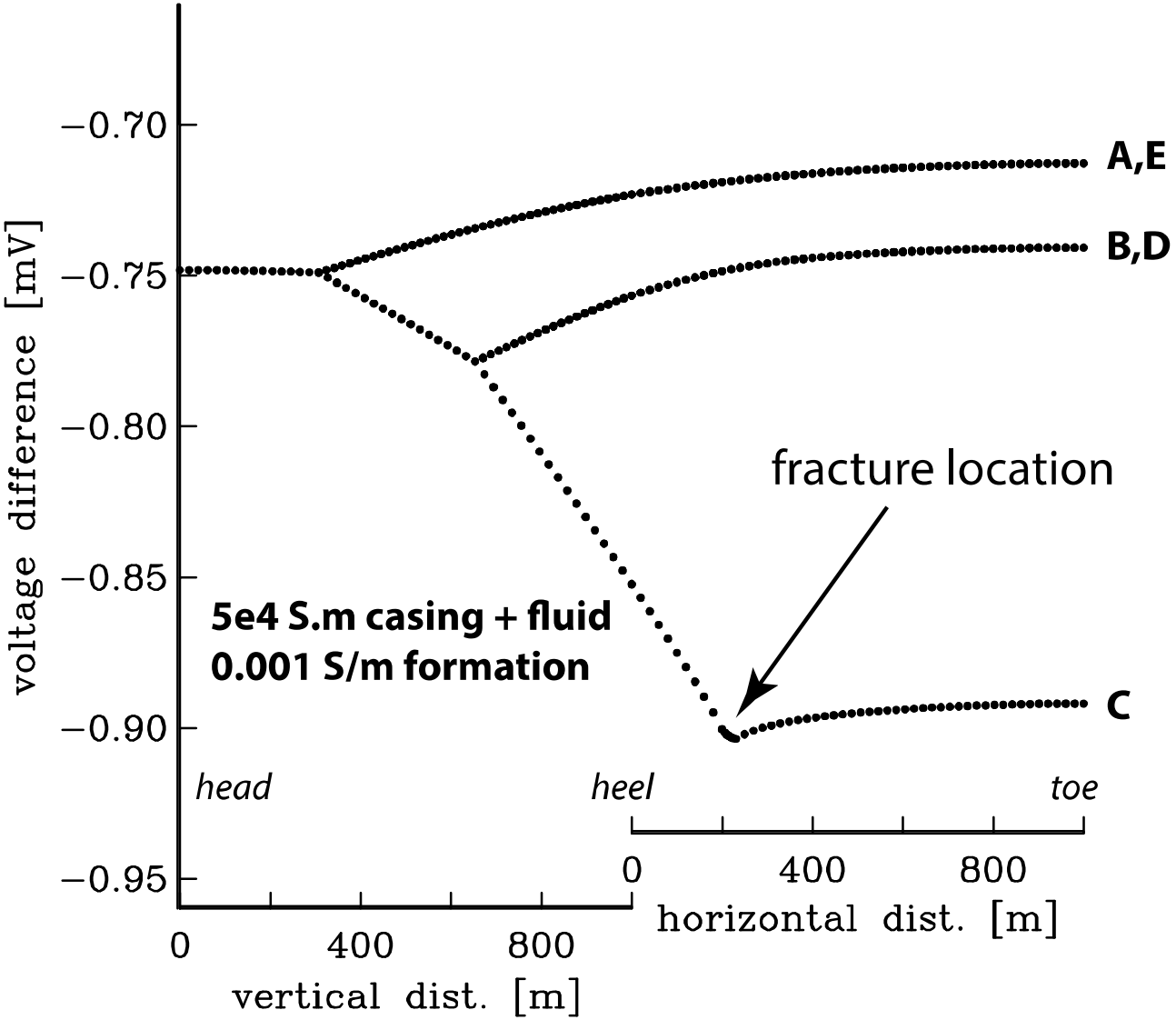

What happens when some of the horizontals aren't in direct electrical contact? I.e. passive coupling between all the steel in the ground.

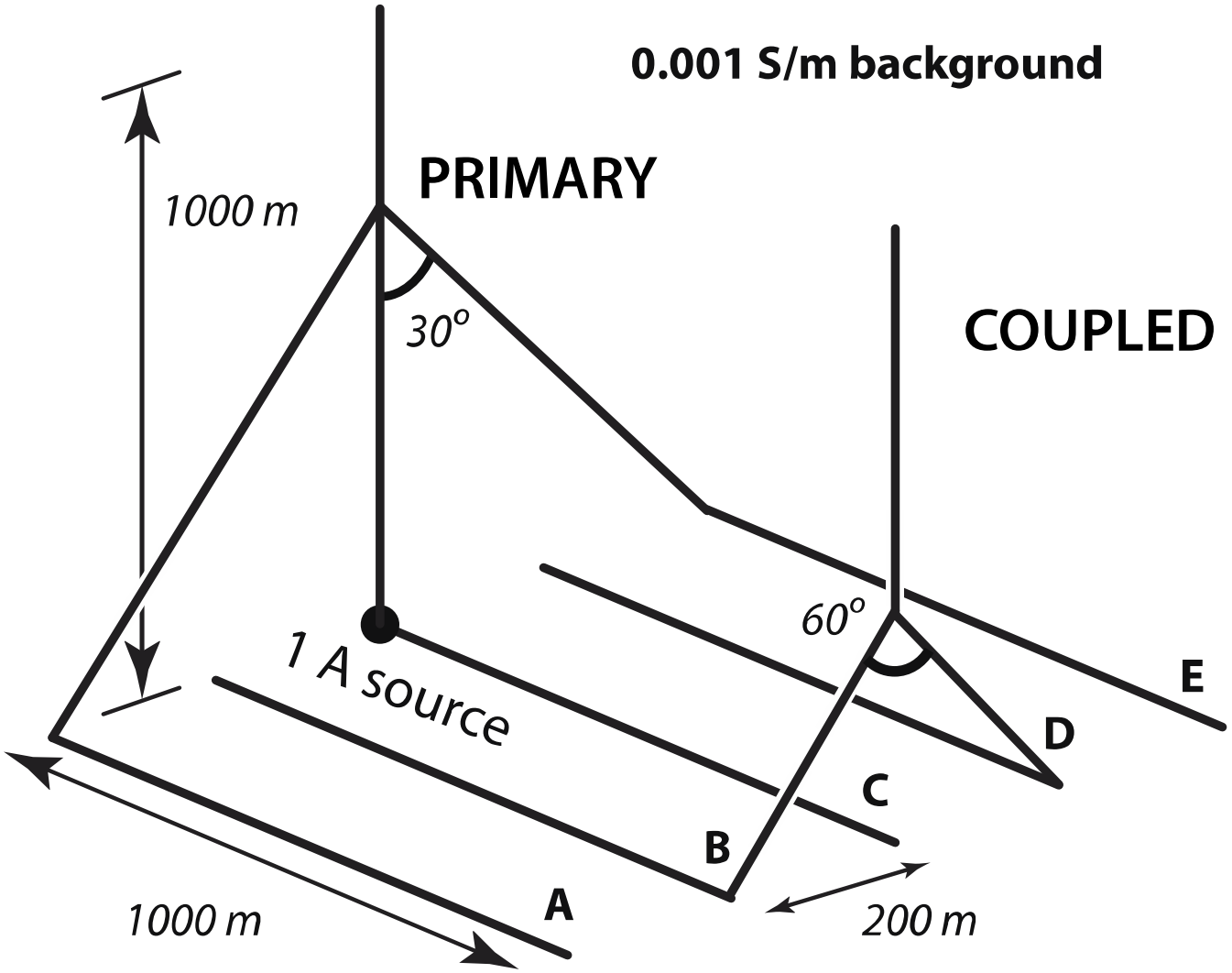

What happens when some of the horizontals aren't in direct electrical contact? I.e. passive coupling between all the steel in the ground.

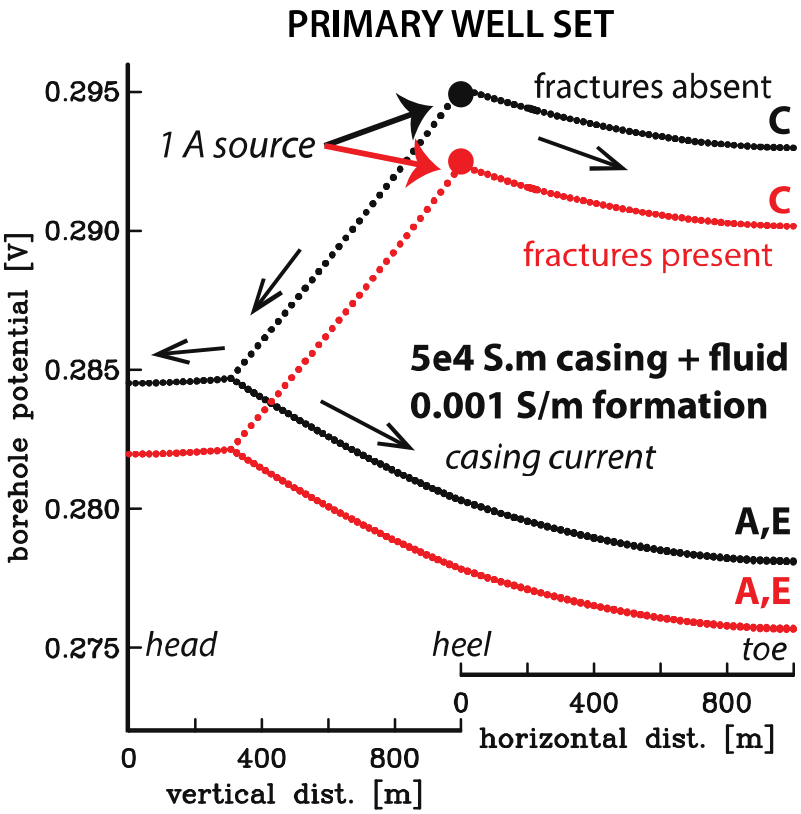

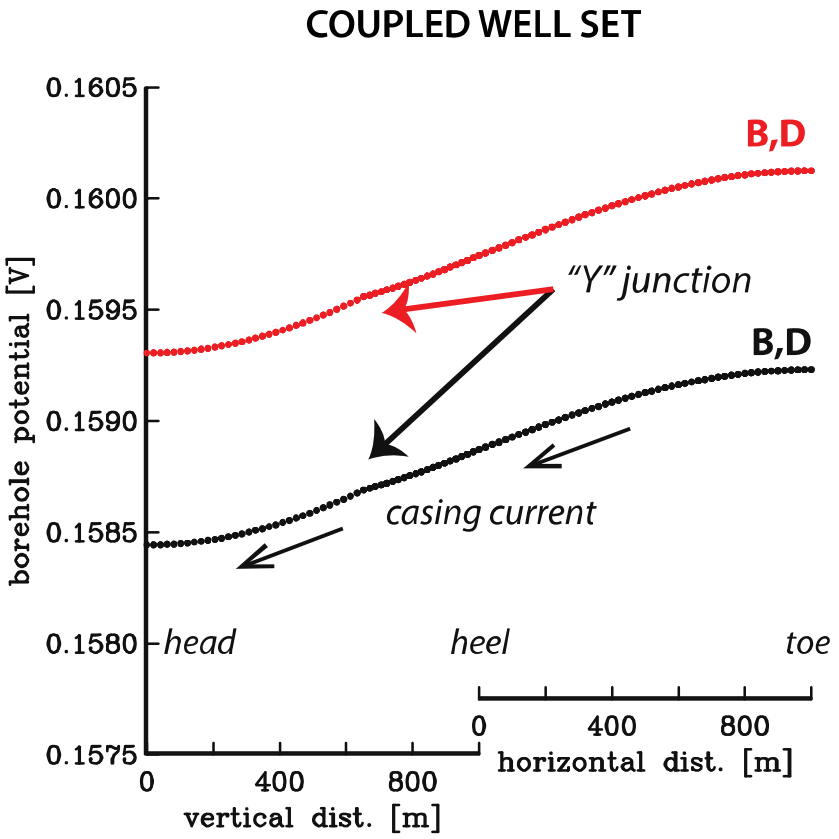

4D differences of casing potential for passively coupled casings.

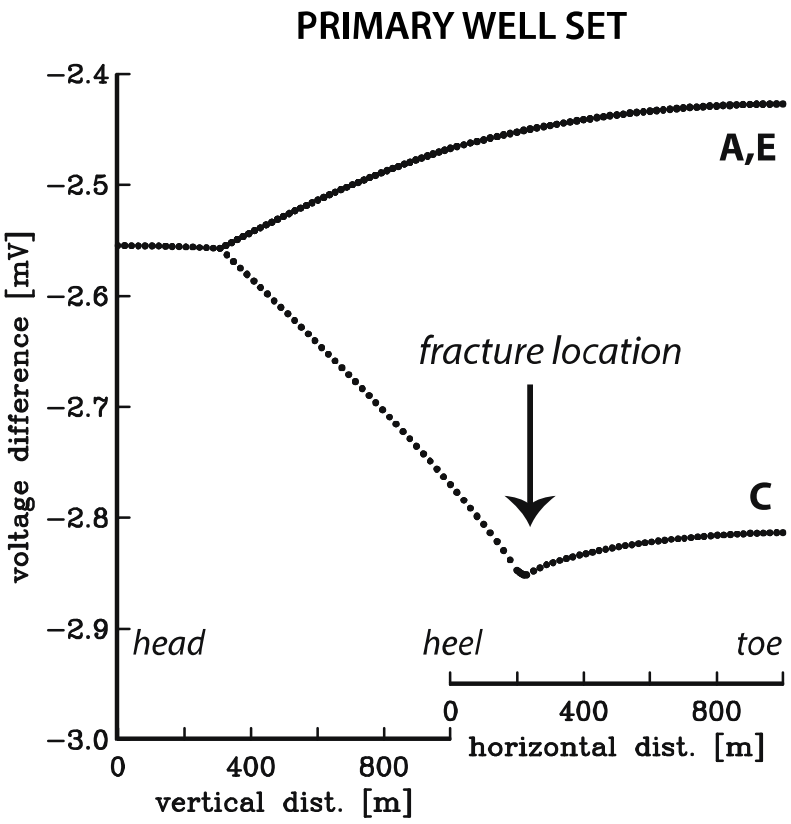

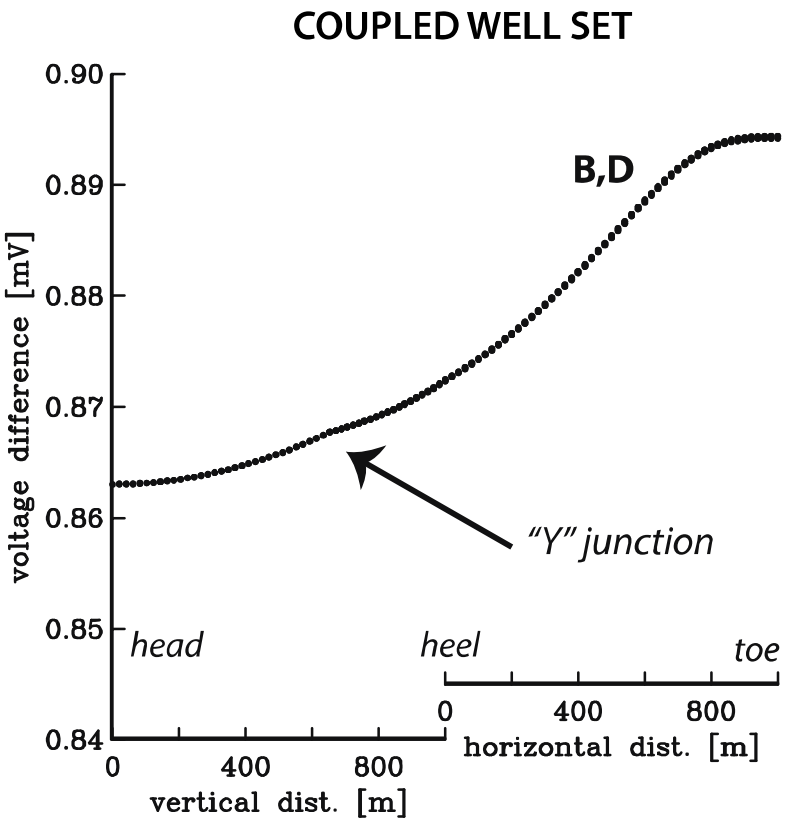

What does the time-lapse surface electric field look like for different casing configurations? Better get all the steel in your model!

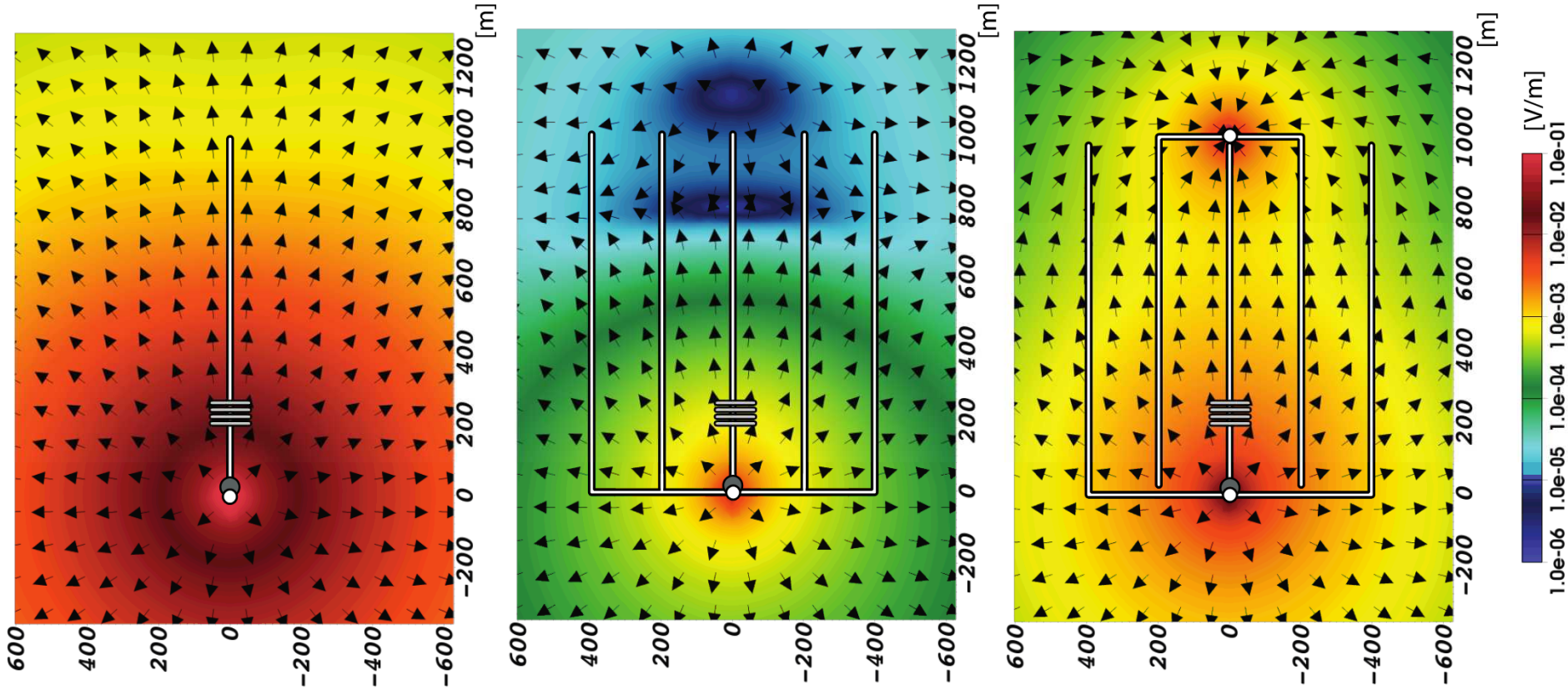

Numerical Tidbits.

Adding steel to the model is known to increase the runtime. But still… the runtimes are on the order of a few minutes, rather than hours.

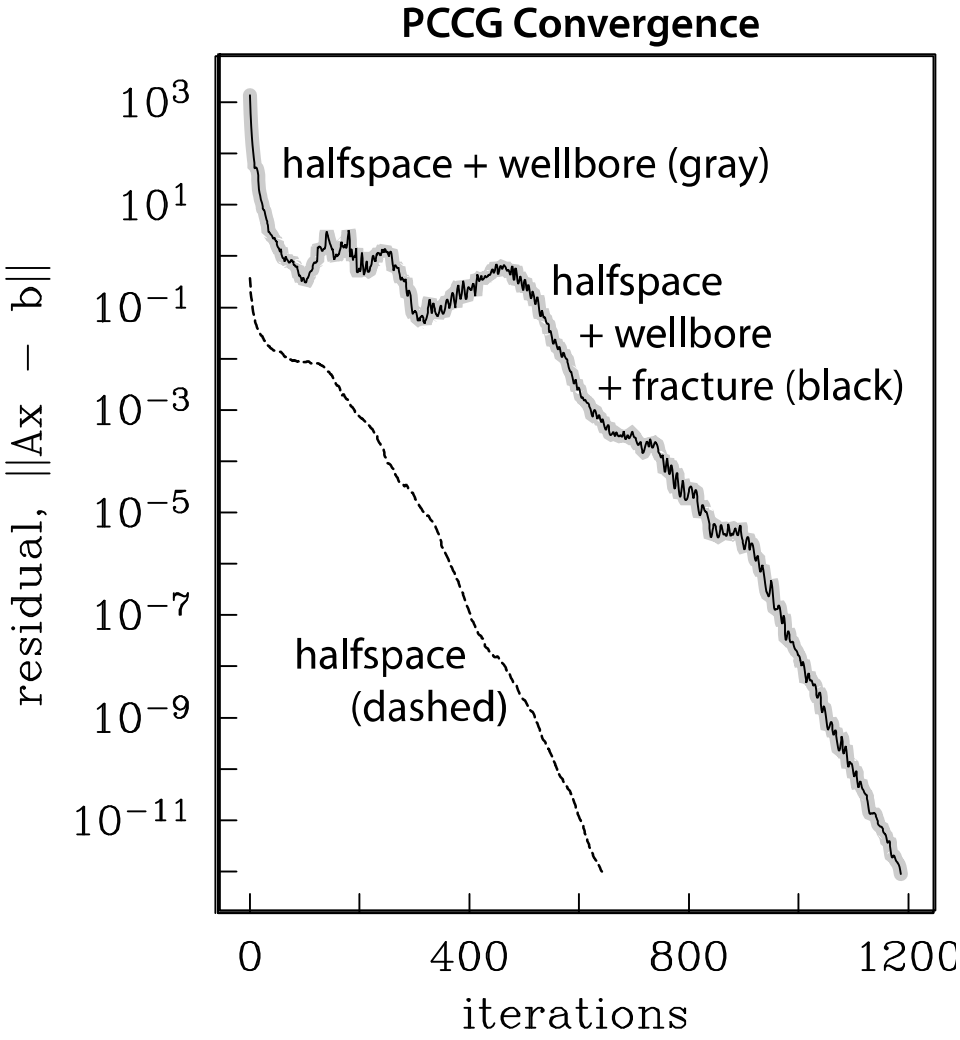

”Facet” model representation allows for efficient perf design studies

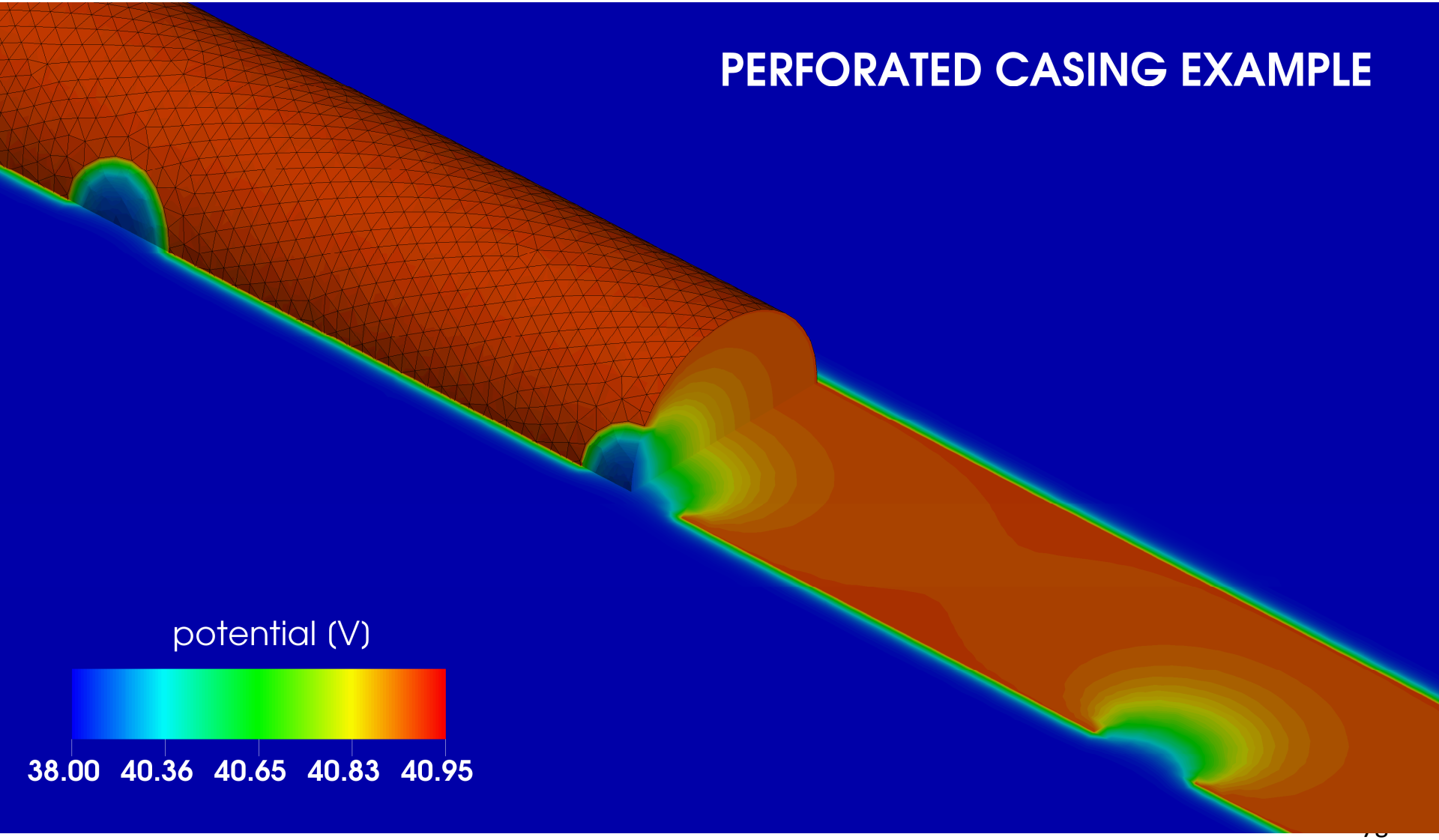

Applying this to Actual Oilfield Settings

Weiss andn Wilson (SEG, 2017)

Kern River Formation Site

0.7 km^2 area + 122 wells + ~2 km surface pipes

Sandia National Laboratories

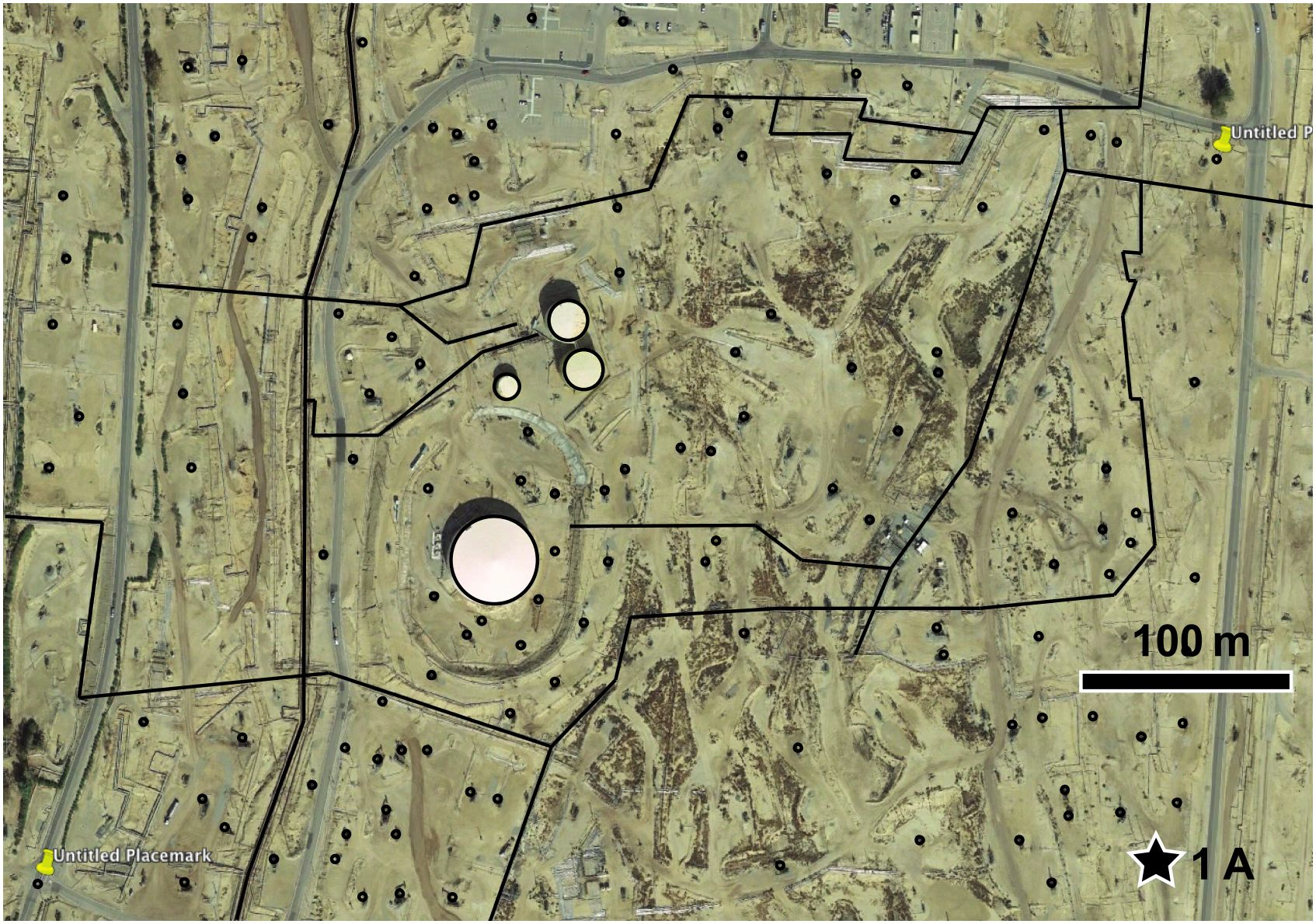

Assuming 300 m well depth gives ~30 km of casing. Add to that 2 km of surface pipeline and the 4 tanks.

Total simulation time ~ 30 min, un-optimized.

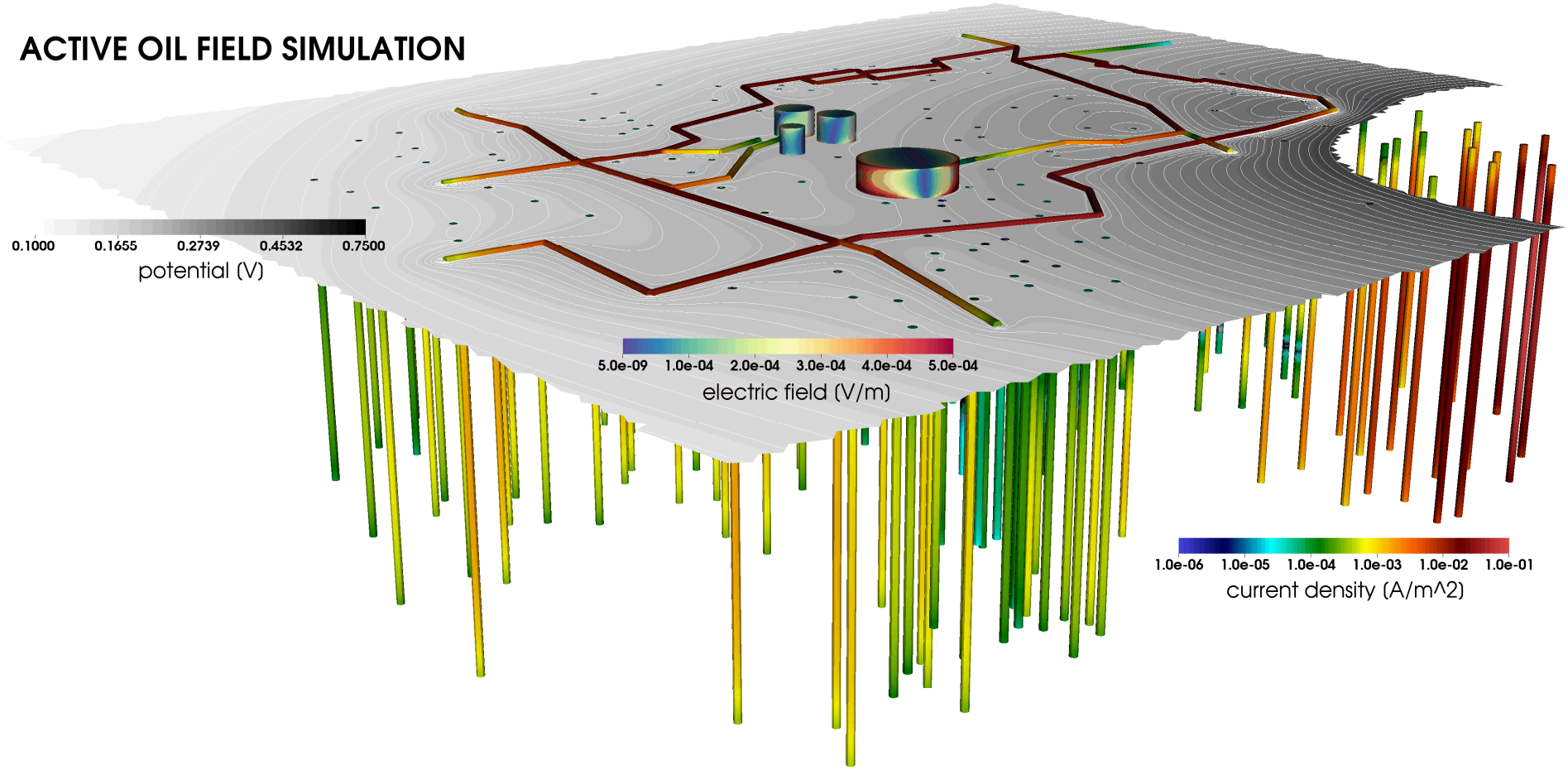

Kern River Formation Site

Electric current density (colors + arrows) for full casing/pipeline coupling (left) and pipeline alone (right).

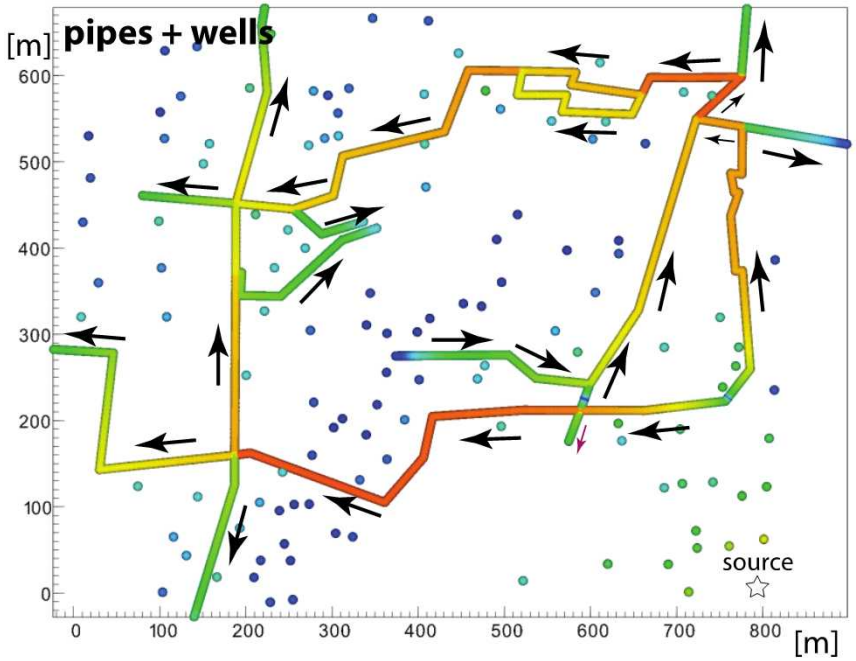

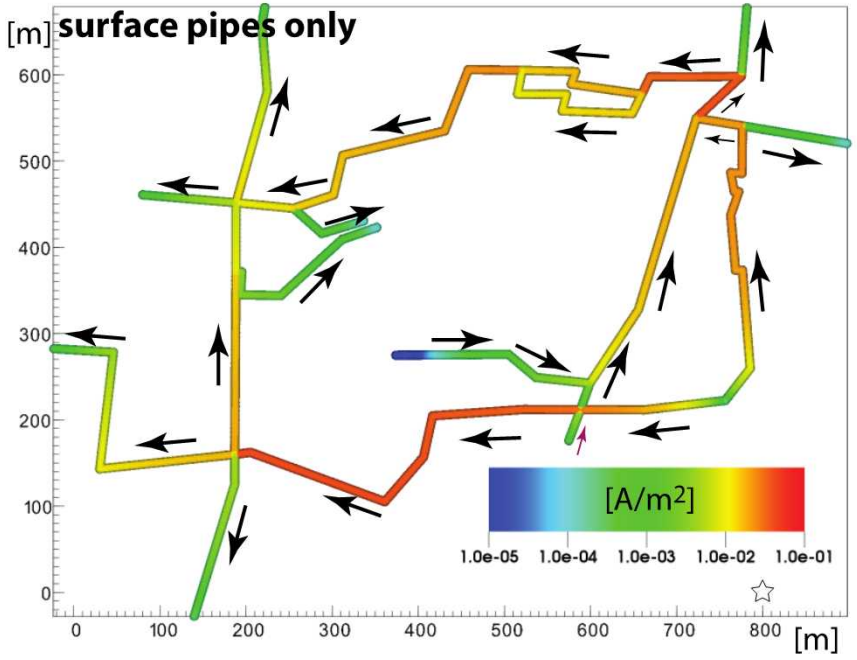

Kern River Formation Site

Surface electric field for fully coupled model. Amplitude only (left), amplitude + direction (right)

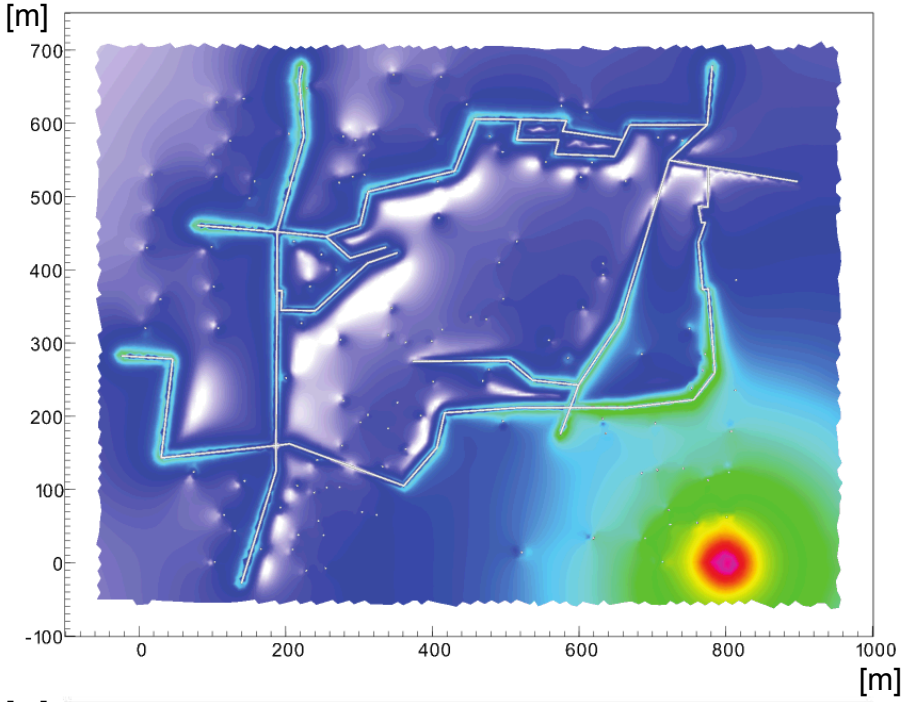

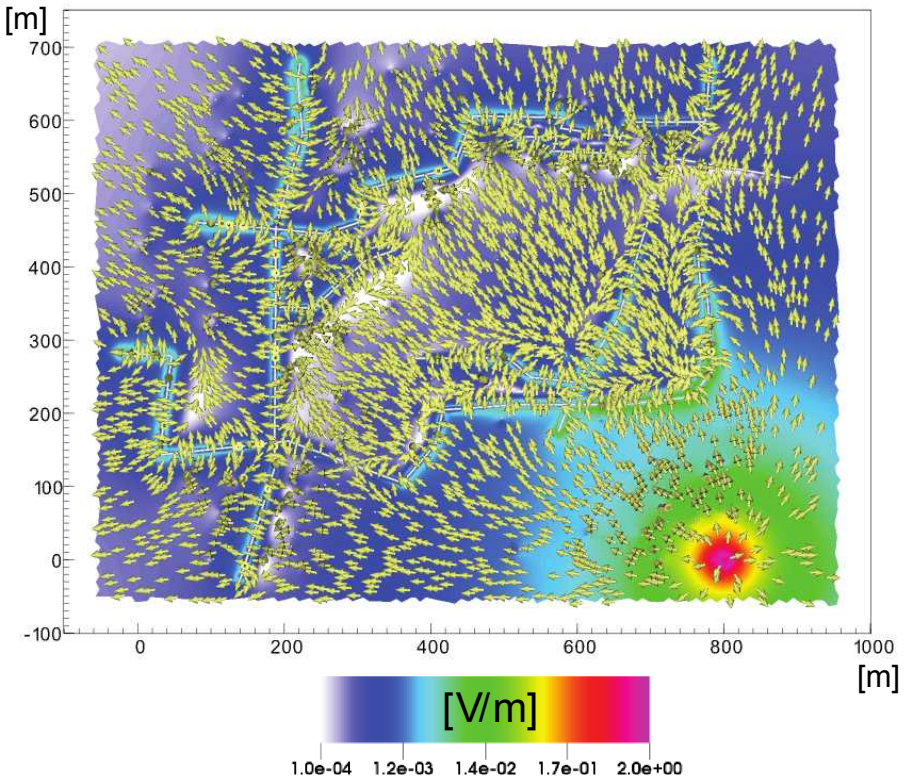

Kern River Formation Site

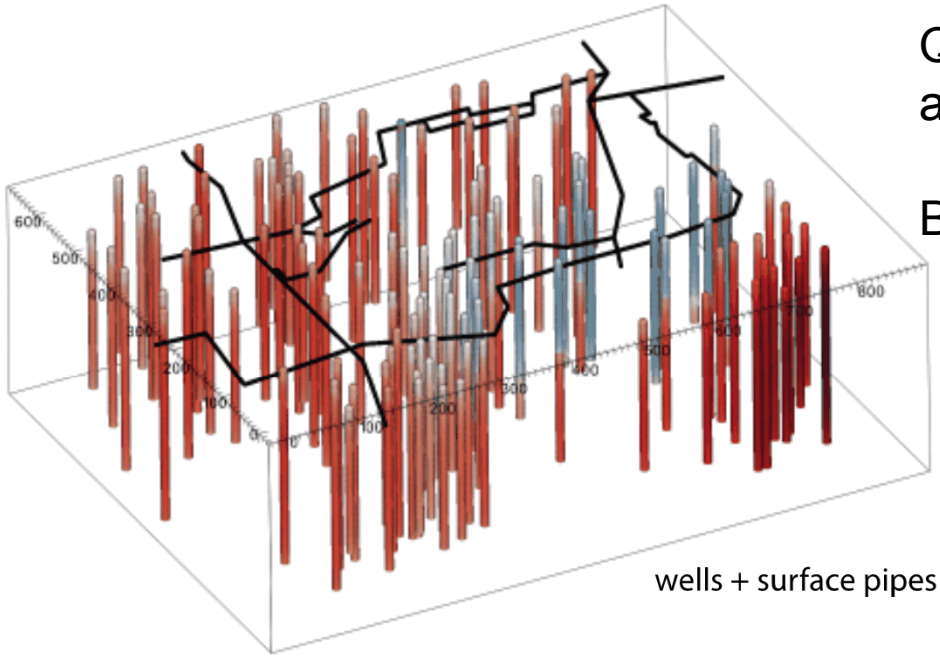

wells + surface pipes

QUESTION: How does pipeline coupling affect casing current direction?

Blue, upward current; red, downward.

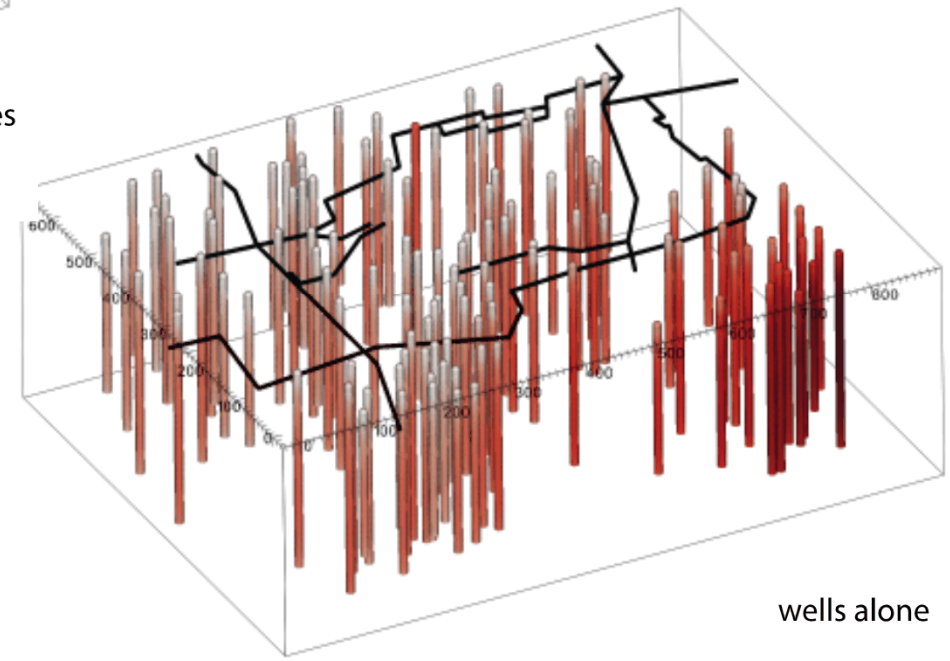

wells alone

To sum up…

1. SNL is investing in novel approaches to electromagnetic modelling of realistic geologic materials, the theoretical underpinnings of which have impacts well beyond geosciences.

2. These modelling approaches are motivated by a growing body of observational evidence for the extistence of a spatially multi-scale Earth.

3. SNL has been applying its computational expertise in electromagnetism to oilfield problems for decades, most recently in the area of fracture detection.

4. Recent SNL advances in finite element analysis, intially targeted at representing thin geology, have immediate application in infrastructure modelling and geologic modelling in cluttered settings. These advances provide access to computational analysis unobtainable elsewhere in the world.